ABSTRACT

EL SAGHIR, AHMED. Improvements to EEDF Analysis from Langmuir Probes Using Integral Methods. (Under the direction of Associate Professor Steven Shannon).

Low density, low temperature plasmas are a vital area of interest in a broad range of applications ranging from nano-scale device fabrication to high efficiency lighting. Langmuir probes are considered a simple and cost efficient technique to diagnose plasmas, specifically, low temperature plasmas. By measuring the voltage/current relationship of the combined probe/plasma circuit, various plasma parameters can be determined. The most important plasma parameter measured by a Langmuir probe can be the Electron Energy Distribution Function (EEDF). Through the EEDF one can determine some characteristics of the plasma such as temperature and density.

In the 1940s Druyvesteyn published results stating that the EEDF can be obtained through the second derivative of the probe *I–V* characteristic through the electron transition portion of the probe trace. This method has been the most widely used for obtaining EEDFs. Since that time other techniques appeared later on in the 1970s taking advantage of Druyvesteyn's relation between the *I–V* characteristic and the EEDF is a Fredholm integral of the first kind, thus leading to the possibility of solving for the EEDF by Tikhonov regularization methods. These regularization techniques were rarely because there were challenges regarding the reconstruction of the EEDF.

In this work we are taking a closer look at both Druyvesteyn's relation and the Tikhonov method. For Tikhonov's method, we were able to overcome its challenges of over and under regularization, as well as the shift that occurs at the beginning of the distribution.

This was carried out by the implementation of our proposed Hybrid method which acted directly on the singular eigenvalues of the kernel matrix, thus removing components that are highly corrupted by noise. The Druyvesteyn relation for EEDF's from Langmuir probes is derived based on a model that assumes spherical probe geometry. Most applications extend this formulation to arbitrary geometries including the more commonly used planar and cylindrical probes. In this work, we present a formulation of the relationship between electron current, probe potential, and EEDF for a cylindrical geometry that also accounts for conservation of angular momentum of the system and provides an identical integral relationship to that posed by Mott-Smith and Langmuir in 1926. This formulation shows a systematic defect in using the Druyvesteyn relation for cylindrical probes that becomes more pronounced for highly non-Maxwellian distributions. In order to minimize this geometry-induced distortion, solution of the integral relation between EEDF and probe current may be needed in place of the more commonly used derivative formulation of Druyvesteyn. Errors of the order 5-15% are common.

Improvements to EEDF Analysis from Langmuir Probes Using Integral Methods

by
Ahmed El Saghir

A dissertation submitted to the Graduate Faculty of
North Carolina State University
in partial fulfillment of the
requirements for the degree of
Doctor of Philosophy

Nuclear Engineering

Raleigh, North Carolina

2011

APPROVED BY:

_____	_____
Dr. David Lalush	Dr. John Gilligan
_____	_____
Dr. Mohamed Bourham	Dr. Steven Shannon Chair of Advisory Committee

DEDICATION

TO MY FAMILY

BIOGRAPHY

Ahmed El Saghir was born in Cairo, Egypt on August 16th, 1982. He received both his Bachelor and Master of Science from Alexandria University from the Nuclear Engineering Department in 2004, and 2007 respectively. He joined the Nuclear Engineering Department at North Carolina State University in August 2007.

ACKNOWLEDGMENTS

In the beginning I would like to thank God for everything in my life. I would like to express my sincere gratitude to my parents for their support, love, and for believing in me. Thank you for being there when I needed you the most. As for my brothers the only thing that I can say is that I am blessed for having them. As for the committee members, I would like to start by thanking Dr. John Gilligan for all the help in getting me to the point of defending my thesis and making it a more complete work. I would like to thank Dr. David Lalush for his questions. The reason for that is I presented my work in numerous conferences and never once did any in the plasma community ask me an intelligent question regarding my work. But it was Dr. Lalush who is from the Biomedical Engineering Department that challenged my thinking by asking those simple but yet intriguing questions. I would like to thank Dr. Mohamed Bourham for his invaluable advice whether it was in plasma or just in general life. It truly helped to correct some of my perspectives and to lead a better life. At last but not least I would like to thank Dr. Steven Shannon not for inviting me into his home and making me feel welcome, nor for being my advisor and sending me out to a bunch of conferences to showcase my work. Although what I just mentioned deserves my true and sincere appreciation and gratitude but there is another reason why I am deeply in debt for Dr. Shannon. I am not an easy character to get along with and truth be said Dr. Shannon had to put up with me, for that I would like to express my sincere gratitude and thanks for Dr. Shannon for putting up with my temper, my flawed character and in sometimes my bad judgment. *THANK YOU DR. SHANNON*.

Finally, I would like to acknowledge Hermine Kabbendjan for always saving the day. I would like to thank Erica Cutchins for her help. I would also like to thank Dr. Karen Nordheden and Lisa Marshall. I would like to acknowledge the financial support provided for this project by the State of North Carolina, the University of North Carolina General Assembly, and the Department of Energy Office of Fusion Energy Science under contract DE-SC0001939, the last of which provided not only financial support but access to the plasma science laboratory managed by Edward Barnat at Sandia National Laboratory, where the experimental results detailed in chapter 5 of this work was obtained. In the end I would like to thank again the committee members for making this come true.

TABLE OF CONTENTS

LIST OF TABLES

LIST OF FIGURES

CHAPTER 1

Introduction

1.1. Historical Background

In order to understand the improvements made in this thesis to the Langmuir probe which is used as a diagnostic technique for plasmas, we need to shed some light on the definition of plasma as well as a Langmuir probe. Apart from the solid, liquid, and gas states plasma can be considered the fourth state of matter. Plasma is a result of matter being heated beyond its gaseous state causing the atoms to be ionized. To have a more formal definition, Plasma is a quasi-neutral gas made up of charged and neutral particles which act in a collective behavior.[1]

Let us define the concept of collective behavior of the plasma. Under normal conditions the molecules of any gas are neutral so they won't be affected by any electromagnetic or gravity force. The motion of the molecules will be controlled by the collisions among themselves. Such motion is known as the random Brownian motion. This isn't the case for plasma since there are charged particles. These charged particles move around producing concentrations of positive and negative charges which give rise to electric fields. These electric fields affect the motion of charged particles which are far away from these fields. Therefore elements of the plasma affect each other even at large separation distances, thus giving the plasma its collective behavior.

As for the plasma being a quasi-neutral gas, this arises from the fact that the plasma consists of small elements or volumes of charged particles either positive (ions) or negative (electrons). Outside these elements and looking at the plasma as a whole the density of ions is approximately equal to the density of electrons causing the plasma to be electrically neutral and thus considered a quasi-neutral gas.

One of the earliest and fundamental techniques for measuring the properties of plasmas is the use of electrostatic probes. This technique was developed by Langmuir as early as 1924 and consequently is sometimes called the method of Langmuir probes. Langmuir confined himself to the case of low pressure, where collisions between charged particles with background neutral gases are neglected. In this case he was able to develop a relatively simple and self consistent theory.[2] An electrostatic probe is a small metallic electrode, usually a wire, inserted into a plasma. The probe is attached to a power supply capable of biasing it at various voltages positive and negative relative to the plasma, and the current collected by the probe then provides information from which plasma parameters such as density and temperature can be inferred.

However, compared to many other diagnostic tools the probe is distinguished by the possibility of direct local measurement of plasma parameters. Since due to the fortunate property of plasmas that under a wide range of conditions the disturbance caused by the presence of the probe is localized. The probe can act truly as a probe in the sense that its very presence has no effect on the quantities it is measuring, making it one of the most valuable tools in experimental plasma science.

The number of possibilities for a meaningful use of probes is subject to many restrictions. There is scarcely another procedure of plasma diagnostics involving so many dangers of incorrect measurement and erroneous interpretation of its results than the probe method as well as the possibility that under certain circumstances, particularly in the presence of a strong magnetic field, the disturbance isn't localized, and the probe current then depends not only on the plasma parameters, but also on the way in which the plasma is created and maintained.

Almost all other techniques, such as spectroscopy or microwave propagation, give information averaged over a large volume of plasma. This advantage of probes, however, is closely connected to their main shortcomings. The local measurement requires the probe to be inserted into the plasma being investigated by means of a probe holder whose surface area in most cases is many times larger than the probe itself. The theory of probes is extremely complicated. The difficulty arises from the fact that probes are considered to be boundaries to a plasma, and near the boundary the equations governing the motion of the plasma alter their character. In particular, the condition of quasi-neutrality, which exists in the body of the plasma is not valid near a boundary; and a layer, called a "sheath" can form in which ion and electron densities can differ and hence large electric fields can be sustained.[2-4]

1.2. Probe-Current Voltage Characteristics

In an isotropic, homogenous plasma, elementary gas-kinetic theory shows that the number of particles of a given species crossing unit area per unit time (from one side only) is

$$\Gamma = \frac{1}{4} n \bar{v} \tag{1.1}$$

where $\bar{v}$ is the mean particle speed, n is particle density and Γ is the particle flux density. Suppose that a probe is present in a thermal plasma of comparable electron and ion temperatures and densities. The mean ion speed will then be much smaller than the mean electron speed so that the total electric current from a probe of area A if the plasma were unperturbed would be dominated by the electrons:

$$I = -eA(\frac{1}{4} n_i \bar{v}_i - \frac{1}{4} n_e \bar{v}_e) \approx \frac{1}{4} eA n_e \bar{v}_e > 0 \tag{1.2}$$

where I is the total electric current. The probe would thus emit a net positive current. If, for example, the probe were electrically insulated from other parts of the plasma device (a "floating" probe), then it would rapidly charge up negatively until the electrons were repelled and the net electrical current brought to zero. The potential arising from such a floating probe is called the floating potential, which is denoted V_f. Clearly it is different from the electric potential in the plasma in the absence of any probe. This latter potential is called the plasma potential and will be denoted V_p. As a simple explanation on the relation between the floating potential and the plasma potential, it should be noted that for an argon ICP (Inductively Coupled Plasma) the plasma potential is around 8 to 12 eV greater than the floating potential, and both of them are always positive.[5]

Figure 1.1 shows the variation of the total electric current I versus the potential of the probe V in a typical Langmuir probe experiment. If the probe is at plasma potential then the perturbations to the free ion and electron currents eq. 1.2 will be small. Thus, the space potential is approximately the point at which $I \approx$ *Probe area x* eJ_e , the electron current. If the

voltage is increased above this level, $V > V_p$, in principle the electron current can not increase any further. This is because the electron current is maximized since all electrons arriving are collected. Due to conservation of flux, the current of electrons can no longer increase since there are no additional mechanisms to add to the initial flux at the plasma sheath interface. Under these same conditions, the ion current J_i decreases because of repulsion of the ions so I is approximately constant. This region (A) is known as electron saturation and I here is equal to the electron-saturation current.[5]

Decreasing the probe potential, $V < V_p$, the probe is now negative with respect to the surrounding plasma and an increasing fraction of impinging electrons is reflected from the negative potential (region B). Eventually the potential is sufficient to reduce J_e to a small fraction of its saturation value. At some point, the electron current decreases to the level of the ion current, and the total current is zero when $J_e = J_i$ at the floating potential V_f . Decreasing the potential further, entering region C, eventually only ions are collected at approximately the constant rate given by eq. 1.1 since almost all of the electrons do not have the energy needed to overcome the probe's space charge potential.

This is the ion saturation current $I = I_{si}$.[5] Although the thesis is mainly dealing with the distribution of electrons collected by the probe but the theory behind the ion collection and subtraction from the I-V curve will be discussed thoroughly in the following chapter.

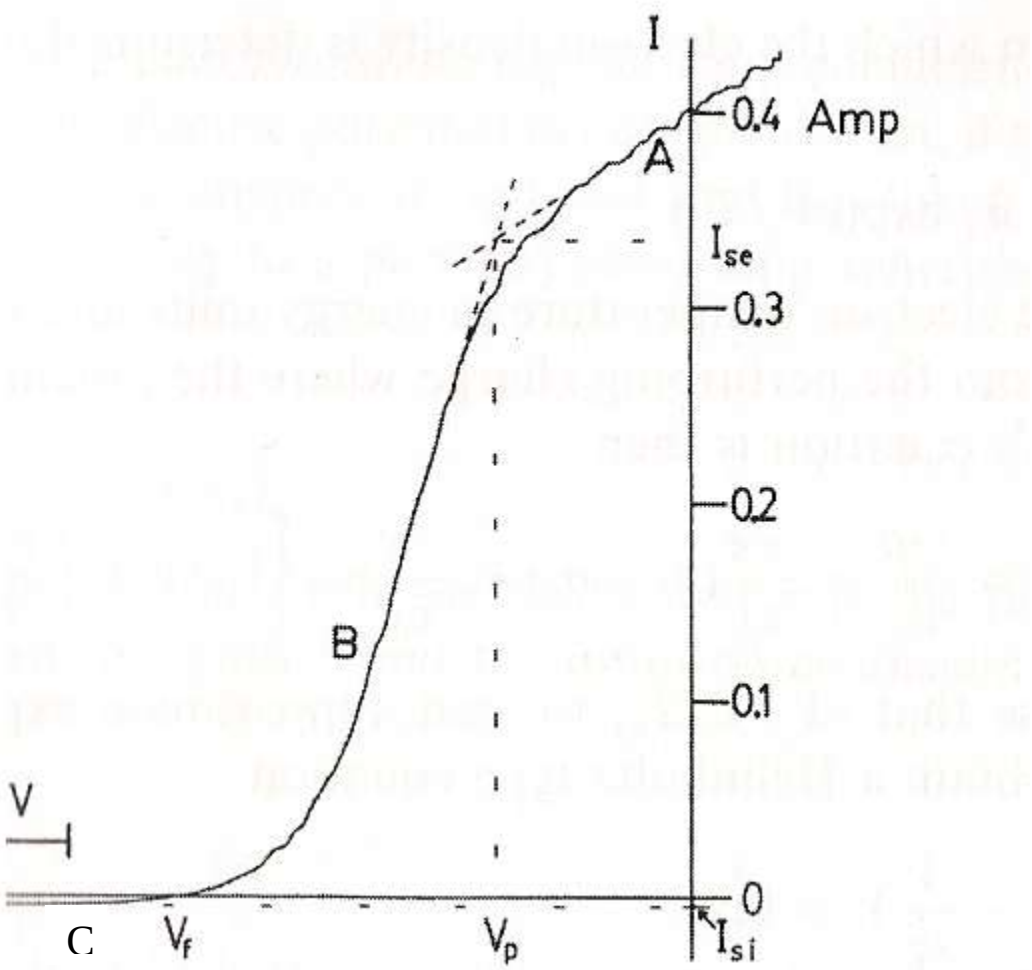

Figure 1.1. Electric probe characteristic showing how the probe current varies with probe potential.[5]

1.3. Research Motivation

One application of probe methods is in the area of low temperature low-density plasma discharges where strongly nonequilibrium plasmas are typically encountered.[6,7] These discharges are utilized for their novel chemistries for various industrial applications

from integrated-circuit fabrication to glass coatings. This has placed a significant value on the measurement of parameters such as EEDFs (Electron Energy Distribution Functions) that can impact plasma chemistry and provide experimental validation for modeling efforts that are working to better understand these discharges for enhanced capability and control. The importance of the field of low-temperature plasmas, as well as the specific need for chemistry study and enhanced diagnostics for modeling validation, was cited by the National Research Council in its decadal report on plasma science and in a recent report released by the Department of Energy's Office of Fusion Energy Sciences.[8,9]

One key point that is mentioned in the decadal report, which is of relevance to our present work, is the unifying scientific principles behind the societal benefit of low-temperature plasmas as a result of the study of plasma heating, stability, and control. The bulk heating of low-temperature plasmas (sans the sheath region) goes predominantly to the heating of free electrons. However, for most systems, this does not result in a thermal equilibrium, and unique non-Maxwellian distributions can arise in these systems [10-12]. The analysis of these EEDFs has proven to be a powerful tool for the discovery of new heating mechanisms.

Several recently introduced models suggest an even stronger correlation between EEDF and various heating mechanisms than previously reported [13]. The improvements in the measurement of the energy distribution of these electrons will provide greater insight into different heating methods (VHF, multifrequency RF, pulsed RF, superimposed dc, etc.) and provide valuable inputs for predictive modeling, new source development, and modeling validation. The only method to obtain EEDFs is through the application of Langmuir probes.

As discussed earlier by varying the bias on the probe the amount of electrons and ions collected vary giving us the I-V characteristic curve. By subtracting the ion current from the I-V curve we are left with the electron current. Now that the electron current is known the energy of the electrons reaching the probe can be determined. It should be noted that electrons with very little energy are repelled with the slightest drop below the plasma potential, while highly energetic electrons are repelled with only the largest drop from plasma potential. So the probe can be considered acting as a simple electron repelling grid. As a result the electron energy distribution is proportional to the second derivative of the electron current to the probe as shown in eq. 1.3.

$$f(E)_{E=-eV_{probe}} = -\frac{4}{A_p e^2}\sqrt{-\frac{m_e V_{probe}}{2e}}\frac{d^2 I_e}{dV_{probe}^2} \tag{1.3}$$

where I_e is the electron contribution to the current collected by the Langmuir probe, A_p is the area of the probe, e is electron charge, m_e is electron mass, V_{probe} is the potential of the probe (referenced to the plasma potential), and $f(E)$ is the EEDF, or the number of electrons per cm^3 with total energy between E and $E+dE$. The aforementioned equation is known as the Druyvesteyn's relation

In practice, one usually neglects non-Maxwellian effects in inferring plasma parameters from the probe characteristics, assuming that the actual deviation of an EEDF from Maxwellian has minor affects on a small number of electrons with energies that are higher than the energy of the inelastic threshold E* . Unfortunately, in many cases, the EEDF

in low-pressure discharges is not Maxwellian, even in the low-energy range where $E < E^*$ and application of conventional procedures such as the Druyvesteyn relation, or basic Tikhonov Regularization for processing probe characteristics in non-Maxwellian plasmas may lead to significant errors in the determination of basic plasma parameters.

This thesis is focused on enhancing the extraction of EEDFs from Langmuir probe data by employing methods that properly address the ill-posed nature of EEDF extraction, as well as taking the geometry of the probe into consideration which is largely neglected by the conventional methods by assuming that cylindrical and spherical probes collect the same number of electrons which will be proved later in the thesis to be absolutely wrong.

1.4. Thesis Outline

This research has both theoretical and experimental aspects. The theoretical aspect will be covered in chapters 2 through 4. Chapter 2 will cover in detail the response of electrons to the insertion of a biased probe in the plasma, taking into consideration the kinetics of the electrons, as well as the geometry of the probe since the probe can be planar, cylindrical, and spherical. It also covers the integral relation governing the extraction of the Electron Energy Distribution Function (EEDF) from the probe current. This relation will be shown to be of an ill-posed nature causing difficulties regarding the extraction process. Other topics will be covered such as secondary electrons which are emitted through the collision of high energetic electrons with the probe and then reabsorbed, and the effect of the length of the probe regarding both species (ions and electrons). Chapter 3 will cover the procedure that was carried out to obtain an EEDF from the probe current, the initial results obtained by the

application of Tikhonov's regularization to the ill-posed problem, the challenges arising from Tikhonov's technique and the numerical techniques devised to overcome such challenges. At the end of the chapter it will be shown that such techniques are limited when dealing with velocity distributions. Chapter 4 will cover the systematic error arising from the geometry of the probe which was mentioned in Langmuir's paper and neglected by Druyvesteyn's relation. Chapter 5 will deal with the numerical results and the comparison to the experimental results. Finally, chapter 6 will be the conclusion of the research and a talk about the future work.

1.5. References

[1] Chen F. F., "Introduction to Plasma Physics and Controlled Fusion", Springer, 1984, ch1.

[2] Mott-Smith and Langmuir; "The Theory of Collectors in Gaseous Discharges." *Phys. Rev.* 28, 1926, pp. 727-763.

[3] "Plasma Diagnostic Techniques", Edited by Richard Huddlestone, and Stanley Leonard, Academic Press, 1965, ch. 4.

[4] Lochte-Holtgreven W. "Plasma Diagnostic Techniques", American Institute of Physics Press, 1995, ch. 11.

[5] Hutchinson I. H. “Principles of Plasma Diagnostics”, Cambridge University Press, 2002 ch. 3.

[6] Tichy M., Hubicka Z., Sicha M., Hori T., Kogano M., Bowden M. D., Uchino K., and Muraoka K. “ A study of Electron Energy Distribution in an Inductively Coupled Plasma by laser Thompson Scattering.” *J. Applied Phys.* 83 (4) ,1998, pp.1909-1916.

[7] National Research Council (U.S.) Plasma 2010 Committee, Plasma Science: Advancing Knowledge in the National Interest, Plasma Science Committee, Board on Physics and Astronomy, Division on Engineering and Physical Sciences: Nat. Acad. Press, 2007.

[8] V. A. Godyak, R. B. Piejak, and B. M. Alexandrovich “Probe diagnostics of Non-Maxwellian Plasmas.” *J. Applied Phys.* 73 (8), 1993, pp.3657-3663.

[9] A. Schwabedissen, E. C. Benck, and J. R. Roberts “Langmuir probe measurements in an inductively coupled plasma source.” *Phys. Rev. E, Stat. Phys. Plasmas Fluids Relat. Interdiscip. Top.* 55(3), 1997, pp. 3450– 3459.

[10] B. Crowley and S. Dietrich “A Langmuir probe system incorporating the Boyd–Twiddy method for EEDF measurement applied to an inductively coupled plasma Source.” *Plasma Sources Sci. Technol.* 18(1), 2009, pp. 014 010–014 017.

[11] “Low temperature plasma science: Not only the fourth state of matter but all of them.” Report of the Dept. of Energy Office of Fusion Energy Sciences Workshop on Low Temperature Plasmas 2008, Mar. 25–27.

CHAPTER 2

Current Collection by a Langmuir Probe

2.1. Introduction

A plasma probe which is charged to a potential differing from that of a surrounding plasma, will lead to the creation of an electric field that attracts particles of opposite charge and repels those of like charge. If the probe potential is large enough, very few of the repelled particles will have sufficient kinetic energy to reach the probe surface, and the region adjacent to the probe will contain only attracted particles. The net space charge density in the region surrounding the probe will be of opposite sign to the charge on the probe, and will tend to prevent electric fields from penetrating into the plasma as shown in figure 2.1. This region of charge imbalance is known as a sheath. Beyond the sheath, the densities of both repelled and attracted charged particles are very nearly equal, and the electric field is relatively weak, though still significant.

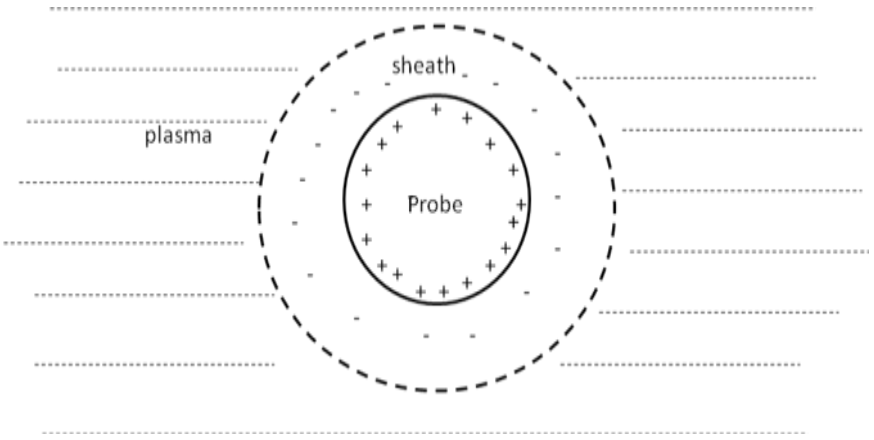

Figure 2.1. Since the probe is positively biased the sheath formed around it is negatively charged.

Any charge imbalance in an ionized plasma sets up electric fields that tend to limit its extent and neutralize it. It has been shown that the sheath thickness is always related to a plasma parameter known as the Debye shielding distance λ_D,

$$\lambda_D = \left(\frac{\varepsilon_o KT_e}{ne^2}\right)^{\frac{1}{2}} \tag{2.1}$$

where KT_e is the electron temperature in eV, n is the number density of electrons, ε_o is the permittivity of free space, and e is the electron charge. The ratio of probe radius to Debye distance is one of the factors that govern whether the sheath that surrounds the probe is thin or thick. As an example take the case where the probe radius is smaller than Debye length, in this case the sheath is called a thick sheath and will lead to the fact that a cylindrical probe tip will have characteristics closer to a spherical probe. Since the flux of attracted particles reaching the probe can be strongly affected by the shape and extent of this potential, the ratio of probe radius to Debye length has a strong influence on the collected current. Measurements of collected current will therefore contain information about the Debye lengths of the various species as shown in figure 2.2.

A charged particle that comes within the influence of the probe is affected in general not only by the macroscopic electric field surrounding the probe, but also by the scattering effect of encounters with other particles, particularly neutral gas species that have a volume density on the order of 100 to 1000 times that of the charged species in a low temperature plasma. The surface of a plasma probe is always at a much lower temperature than the plasma. As a result, nearly all electrons that strike it are absorbed, and nearly all ions that

strike it combine with electrons from the surface and move off as neutral atoms.

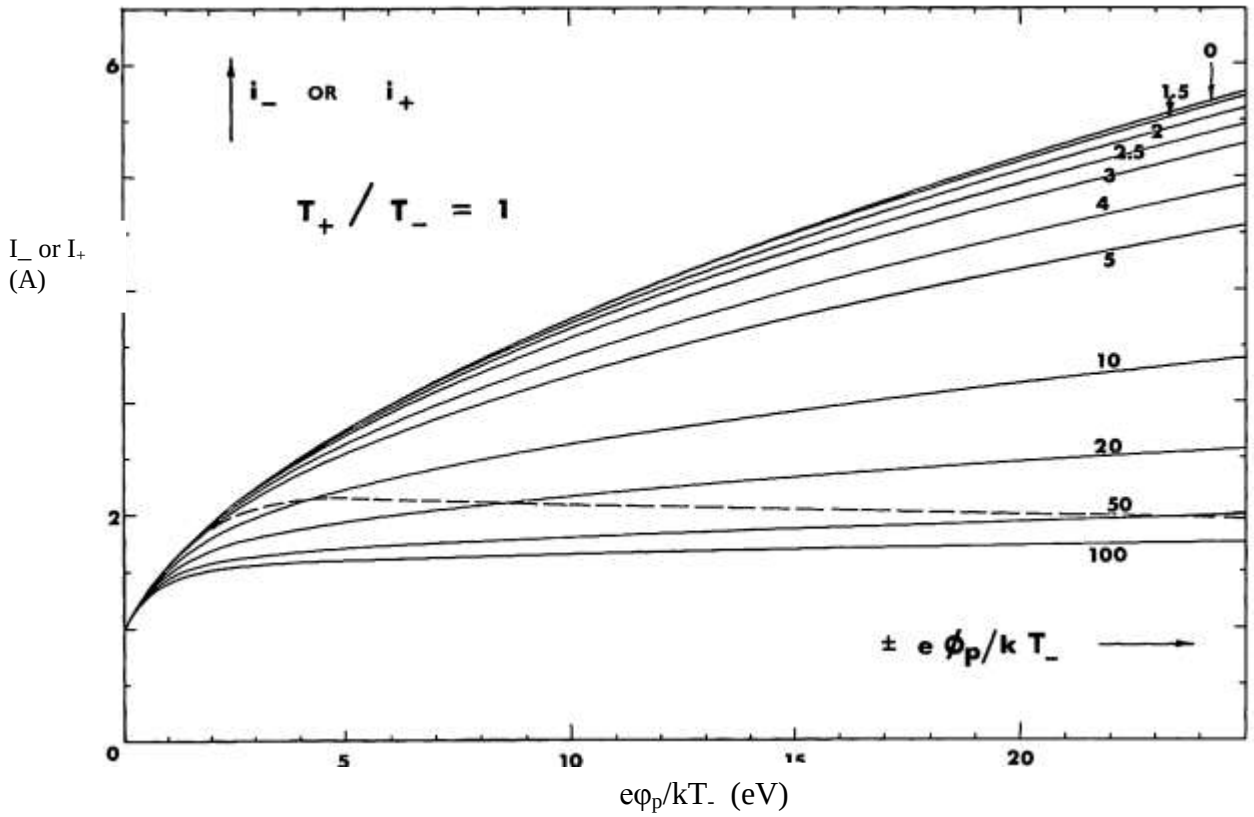

Figure 2.2. Ion or electron current vs probe potential for various ratios of probe radius to ion or electron debye length; cylindrical probe; dotted curve shows trapped orbit boundary.[1]

These neutrals do not interact with electric fields and, in the collision less approximation, are in effect removed from the problem. It should be noted that secondary electrons (electrons emitted by the probe due to bombardment of ions on it) do contribute in some cases by being recollected and this will be discussed later in this chapter.

The plasma probes come in a variety of shapes. Some are planar, cylindrical or spherical, with the cylindrical being the most common due to its simplicity in construction. Since the usefulness of such a probe to the experimenter is considerably enhanced with the availability of good theoretical models that depict its characteristics. The most useful shapes are usually those possessing sufficiently high symmetry such as the spherical or cylindrical probe, that the dynamics of particle motion in the electric fields near the probe are of simplified form. In particular, the cases considered here are those of a sphere or long cylinder in stationary plasma. In these cases, all particles move in central force fields[2].

2.2. Electron Acceleration: The Orbital Motion Limited Theory

2.2.1. Cylindrical Probe Generalized Velocity Distribution

Mathematically, we start by applying the conservation laws of energy and momentum to the electrons crossing the sheath region. The derivation below was carried out by Swift and Schwar. Thus, in general, we have

$$E = \frac{1}{2} m_e (u^2 + v^2 + w^2) - eV(r) \tag{2.2}$$

$$J = m_e v r \tag{2.3}$$

where *u,v,w* are the velocity components in arbitrary three dimensional space, *E* is the total energy, *e* is the charge, m_e is the electron mass, *J* is the momentum and *V(r)* is the potential relative to the sheath edge. We assume for this study that the potential is purely radial, and ignore axial fields generated by the finite length or asymmetries of the probe construction. It is noted, however, that these effects can have a significant impact on near probe charged

particle dynamics, particularly when the debye length approaches the characteristic scale length of the probe.[3] Instead of carrying out the analysis in terms of total energy, momentum, and effective potential energy, it is simpler to consider u , the radial velocity component, and v the tangential velocity component. Before proceeding with the analysis it is convenient at this stage to mention the assumptions made by Langmuir in developing his theory and summarized by Swift and Schwar [2,4]. They are:

1. Carrier densities are known at the sheath edge.
2. Carrier velocity distributions are known at the sheath edge.
3. The entire probe potential is developed across the sheath.
4. Gas pressures are sufficiently low for no collisions to occur in the sheath region.
5. The probe is sufficiently small for it not to disturb the plasma.
6. Carriers are neutralized on reaching the probe surface.
7. Carriers are not emitted or reflected from the probe surface.
8. The effect of space charge sheaths surrounding the supports and lead wires to the probe are ignored.

If $f(u_s,v_s,w_s)du_s\, dv_s\, dw_s$ is the number of electrons per unit volume at the sheath edge having velocity components in the range u_s to u_s+du_s, v_s to v_s+dv_s, and w_s to $w_s + dw_s$ and if r_s is the sheath radius the flux of electrons in this velocity range crossing the sheath edge is

$$dJ = 2\pi r_s L f(u_s, v_s, w_s) u_s du_s dv_s dw_s \qquad (2.4)$$

It is assumed that the length L of the cylindrical probe is sufficiently large compared with r_s for the velocity component parallel to the axis of the cylinder to make no contribution to the

electron flux crossing the sheath edge. In order to calculate the flux of the electrons that reach the probe it is necessary to examine their orbital motion within the sheath region.

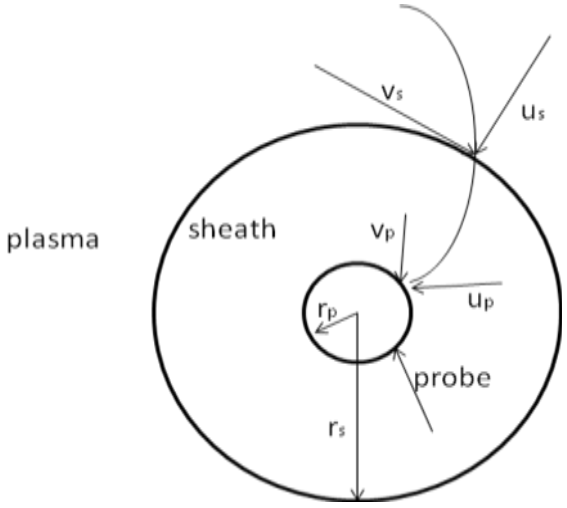

Figure 2.3. Velocity components of an electron crossing the space charge sheath surrounding a cylindrical probe

Let u_s,v_s,and w_s be the velocity components at the sheath edge and u_p,v_p, and w_p be the corresponding components at the probe's surface. From eqs 2.2 and 2.3 we have

$$\frac{1}{2}m_e(u_s^2+v_s^2+w_s^2)=\frac{1}{2}m_e(u_p^2+v_p^2+w_p^2)-eV_p \tag{2.5}$$

$$m_e v_s r_s = m_e v_p r_p \tag{2.6}$$

Eqs 2.5 and 2.6 may be solved simultaneously for the tangential and the radial velocity components at the probe surface, to give

$$v_p = v_s(\frac{r_s}{r_p}) \tag{2.7}$$

$$u_p^2 = u_s^2 - v_s^2[(\frac{r_s}{r_p})^2-1]+\frac{2eV_p}{m_e} \tag{2.8}$$

An electron contributes to the electron current if its radial velocity component at the probe surface is greater than zero. In order that an electron, having a radial velocity at the sheath edge of u_s, should reach the probe it must also have a tangential velocity in the range

$$0 \le v_s^2 \le [\frac{r_p^2}{r_s^2 - r_p^2}][u_s^2 + \frac{2eV_p}{m_e}] \tag{2.9}$$

The smallest value of u_s that an electron can have and still be able to reach the probe surface is zero for positive values of V_p. For negative values of V_p it can be seen from eq 2.9, by putting v_s equal to zero, to be $(-2eV_p/m_e)^{1/2}$. The upper limit of u_s is $+\infty$ and the limits of w_s are $\pm\infty$. Integrating eq 2.4 between these limits gives the flux of electrons reaching an electron accelerating probe as

$$J_e = 2\pi r_s L \int_0^{\infty} \int_{-\infty}^{\infty} \int_{-v_1}^{v_1} u_s f(u_s, v_s, w_s) du_s dv_s dw_s \tag{2.10}$$

where

$$v_1 = [\frac{r_p^2}{r_s^2 - r_p^2}]^{1/2} [u_s^2 + \frac{2eV_p}{m_e}]^{1/2} \tag{2.11}$$

2.2.2. Cylindrical Probe Maxwellian Velocity Distribution

Assuming that the electrons at the sheath edge possess a Maxwellian velocity distribution $f(u_s,v_s,w_s)du_s\, dv_s\, dw_s$ maybe replaced by

$$N_\infty (\frac{m_e}{2\pi kT_e})^{3/2} \exp\{-\frac{m_e}{2kT_e}(u_s^2 + v_s^2 + w_s^2)\} du_s dv_s dw_s \tag{2.12}$$

Inserting this into eq 2.10 and integrating gives

$$J_e = 2\pi r_p L N_\infty \left(\frac{kT_e}{2\pi m_e}\right)^{1/2} \left\{\frac{r_s}{r_p}\left[1 - erfc\left(\frac{r_p^2 eV_p / kT_e}{r_s^2 - r_p^2}\right)^{1/2}\right] + \exp\left(\frac{eV_p}{kT_e}\right) erfc\left(\frac{r_s eV_p / kT_e}{r_s^2 - r_p^2}\right)^{1/2}\right\} \quad (2.13)$$

2.2.3. Spherical Probe Maxwellian Velocity Distribution

The corresponding equation for a spherical probe is

$$J_e = 4\pi r_s^2 N_\infty \left(\frac{kT_e}{2\pi m_e}\right)^{1/2} \left\{1 - \left[1 - \frac{r_p^2}{r_s^2}\right] \exp\left(-\frac{r_p^2 eV_p / kT_e}{r_s^2 - r_p^2}\right)\right\} \quad (2.14)$$

2.2.4. Limiting Cases

Eqs 2.13 and 2.14 show that the electron fluxes to cylindrical and spherical probes in the case of a Maxwellian distribution are complicated functions of probe potential and sheath and probe radii. In order to use these expressions to determine, say, electron concentrations assuming T_e to be known, it is also necessary to know the value of r_s and also how it depends on V_p.

The determination of r_s, i.e. the radius that represents the region within which only electrons are present, is extremely difficult. This is partly due to the fact that a gradual transition takes place between the sheath and the neutral plasma and the separation point between these two regions must be arbitrary. Therefore an adequate position is to operate the probe under the condition where the electron flux is independent of r_s or where r_s can be determined theoretically. These two conditions will be shown to be satisfied when the ratio r_s / r_p either tends to infinity or is very close to unity.[2,5,6]

2.2.4.1. Cylindrical Case

Rewriting eq 2.13 when r_s/r_p tends to infinity and η is substituted for eV_p/kT_e gives

$$J_e = 2\pi r_p L N_\infty \left(\frac{kT_e}{2\pi m_e}\right)^{1/2} \left\{\frac{r_s}{r_p}\left[1 - erfc\left(\frac{r_p}{r_s}\eta^{1/2}\right)\right] + \exp(\eta)erfc(\eta^{1/2})\right\} \quad (2.15)$$

$$J_e = 2\pi r_p L N_\infty \left(\frac{kT_e}{2\pi m_e}\right)^{1/2} \left\{\frac{r_s}{r_p}\frac{2}{\sqrt{\pi}}\int_0^{\frac{r_p}{r_s}\eta^{1/2}} e^{-y^2}dy + \exp(\eta)erfc(\eta^{1/2})\right\} \quad (2.16)$$

In the limit as $(r_p/r_s)\eta^{1/2}$ tends to zero, eq 2.16 reduces to

$$J_e = 2\pi r_p L N_\infty \left(\frac{kT_e}{2\pi m_e}\right)^{1/2} \left[\frac{2}{\sqrt{\pi}}\eta^{1/2} + \exp(\eta)erfc(\eta^{1/2})\right] \quad (2.17)$$

Figure 2.4 shows a plot of $\left[\frac{2}{\sqrt{\pi}}\eta^{1/2} + \exp(\eta)erfc(\eta^{1/2})\right]$ against η as well as a plot of $\frac{2}{\sqrt{\pi}}[1+\eta]^{1/2}$ against η. Note that for values of η greater than 2 the two curves asymptotically coincide. Eq 2.17 therefore simplifies to

$$J_e = 2\pi r_p L N_\infty \left(\frac{kT_e}{2\pi m_e}\right)^{1/2} \frac{2}{\sqrt{\pi}}\left(1 + \frac{eV_p}{kT_e}\right)^{1/2} \quad for\ V_p > \frac{2kT_e}{e} \quad (2.18)$$

Although it is shown in both eqs 2.17 and 2.18 that when r_s/r_p tends to infinity, the electron flux is independent of the sheath radius, another problem exists which is the absence of a value or estimate of r_s in order to determine whether or not the condition r_s/r_p tends to infinity is satisfied. Unfortunately there is no way of determining the sheath radius in the case when the electrons move with orbital motion but the condition may reasonably be assumed to be satisfied when λ_D/r_p tends to infinity. In the limit of r_s/r_p tending to unity the two

complementary error functions in eq 2.13 become zero and so the expression for the electron flux to a cylindrical probe is now

$$J_e = 2\pi r_p L N_\infty \left(\frac{kT_e}{2\pi m_e}\right)^{1/2} \tag{2.19}$$

Eq. 2.19 shows that all the electrons that enter the sheath hit the probe. This will lead to the assumption that the electrons pass through the sheath region with their velocity vector normal to the probe's surface.

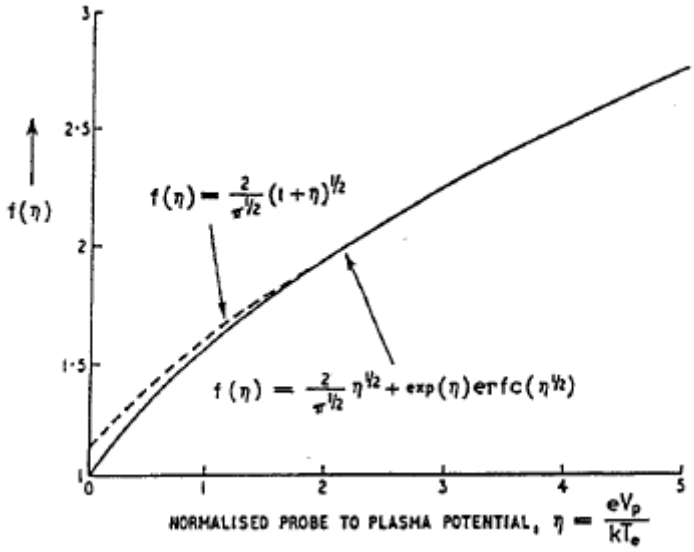

Figure 2.4. A plot of the functions appearing in eqs 2.16 and 2.17 showing how *f(η)* depends on the normalized probe to plasma potential *η*.[11]

2.2.4.2. Spherical Case

Eq. 2.14 can be rewritten in the limit when r_s / r_p tends to infinity as

$$J_e = 4\pi r_s^2 N_\infty \left(\frac{kT_e}{2\pi m_e}\right)^{1/2} \{1 - [1 - \frac{r_p^2}{r_s^2}][1 - \frac{r_p eV_p / kT_e}{r_s^2 - r_p^2}]\} \quad (2.20)$$

$$J_e = 4\pi r_s^2 N_\infty \left(\frac{kT_e}{2\pi m_e}\right)^{1/2} [1 + \frac{eV_p}{kT_e}] \quad (2.21)$$

This equation maybe applied when λ_D / r_p tends to infinity. In the limit of r_s / r_p tending to unity the exponential term in eq. 2.14 becomes unity and the electron flux to a spherical probe reduces to

$$J_e = 4\pi r_s^2 N_\infty \left(\frac{kT_e}{2\pi m_e}\right)^{1/2} \quad (2.22)$$

2.2.5. Limitations of the Orbital Motion Limited Theory

The theory described in the above sections contains an implicit assumption. The assumption is that for an attractive probe any particle that hits or at least grazes the probe is absorbed. This assumption may not be totally accurate, since there exists a radius (greater than the probe radius) surrounding the probe called an absorption radius. It is assumed that any particle that passes through the absorption radius will eventually get absorbed by the probe.

Let us consider the case of ion collection, and focus our attention on ions within a narrow energy range. If all imaginary cylindrical (or spherical) surfaces outside the probe are ‘grazed‘ by ions then the corresponding impact parameters must all be greater than h_p, i.e.

$$r(1-\frac{V}{V_0})^{1/2} > r_p(1-\frac{V_p}{V_0})^{1/2} \tag{2.23}$$

where the initial energy of the electron is eV_0. Rearranging, the condition for no absorption radius to exist can be written

$$\frac{V_0 - V}{V_0 - V_p} > (\frac{r_p}{r})^2 \tag{2.24}$$

If this condition is to hold for all of the ions, including those with small initial energies then

$$\frac{V}{V_p} > (\frac{r_p}{r})^2 \tag{2.25}$$

It appears that in dense plasmas this condition seizes to hold and we need an absorption radius to replace the probe radius. Whether or not the inequality holds in a particular case is difficult to say, leading us to taking a look at Poisson's equation and probably solving it.

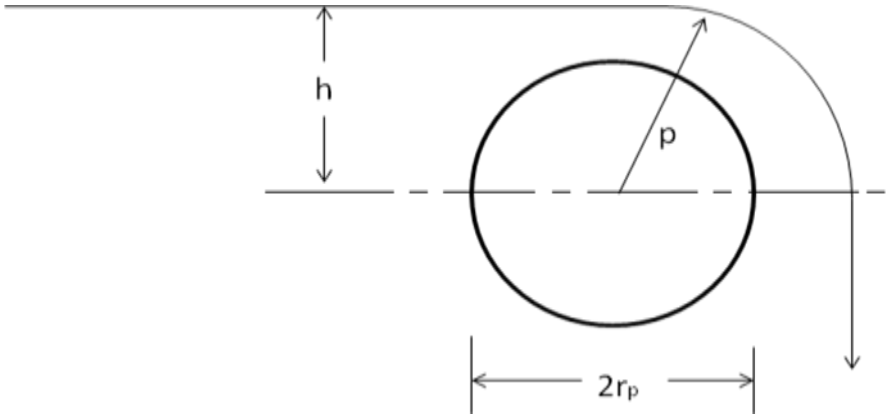

Figure 2.5. Diagram illustrating the impact parameter h and the distance of closest approach p.

2.2.6. ABR Theory

In order to properly account for the sheath theory, one has to solve Poisson's equation for the potential $V(r)$ from the probe surface to $r = \infty$. Allen, Boyd, and Reynolds (ABR) simplified the problem by assuming ab initio that $T_i = 0$, thus neglecting any orbital motion, leading to the fact that the ions are attracted radially into the probe.[6,7] Although the ABR theory was only for spherical probes, Chen extended it to cylindrical probes.[8] The derivation below was carried out by Chen.[6] Assume that the probe is centered at $r = 0$ and that the ions start at rest from $r = \infty$, where $V = 0$. Poisson's equation in cylindrical coordinates is

$$\frac{1}{r}\frac{\partial}{\partial r}\left(r\frac{\partial V}{\partial r}\right) = \frac{e}{\varepsilon_0}(n_e - n_i), \quad n_e = n_0 e^{eV/kT_e} \tag{2.26}$$

where electrons are assumed to be Maxwellian. To find n_i, let I be the total ion flux per unit length collected by the probe. By current continuity, the flux per unit length at any radius r is

$$\Gamma = n_i v_i = I/2\pi r \quad \text{where} \quad v_i = (-2eV/M)^{1/2} \tag{2.27}$$

Thus,

$$n_i = \frac{\Gamma}{v_i} = \frac{I}{2\pi r}\left(\frac{-2eV}{M}\right)^{-1/2} \tag{2.28}$$

Poisson's equation can then be written

$$\frac{1}{r}\frac{\partial}{\partial r}\left(r\frac{\partial V}{\partial r}\right) = -\frac{e}{\varepsilon_0}\left(\frac{I}{2\pi r}\left(\frac{-2eV}{M}\right)^{-1/2} - n_0 e^{eV/kT_e}\right) \tag{2.29}$$

Defining

$$\eta = -eV/kT_e, \quad c_s = \left(\frac{kT_e}{M}\right)^{1/2} \tag{2.30}$$

rewriting write eq. 2.29 as

$$\frac{kT_e}{e}\frac{1}{r}\frac{\partial}{\partial r}(r\frac{\partial \eta}{\partial r}) = -\frac{e}{\varepsilon_0}(\frac{I}{2\pi r}\frac{(2\eta)^{-1/2}}{c_s} - n_0 e^{-\eta}) \tag{2.31}$$

or

$$-\frac{\varepsilon_0 kT_e}{n_0 e^2}\frac{1}{r}\frac{\partial}{\partial r}(r\frac{\partial \eta}{\partial r}) = \frac{I}{2\pi r}\frac{(2\eta)^{-1/2}}{n_0 c_s} - e^{-\eta} \tag{2.32}$$

the debye length appears on the left-hand side as the natural length for this equation. We therefore normalize *r* to λ_D by defining a new variable ξ

$$\xi = \frac{r}{\lambda_D}, \quad \lambda_D = (\frac{\varepsilon_0 kT_e}{n_0 e^2})^{1/2} \tag{2.33}$$

rewriting eq. 2.32

$$\frac{\partial}{\partial \xi}(\xi\frac{\partial \eta}{\partial \xi}) = \frac{eI}{2\pi kT_e}(\frac{M}{2\varepsilon_0 n_0})^{1/2}\eta^{-1/2} - \xi e^{-\eta} \tag{2.34}$$

Defining

$$J = \frac{eI}{2\pi kT_e}(\frac{M}{2\varepsilon_0 n_0})^{1/2} \tag{2.35}$$

we arrive at the ABR equation for cylindrical probes:

$$\frac{\partial}{\partial \xi}(\xi\frac{\partial \eta}{\partial \xi}) = J\eta^{-1/2} - \xi e^{-\eta} \tag{2.36}$$

Of course, both *J* and ξ_p (the probe radius)depend on the unknown density n_o , which is to be determined from the measured current I_i.

2.2.7. BRL Theory

Bernstein and Rabinowitz are considered to be the first who published a probe theory taking into account both sheath formation and orbital motions was published by assuming an isotropic distribution of ions of a single energy E_i.[9] This was further refined by Laframboise, who extended the calculations to a Maxwellian ion distribution at temperature T_i.[1] The BRL treatment is considerably more complicated than the ABR theory. According to ABR, all ions strike the probe, so the flux at any radius depends only on the conditions at infinity, and not on the probe radius. In BRL theory, it is assumed that there are two groups of ions. One group that will hit the probe thus contributing only once to the ion density, while the other group which orbits the probe and thus will contribute twice at any given radius *r*. The ion density must be known before Poisson‘s equation can be solved, and clearly this depends on the presence of the probe. There is an absorption radius as shown in figure 2.6, depending on *J*, inside of which all ions are collected. Bernstein approached the problem in a different technique by expressing the ion distribution in terms of energy *E* and angular momentum *J* instead of v_r and $v_\perp$. Ions with a given *J* see an effective potential barrier between them and the probe. They must have enough energy to overcome this barrier before they can be collected. In figure 2.7, the lowest curve is for ions with $J = 0$; these simply fall into the probe. Ions with finite *J* see a potential hill and with sufficient energy, they can climb the hill and be collected by the probe. The dashed line through the maxima shows the absorption radius for various values of *J*. It turns out that KT_i makes little difference if $T_i/T_e < 0.1$ or so, as it usually is. One sees that for large probes ($R_p/\lambda_D >> 1$) the ion current

saturates well, since the sheath is thin. For small R_p/λ_D, I_i grows with increasing V_p as the sheath radius increases.[1,5,6,7]

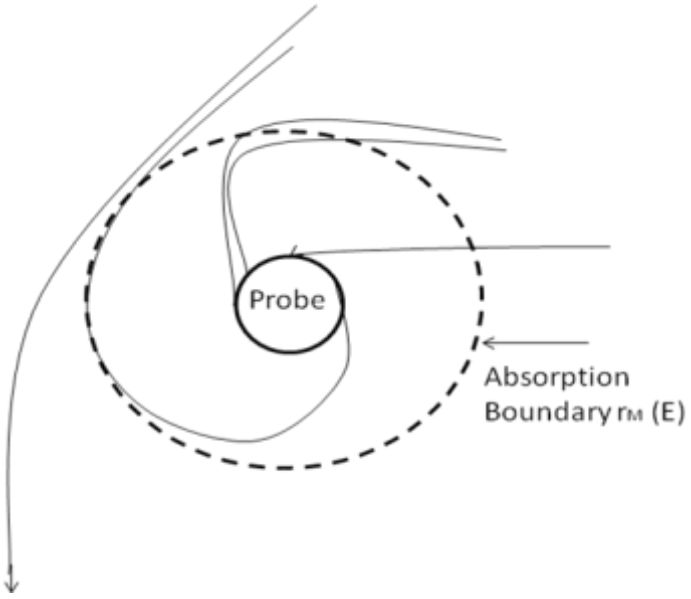

Figure 2.6. Definition of absorption radius

If $T_i = 0$ or $E_i = 0$ one would expect that BRL computations will converge on to the ABR results. However, this happens only for spherical probes. For cylindrical probes, there is a problem of nonuniform convergence. Since the angular momentum is Mvr, for $r \rightarrow \infty$ ions with zero thermal velocity have $J = (M)(0)(\infty)$, an indeterminate form. To overcome that is to calculate the probe current for $T_i > 0$ and then take the limit $T_i \rightarrow 0$, as BRL have done. It should be noted that Chen pointed out the fact that the BRL predictions have been borne out in experiments in fully ionized plasmas, but not in partially ionized ones.

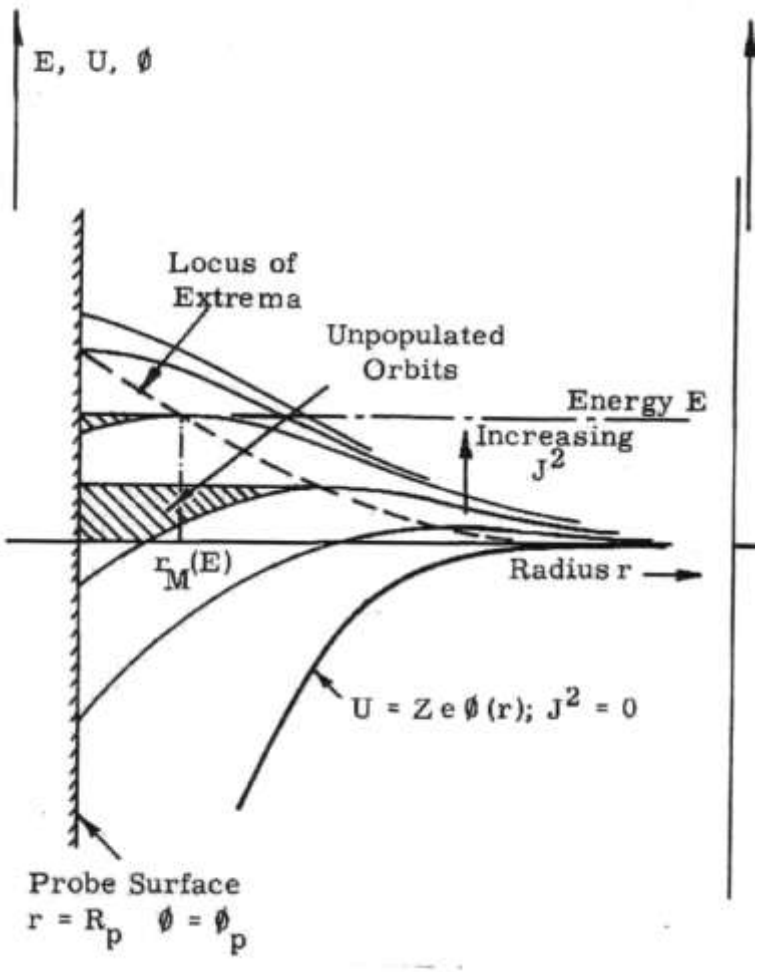

Figure 2.7. Effective potential seen by ions with angular momentum J[1]

2.2.8. Comparison Among Theories

A comparison between the plasma densities obtained by using a Langmuir probe and measurements made with microwave interferometry. Regarding the Langmuir probe the plasma densities will be computed using both ABR and BRL methods. Such a comparison is shown in fig. 2.8. By comparing between the ABR and BRL theories, it appears that the ABR

theory under-predicts the density because orbiting is neglected, and therefore the predicted current is too high and the measured current is identified with a lower density. On the other hand, BRL theory over predicts the density because it assumes more orbiting than what actually occurs, so that the measured current is identified with a high density.

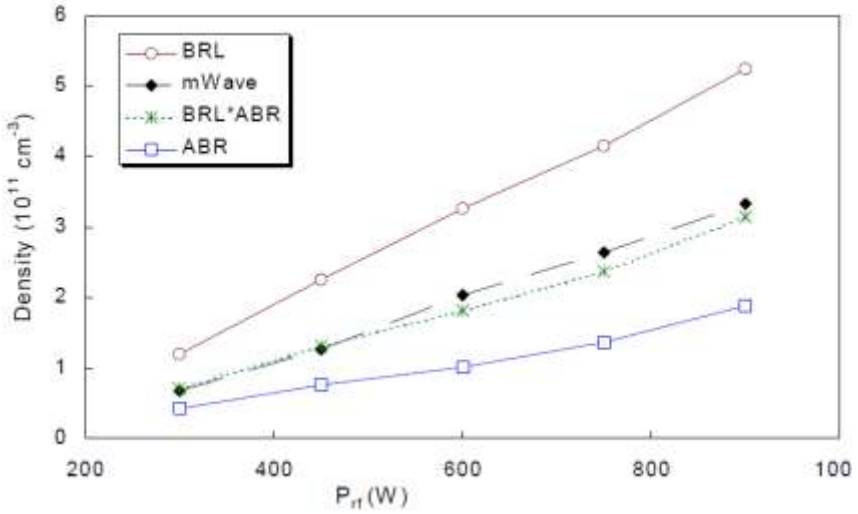

Figure 2.8. Comparison of n measured with microwaves with probes using two different probe theories[6]

This effect occurs in partially ionized plasmas because the ions suffer collisions far from the probe, thus losing their angular momentum. The BRL theory assumes that there is no change in the angular momentum of the ions all the way in from infinity. One might expect the real density to lie in between, and indeed, it agrees quite well with the geometric mean of the BRL and ABR densities[6].

2.3. Electron Retardation

2.3.1. Electron Current

It was first presented by Langmuir that a measurement of d^2I/dV_p^2 as a function of V_p enables the electron velocity distribution to be found. Druyvesteyn further carried on the work and analyzed the cases of cylindrical and planar probes and suggested that this expression should also apply to non-concave probe. Kagan presented the following simplified analysis confirming Druyvesteyn's conclusion.[2,10]

The following derivation was carried out by Swift and Schwar. If $f(1/2m_ev^2)4\pi v^2dv$ represents the number of electrons in unit volume of the plasma having speeds in the range v to $v+dv$ the number of such electrons that travel in the θ to $\theta+d\theta$ and φ to $\varphi+d\varphi$ direction is

$$f(\frac{1}{2}m_ev^2)v^2\sin\theta d\theta d\varphi dv \tag{2.37}$$

The flux of these electrons crossing an area δA_p of the probe's surface per second is then

$$\delta A_p f_p(\frac{1}{2}m_ev^2)v^3\cos\theta\sin\theta d\theta d\varphi dv \tag{2.38}$$

where $f_p(1/2m_ev^2)$ is the electron velocity distribution function at the probe's surface. The net electron current reaching the whole probe surface from all possible directions and over the complete speed range is

$$I_e = -A_pe\int_0^{\pi/2}\int_0^{2\pi}\int_0^{\infty} f_p(\frac{1}{2}m_ev^2)v^3\cos\theta\sin\theta d\theta d\varphi dv \tag{2.39}$$

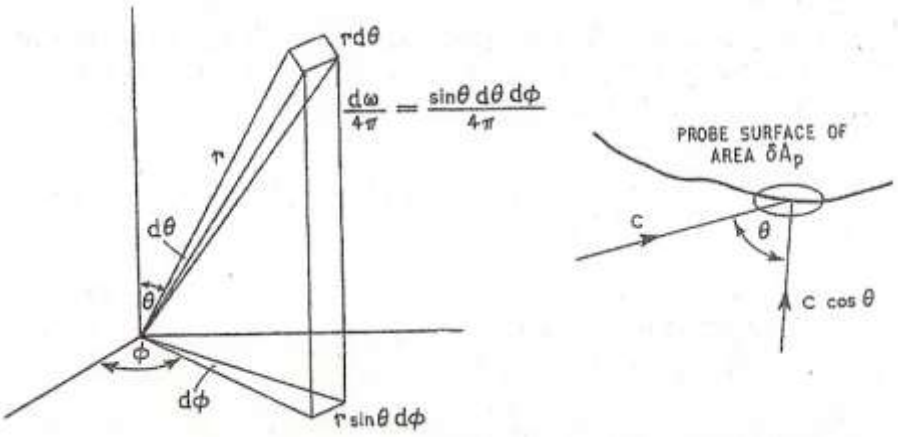

Figure 2.9. Co-ordinate system showing fraction of electrons moving in directions θ to $\theta+d\theta$ and φ to $\varphi+d\varphi$ and reaching an area δA_p in unit time[1]

In order for us to assume an isotropic case (the electrons can reach the point in question from any direction), the dimensions of the probe must be very much smaller than the electron mean free path. The limits of θ of 0 and $\pi/2$ are intended to make the analysis tractable and simply mean that the probe contains no re-entrant areas. The electron speed v in eq. 2.39 refers to the value at the probe's surface. On carrying out the integration over θ and φ eq. 2.39 reduces to

$$I_e = -A_p e\pi \int_0^\infty f_p(\frac{1}{2} m_e v^2) v^3 dv \qquad (2.40)$$

Providing the distribution function is isotropic and homogeneous it is a function only of the electron's energy. If no collisions occur the total energy of an electron remains unchanged. Hence, if the potential drop between the probe and plasma occurs over a distance much less than a mean free path, it follows that over this last mean free path next to the probe there must be not only conservation of the total electron energy E but also a constant electron distribution function. Now

$$E = \frac{1}{2} m_e v^2 - eV \tag{2.41}$$

Thus v must decrease as the electron approaches the probe since V is becoming progressively more negative. Also

$$f(E) = f_p(\frac{1}{2} m_e v^2) \tag{2.42}$$

$$f_p(\frac{1}{2} m_e v^2) = f(\frac{1}{2} m_e v^2 - eV_p) \tag{2.43}$$

where v again refers to the electron speed at the probe's surface. Rewriting eq. 2.40 then gives

$$I_e = -A_p e\pi \int_0^\infty f(\frac{1}{2} m_e v^2 - eV_p) v^3 dv \tag{2.44}$$

From eq. 2.41 we obtain $v^2=2(E+eV_p)/m_e$ and $v\,dv=dE/m_e$. Hence eq. 2.44 becomes

$$I_e = -A_p \frac{2e\pi}{m_e^2} \int_{-eV_p}^\infty f(E)(E + eV_p) dE \tag{2.45}$$

This becomes on differentiating once with respect to V_p

$$\frac{dI_e}{dV_p} = -A_p \frac{2e^2\pi}{m_e^2} \int_{-eV_p}^\infty f(E) dE \tag{2.46}$$

Differentiating again gives

$$\frac{d^2 I_e}{dV_p^2} = -A_p \frac{2e^2\pi}{m_e^2} e[f(E)]_{E=-eV_p}, \quad V_p < 0 \tag{2.47}$$

i.e.

$$\frac{d^2 I_e}{dV_p^2} = -A_p \frac{2e^2\pi}{m_e^2} e[f(E)]_{E=-eV_p}, \quad V_p < 0 \tag{2.48}$$

Thus a plot of d^2I_e/dV_p^2 versus V_p shows how $f(E)$ varies with E. $f(E)$ is the velocity distribution function. To convert to an energy distribution function $f_1(E)$ we use the relation

$$f_1(E)dE = 4\pi v^2 f(E)dv \tag{2.49}$$

where $f_1(E)dE$ is the number of electrons per unit volume in the energy range E to $E + dE$ and $E=1/2m_ev^2$. Hence:

$$[f_1(E)]_{E=-eV_p} = -\frac{4}{A_p e^2}\left(\frac{-m_e V_p}{2e}\right)^{1/2}\frac{d^2I_e}{dV_p^2} \tag{2.50}$$

It is worth mentioning that Kagan is simply stating that the probe does not perturb the distribution function prior to measurement. His method of analysis which takes into account the spherical coordinates supports the conclusion reached by Druyvesteyn. At this point there is a big distinction between our work and Kagan's work since the conclusion we are trying to reach is that it is the efficiency of collection as a function of energy that needs to be considered. This is done by taking the geometry of the probe into consideration. This point will be discussed further in the next following chapters.

2.3.2. Methods of Determining the Second Derivative

There are a number of ways of finding the second derivative of the electron current flowing to a negative probe. In this section we shall discuss the principle of these different methods. In the electron retarding region, due to the difference in mass between electrons and ions with electrons being lighter, the change in electron current due to varying the bias on the

probe is very much greater than the corresponding changes in positive ion current even for moderately large electron retarding potentials. Usually, therefore, electron energy distributions can be measured up to large energies by assuming that

$$\frac{d^2|I_e|}{dV_p^2} \gg \frac{d^2|I_+|}{dV_p^2} \tag{2.51}$$

i.e. the second derivative of the circuit current is essentially the same as the second derivative of the electron current.[2]

When the probe to plasma potential is zero, all electrons, regardless of their energy, can reach the probe while when the probe potential is strongly negative only the highly energetic electrons that can overcome the retarding potential will be able to reach the probe. In practice it is difficult to determine when V_p is zero as the probe potential is always measured relative to a reference electrode, therefore in order to set an origin point one must first determine the plasma potential V_o. If V_o remains constant it has no effect on the actual shape of the second derivative curve. Fig. 2.10 shows the zero, first and second derivatives for planar, cylindrical and spherical probes when the electrons possess a Maxwellian velocity distribution and the flow of electrons and the ions is governed by orbital motion. These graphs were deduced from the differentiation of eqs. 2.16 and 2.21. In the next section we will discuss two methods of determining d^2I_e/dV_p^2.

2.3.2.1. Graphical Differentiation

The simplest method of determining the derivative of a probe characteristics is to differentiate it graphically. As might be expected, the main source of error in this type of analysis lies in the accuracies involved in the two successful graphical differentiations of an experimentally determined probe characteristic. The reason for such error might rise from the fact that any wrong differentiation of the first graph would be carried out to the second and thus causing the error to propagate. A rather elaborate procedure for doing this has been proposed by Medicus.[16]

2.3.2.2. Differentiating Circuits

Unlike the method mentioned above which is carried manually, this method overcomes the rather tedious procedure mentioned above by arranging for the differentiation to be carried out electrically. The method is based on measuring the probe current while the probe potential varies linearly with time. Thus, if V_p can be written as

$$V_p = xt \tag{2.52}$$

$$\frac{dI_e}{dV_p} = \frac{1}{x}\frac{dI_e}{dt} \tag{2.53}$$

The output from the first differentiating circuit which is dI_e/dt may again be differentiated by feeding into another differentiating circuit. The output from the second differentiation circuit will give a signal proportional to d^2I_e/dV_p^2 as shown in figure 2.11.

A major assumption has been made that I_e varies instantaneously with V_p, i.e. the electrons are always in equilibrium with the applied field. In practice this is not the case,

where if an instantaneous potential is applied between the probe and plasma there will be some finite time before the electrons can rearrange to their new equilibrium state.

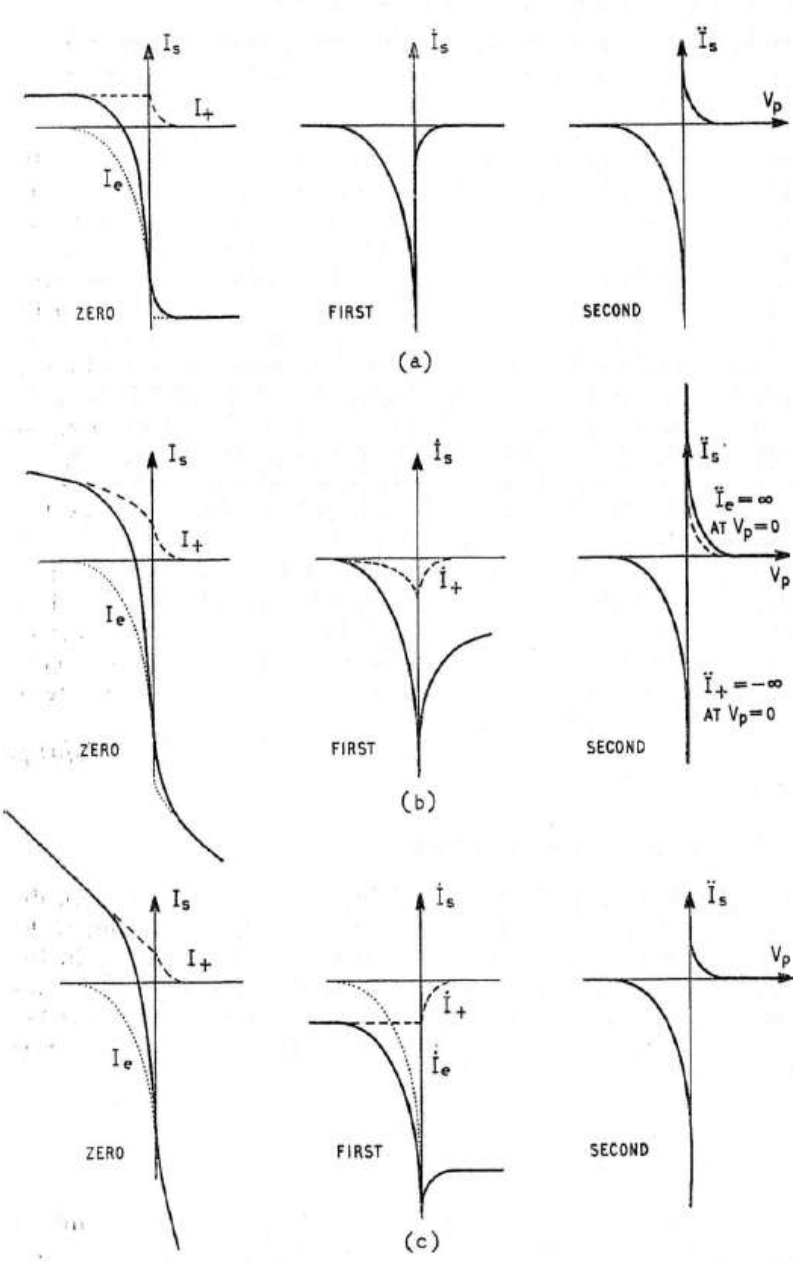

Figure 2.10. Zero, first, and second derivatives of (a) planar (b) cylindrical (c) spherical probe current characteristics assuming orbital motion and a Maxwellian velocity distribution[2]

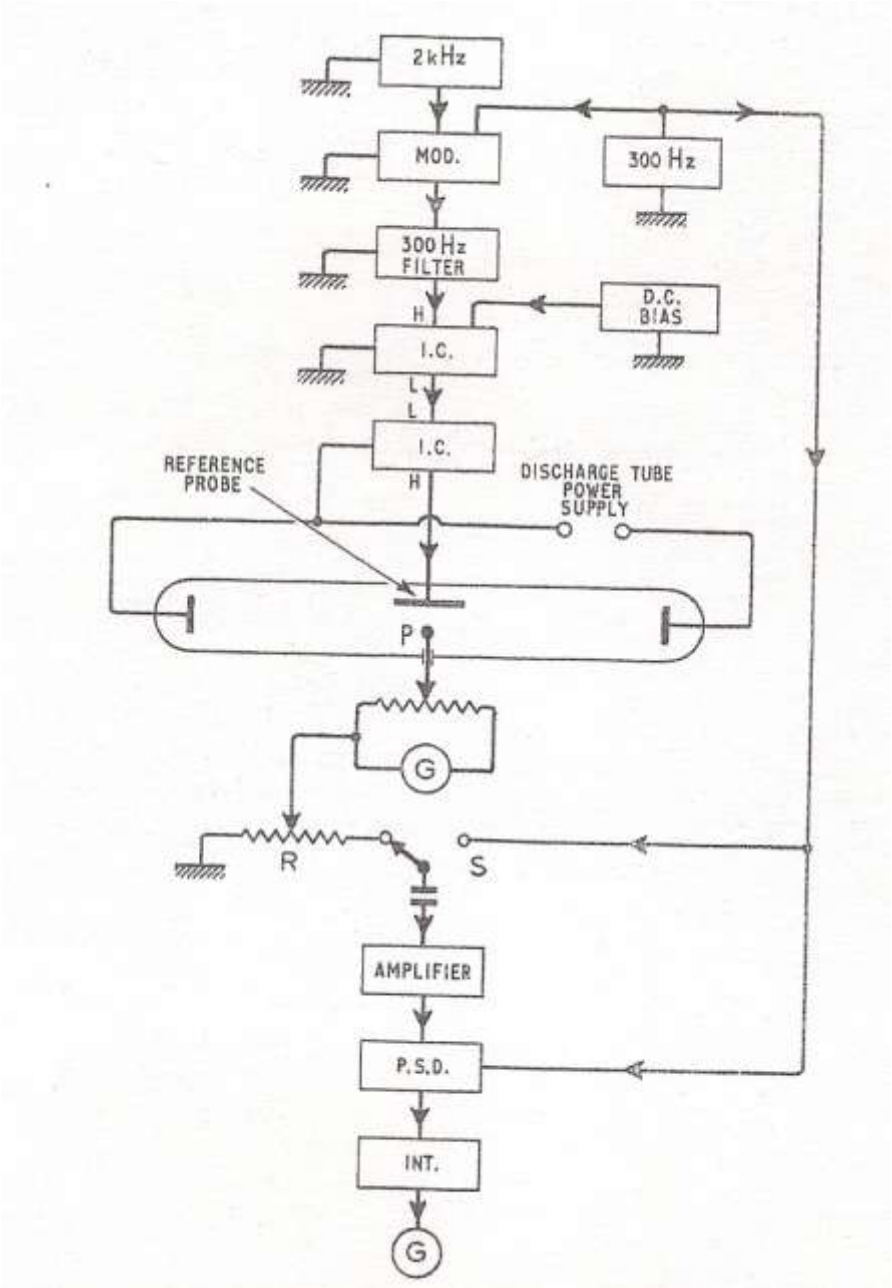

Figure 2.11. Circuit for obtaining second derivative of a probe current versus potential characteristic using a small amplitude sine-wave modulated potential difference.[2]

2.4. Probe Contamination

Consider the case where a layer of impurities is covering the probe. This layer of impurity has a resistance R. If the probe is biased to a voltage V_B, the actual bias that is applied to the surface in contact with the plasma will be reduced to V_B-IR, where I is the net current. In the case where the probe is biased at low potentials, i.e. near the floating potential, the net current will be small and the applied bias will be close to the actual bias. On the other hand, when the probe is biased at V_p, the actual potential will be V_p-I_e R. And due to the fact that the current will be greater than in the case of low potentials, the actual bias will not equal V_p until the applied bias is greater than V_p+I_e R. It is apparent that in this case the plasma potential determined from the knee of the measured I-V characteristic will be overestimated causing the overestimation of the electron temperature as well. The error in this case will depend on the value of R, of the resistive layer.

Impurities can also cause another source of error in the determination of the plasma potential from the knee. This error appears as variations in the surface work function. Variations in the surface work function can be as large as 1 V. Probe contamination is often apparent in hysteresis in I-V characteristics as shown in figure 2.12.

One of the best techniques to get rid of impurities is to heat the probes red to white hot by biasing probes more positive than V_p. However, for very low pressures ~10^{-6} torr, monolayers of contaminants can form in several minutes and cleaning must be carried out often.[12]

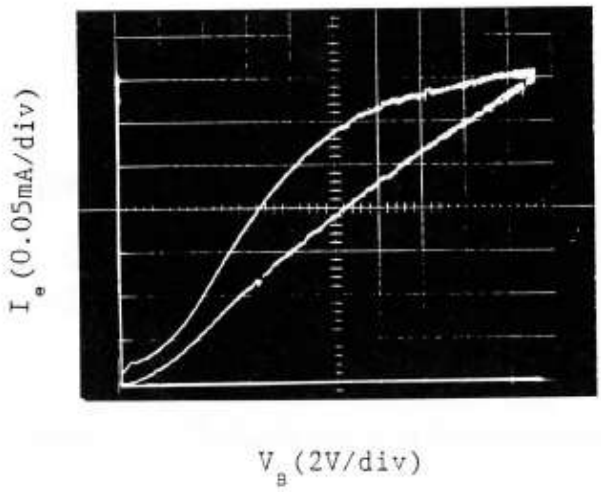

Figure 2.12. I-V characteristic of a dirty probe showing hysteresis[12]

2.5. Secondary Electron Effects

Secondary electron emission plays a key role in plasma production in many plasma processing devices. Since secondary electrons can result from either electron or ion bombardment they will have an important effect in determining the probe characteristics. Before talking about secondary electron effects we need to identify an important factor which is the secondary electron emission coefficients $\sigma(E)$. The secondary electron emission coefficients are defined as the ratio of emitted to incident current and depend on the incident particle energy. For clean surfaces, they can be greater than 1.0 for ion energies greater than 1 keV or for incident electron energies of several hundred eV. It should be noted that dirty surfaces as well as insulators tend to have higher secondary electron emission coefficients than conductors. Another source of secondary electron emission is photoemission.

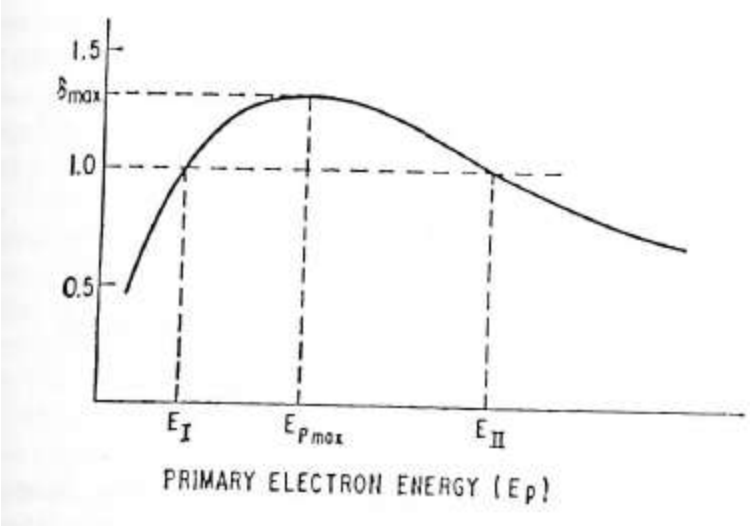

Figure 2.13. Schematic description of the variation of the electron secondary electron emission coefficient versus incident electron energy[12]

Consider secondary electron emission caused by monoenergetic primary electrons. The secondary electron emission coefficient σ of most metals increases with incident electron energy in the order of several hundred eV to a maximum value and then starts to decrease with increasing incident energy as shown in figure 2.13.

The effect on Langmuir probe *I-V* characteristics can be estimated by representing the curve in fig. by $\sigma \approx \delta\varepsilon/E_0$, where $E_0 \approx 200eV$ for tantalum. This is a reasonable approximation for $\varepsilon < 150eV$. The derivation below was carried out by Hershkowitz. The secondary electron current density can be written

$$j_s(V_B) = \frac{e2\pi}{m_e^2}\int \varepsilon f(\varepsilon)[\frac{1-e(V_p - V_B)}{\varepsilon}]\sigma(\varepsilon_w)d\varepsilon \qquad (2.55)$$

where σ is evaluated at ε_w, the kinetic energy that the incident primary electrons have at the probe. Conservation of energy gives

$$\varepsilon_w = E_p - e(V_p - V_B) \tag{2.56}$$

The ratio of secondary current to primary current can be written

$$\frac{j_s}{j_p} = \frac{E_p}{E_0}\delta[1 - e(V_p - V_B)/E_p] \tag{2.57}$$

If j_p is comparable to the bulk electron background current density, the condition for significant secondary electron emission is that E_p is the order of E_0.[12] It can be shown that a similar result holds for Maxwellian electrons.[13]

Figure 2.14 represents data for a tantalum probe immersed in plasma with monoenergetic electrons. The secondary electron emission current resembles an additional ion collection current. As the probe bias voltage is swept, the curve falls below 0A, indicating significant electron emission. It should be noted that secondary electron emission gives rise to a greater slope below the knee. When energetic electrons are present, the contribution of secondary electrons should be taken into consideration.[12,14,15]

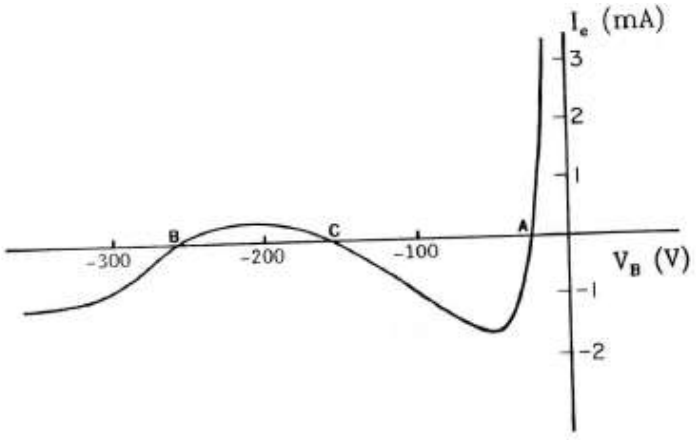

Figure 2.14. I-V characteristics of a tantalum probe with 300 eV primary electrons and 5 eV plasma electrons at an argon neutral pressure of 2×10^{-5} torr. The net current equals 0 at A, B, and C.[12]

2.6. Summary

Although the thesis is mainly about improving the EEDF calculated from the electron current extracted from plasma (I-V curve), but one important aspect of the I-V curve is that it represents both ion and electron currents. In some cases the ion current is small and can be neglected but in most cases the ion current contributes significantly and needs to be dealt with. In this chapter the focus was divided into two parts. The first part dealt with the ions' contribution to the Langmuir probe, and the previous work carried out by reputable scientists in the field in trying to identify a number of theories to subtract the ion contribution from the I-V curve. Although the discussion was brief, we mainly focused on the important theories out in the field. The second part dealt with the most common technique in extracting EEDF from the I-V curve, which is the second derivative. Also we introduced a number of concepts such as secondary emission as well as probe contamination. The reason for the second portion of this chapter is to act as an introduction to chapter 3 which will deal with our work regarding EEDFs and the improvements we added compared to what is being used in the field today.

2.7. References

[1] Laframboise J., "Theory of Spherical and Cylindrical Langmuir Probes in a Collisionless, Maxwellian Plasma at Rest", PhD. Thesis, 1966.

[2] Swift J. D., Schwar M. J., "Electrical Probes for Plasma Diagnostics", American Elsevier Publishing Company, 1971,ch. 4.

[3] Hoskinson A. R., Hershkowitz N., "Effect of Finite Length on the Current-Voltage Characteristic of a Cylindrical Langmuir Probe in a Multidipole Plasma Chamber", *Plasma Source Science and Tech.,* 15(1), 2006, pp. 85-90.

[4] Mott-Smith and Langmuir; "The Theory of Collectors in Gaseous Discharges", *Phys. Rev.*, 28,1926, pp. 727-763.

[5] Allen J. E., "Probe Theory- The Orbital Theory Approach", *Phys. Scr.,* 45, 1992, pp.497-503.

[6] Chen F., Chang P.,"Lecture Notes on Principals of Plasma Processing", Plenum Kluwer Publisers, 2002, ch. 7.

[7] Allen J. E., Boyd R. F., Reynolds P., "The Collection of Positive Ions by a Probe Immersed in a Plasma ", *Proc. Physics Soc. B,* 70, 1957, pp. 297-304.

[8] Chen F. F., "Numerical Computations for Ion Probe Characteristics in a Collisionless Plasma", *Journal of Nuc. Energy Part C*, 7 (1), 1965, pp. 47-68.

[9] Bernstein I. B., Rabinowitz I., "Theory of Electrostatic Probes in a Low Density Plasma", *Phys. Fluids*, 2, 1959, pp. 112-121.

[10] Kagan M., and Perel, "Probe Methods in Plasma Research", *Usp. Fiz. Nauk.*, 81, 1963, pp. 409-452.

[11] Langmuir I., Compton K.T., "Electrical Discharges in Gases, Part II. Fundamental Phenomena in Electrical Discharges", *Rev. Mod. Phys.*, 3, 1931, pp. 191-257.

[12] "Plasma Diagnostics Discharge Parameters and Chemistry", Edited by Orlando Auciello, and Daniel Flamm, Academic Press Inc,vol. 1, 1989,ch. 3.

[13] Wang E. Y., Hershkowitz N., Intrator T., "Direct Indication Plasma Diagnostic Based on Secondary Electron Emission", *Rev. Sci. Instrum.*, 57, 1986, pp. 1085-1089.

[14] Nam C., Hershkowitz N., Cho M., Intrator T., and Diebold D., "Multiple Valued Floating Potential s of Langmuir Probes", *J. Appl. Phys.*, 63, 1988, pp. 5674-5677.

[15] Griskey M., Stenzel R., “Secondary-Electron-Emission Instability in a Plasma”, *Phys. Rev Lett.*, 82, 1999, pp.556-559.

[16] Medicus G., “Simple Way to obtain the Velocity Distribution of the Electrons in Gas Discharge Plasmas from Probe Curve”, *J. Appl, Phys*., 27, 1956, pp.1242-1248.

CHAPTER 3

The Electron Energy Distribution Function as an Integral Problem

3.1. Introduction

The derivative formulation of Druyvesteyn combined with an assumption of geometry invariance posed by both Druyvesteyn and Kagen and the relative ease of data smoothing and analog differentiation have made the derivative solution for EEDF analysis the preferred method for experimentalists. Druyvesteyn built his theory on the fact that the second derivative works well for both spherical and cylindrical probes and can be extended to planar probes. This geometry invariance assumes that both the spherical and cylindrical coordinates will behave the same if applied on a Langmuir probe in plasma. Adding to geometry invariance the use of smoothing methods such as Savitzky-Golay filter which in part removes data from the I-V curve based on the noise level suggested by the user. The combination of both methods lead to major errors in the EEDF.

Recently, electron energy distribution function (EEDF) extraction techniques have been evaluated using regularized solutions to the integral problem. These techniques do not assume any mathematical representation of the EEDF and solve the integral problem for any function that best represents the EEDF. Also, unlike the more widely used point-by-point extraction of the second-derivative relationship, the integrated relationship between electron current and the EEDF is used, instead of a relatively small fraction of the integrated data in

the point-by-point method. In 1930, Druyvesteyn derived the relationship between the electron energy distribution in a plasma and the electron current measured by a biased Langmuir probe [1]:

$$f(E)_{E=-eV_{probe}} = -\frac{4}{A_p e^2}\sqrt{-\frac{m_e V_{probe}}{2e}}\frac{d^2 I_e}{dV_{probe}^2} \tag{3.1}$$

where I_e is the electron contribution to the current collected by the Langmuir probe, A_p is the area of the probe, e is electron charge, m_e is electron mass, V_{probe} is the potential of the probe (referenced to the plasma potential), and $f(E)$ is the EEDF, or the number of electrons per cm^3 with total energy between E and $E+dE$.

The well-known relationship dating to Druyvesteyn between the I-V characteristic and the EEDF is a Fredholm integral of the first kind, and can be rewritten in a similar integral form:

$$I_e = -\frac{A_p e}{4}\sqrt{\frac{2}{m_e}}\int_{-eV_{probe}}^{\infty}\frac{f(E)\left(E+eV_{probe}\right)}{\sqrt{E}}dE \tag{3.2}$$

Where eqs. 3.1 and 3.2 are identical representations of electron current to a probe for spherical geometries from which the Druyvesteyn relation is derived. Eq. 3.2 has the form $f(x) = \int K(x,y)g(y)dy$ [2]. This family of integral problems are often cited as a classic example

of a linear inverse problem [2] in which one attempts to construct modeled theory (here, the EEDF) from data (here, collected current and applied voltage). By descretizing the electron current and EEDF (something that is typically done in the age of digital data acquisition anyhow), this integral can be reduced into a system of algebraic linear equations of the form

$$I_e = Kf \tag{3.3}$$

where I_e is the electron current data in vector of length M, K is an $M \times N$ matrix with a large condition number $M \geq N$, and f is the EEDF in vector length N[3]. Algebraic problems in the form shown above are considered discrete ill-posed problems based on the fact that the matrix K is ill-conditioned[2,4]. In the upcoming sections ill-posed problems will be discussed in detail.

3.2. Ill-Posed Problems

The concept of well-posed and ill-posed problems was first introduced by Hadamard at the beginning of the 19th century.[41] Hadamard defined a problem as ill posed if the solution is not unique or if it is not a continuous function of the data—i.e., if any small perturbation of the data can cause a large perturbation of the solution. Hadamard did not believe that ill-posed problems would describe physical systems. Since then this class of problems has been shown to give a better insight into physical systems, and today ill-posed

problems take the form of inverse problems in many areas of science and engineering. Inverse problems appear in determining the internal structure of a physical system from the system's measured behavior, or in determining the unknown input that gives rise to a measured output signal (in contrast to direct case where the system's behavior is sought out given the input or internal structure). Some examples are acoustics, astrometry, computerized tomography, continuation problems, early vision, electromagnetic scattering, geophysics, inverse geo- and helioseismology, mathematical biology, optics and image restoration, remote sensing, inverse scattering theory, signal processing, and statistics.[2,5 → 14]

The main discussion of this general introduction will be on linear inverse problems that can be formulated in the following very general form:

$$\int_{\Omega} input * system \, d\Omega = output \tag{3.4}$$

In this formulation, having the *input* and the mathematical description of the system, the direct problem is to compute the *output*. The goal of the inverse problem is not to determine the *output* as is the case with the direct problem but to determine either the *input* or the *system*. For example, in astronomical image deblurring the "*input*" is the night sky, the blurring "*system*" consists of the telescope and the atmosphere, and the "*output*" is the recorded blurred image. The goal is to reconstruct the *"input"* which is in this case the unblurred image of the night sky, given a mathematical description of the blurring effects caused by the telescope and the atmosphere. Another example is computerized tomography, where the "*input*" is in this case the true image, the "*system*" is the geometry, and the

"*output*" is the projection image. The goal here to reconstruct the *"system"*, from information about the locations of the X-ray sources and measurements of their damping.[2]

The classical example of a linear ill-posed problem is a Fredholm integral equation of the first kind[1] with a square integrable kernel [15], which can always be written in the generic form

$$\int_0^1 K(x,y)\,f(y)dy = g(x), \qquad 0 \le x \le 1 \tag{3.5}$$

where *g(x)* the output, and the kernel *K(x,y)* are known functions, at least in principle, while *f* is the unknown *input*, sought solution. In many practical applications, the kernel *K* is given exactly by the underlying mathematical model, while the right-hand side *g* typically consists of measured quantities; i.e., *g* is only known with a certain accuracy and only in a finite set of points x_1,..., x_m.[2]

3.2.1 The Singular Value Expansion

One of the best analytical tools for analysis of first-kind Fredholm integral equations with square integrable kernels is the singular value expansion (SVE) of the kernel. A kernel *K* is square integrable if the norm

$$\|K\|^2 = \int_0^1 \int_0^1 K(x,y)^2\,dxdy \tag{3.6}$$

is bounded. By applying the SVE, any square integrable kernel *K* can be written in the form of an infinite sum:

$$K(x,y) = \sum_{i=1}^{\infty} \mu_i u_i(x) v_i(y) \tag{3.7}$$

Note that for degenerate kernels, the ∞ should be replaced by the rank of the kernel. The functions u_i and v_i are termed the singular functions of K.[2] They are orthonormal with respect to the usual inner product, i.e.,

$$(u_i, u_j) = (v_i, v_j) = \begin{cases} 1 & if \quad i = j \\ 0 & if \quad i \neq j \end{cases} \tag{3.8}$$

where (u_i ,u_j) and (v_i , v_j) is defined by

$$(\phi, \vartheta) = \int_0^1 \phi(t)\vartheta(t)dt \tag{3.9}$$

The numbers μ_i are the singular values of K: they are always positive and they can always be ordered in a decreasing order such that

$$\mu_1 \geq \mu_2 \geq \mu_3 \geq .....\geq 0 \tag{3.10}$$

The singular values satisfy the relation $\sum_{i=1}^{\infty} \mu_i^2 = \|K\|^2$.[2] The triplets { μ_i, u_i, v_i } are related to the following two eigenvalue problems associated with the kernel K: { $\mu_i{}^2$, μ_i } are the eigensolutions of the symmetric kernel $\int_0^1 K(x,z)K(y,z)dz$, while { $\mu_i{}^2$,v_i } are the eigensolutions of $\int_0^1 K(z,x)K(z,y)dz$. These eigensolutions establish the condition that the triplets { μ_i, u_i, v_i } are characteristic and essentially unique for the given kernel K.[2]

The following relation helps illustrate how singular values and functions relate to each other:

$$\int_0^1 K(x,y)v_i(y)dy = \mu_i u_i(x), \qquad i = 1,2,... \tag{3.11}$$

Eq. 3.11 represents the fact that any singular function v_i is mapped onto the corresponding u_i, and that the singular value μ_i acts as an amplification of this particular mapping. If this relation, together with eq. 3.7, is inserted into the integral equation 3.5, then we obtain the equation

$$\sum_{i=1}^{\infty} \mu_i (v_i, f) u_i(x) = \sum_{i=1}^{\infty} (u_i, g) u_i(x) \tag{3.12}$$

which, in turn, leads to the following expression for the solution to eq. 3.5:

$$f(y) = \sum_{i=1}^{\infty} \frac{(u_i, g)}{\mu_i} v_i(y) \tag{3.13}$$

The only requirements for the existence of f is that the right-hand side of eq. 3.13 indeed converges, which is equivalent to requiring that g belong to R(K), the range of K. From eq. 3.13 we see that f is broken down to its singular functions v_i and the corresponding expansion coefficients μ_i^{-1} (u_i,g). Therefore the solution f can be characterized by an analysis of the coefficients μ_i^{-1} (u_i,g) and the functions v_i.[2,16]

3.2.2 The Smoothing Property of the Kernel

The overall behavior of the singular values μ_i and the singular functions u_i and v_i is by no means "arbitrary"; their behavior is strongly connected with the properties of the kernel K. The following holds as described by P.C. Hansen.[2]

- The "smoother" the kernel K, the faster the singular values μ_i decay to zero (where "smoothness" is measured by the number of continuous partial derivatives of K).

- The smaller the μ_i, the more oscillations (or zero-crossings) there will be in the singular functions u_i and v_i. This property is perhaps impossible to prove in general, but it is often observed in practice.

The practical application of the above properties of the triplets { μ_i, u_i, v_i } is that eq. 3.13 for *f* can be considered as a spectral expansion. This spectral expansion can better describe the spectral properties of the solution *f* through the coefficients μ_i^{-1} (u_i,g). It can be concluded from eq. 3.12 that the integration with *K* has a smoothing effect: the higher the spectral components in *f*, the multiplication of *g* with μ_i causes the spectral components to be more damped. Eq. 3.13 shows that the inverse problem of computing *f* from *g*, has the opposite effect on the oscillations in *g*, which is an amplification of the spectral components (u_i,g) with a factor μ_i^{-1} .[2]

The decay rate of the singular values μ_i can be used to diagnose the degree of ill-posedness of the problem. If there exists a positive real number λ such that the singular values satisfy $\mu_i = O(i^{-\lambda})$, then λ is called the degree of ill-posedness, and the problem is characterized as mildly or moderately ill posed if $\lambda <= 1$ or $\lambda > 1$, respectively.[2,17]

3.2.3 The Picard Condition and the Instability of the Solution

It should be stated that not every right-hand side *g* will lead to a "smooth" solution *f* due to the amplification factors μ_i^{-1}. The only case were the right-hand side in eq. 3.13 actually converges to *f* is when *g* is even more “smooth” than the input function *f*. The following Picard condition is essential to measure the smoothness of *g*.[2]

The Picard Condition states that there exists a square integrable solution *f* to the integral eq. 3.5, the right-hand side *g* must satisfy

$$\sum_{i=1}^{\infty}(\frac{(u_i, g)}{\mu_i})^2 < \infty \tag{3.14}$$

The Picard condition concludes that in order for a square integrable solution to exist, that from some point in the summation in eq. 3.13, the absolute value of the coefficients (u_i,g) must have a higher rate of decay than the corresponding singular values μ_i. Aready we showed that for *g* to be square integrable the coefficients (u_i,g) must decay faster than $i^{-1/2}$, but the Picard condition adds a more strict requirement on *g*, in that the coefficients (u_i,g) must decay faster than $\mu_i i^{-1/2}$. Since the Picard condition is important when talking about Fredholm integral equations of the first kind, it should be checked before one attempts to solve the integral equation.[2]

The requirement (eq. 3.14) in the Picard condition is identical to the requirement that the right-hand side *g* belong to R(K), the range of *K*. If there is a case where *g* has any small component outside R(K), then there is no square integrable solution. Consider a $g \notin R$(K), and let g_k denote the approximation to *g* obtained from truncating its SVE expansion after *k* terms,

$$g_k(x) = \sum_{i=1}^{k}(u_i, g)u_i(x) \tag{3.15}$$

This g_k clearly satisfies the Picard condition for all k = 1, 2,..., and the corresponding approximate solution f_k is given by

$$f_k(t) = \sum_{i=1}^{k} \frac{(u_i, g)}{\mu_i} v_i(t) \tag{3.16}$$

We conclude that as k —> ∞ we have g_k —> g, but

$$\| f_k \|_2 = (f_k, f_k)^{1/2} \to \infty \ \ as \ \ k \to \infty \tag{3.17}$$

It is exactly this lack of stability of f that makes the integral eq. 3.5 ill-posed.[2]

Unfortunately, in practical situations right-hand side g will be at best an approximate due to the fact that it is contaminated with unavoidable errors:

$$g = g^{exact} + \eta, \quad g^{exact} \in \Re(K), \quad \|\eta\|_2 \le \left\| g^{exact} \right\|_2 \tag{3.18}$$

Here, g^{exact} denotes the unknown, exact right-hand side and η denotes the perturbation (noise). In an ideal case, we want to compute $f^{exact} = \sum_{i=1}^{\infty} \mu_i^{-1} (u_i, g^{exact}) v_i$. We cannot expect the errors η to satisfy the Picard condition, and hence $g \notin R$(K). Any attempt to compute f^{exact} via the infinite sum $\sum_{i=1}^{\infty} \mu_i^{-1} (u_i, g) v_i$ will either diverge or return a useless result with extremely large norm, no matter how small the perturbation η is. Instead, it is necessary to use a regularization method that replaces the original problem (eq. 3.5) by a regularized problem which approximates the desired f^{exact}. If the perturbation turns out to be too big, compared to g^{exact} , then it is useless to compute an approximation to f^{exact}; hence, the assumption $\|\eta\|_2 \le \left\| g^{exact} \right\|_2$.[2,18]

3.3. Prelude to Regularization

As discussed in the previous section, the primary difficulty with ill-posed problems is that they are practically underdetermined due to the cluster of small singular values of *K*. Hence, it is important to incorporate further information about the desired solution in order to make the problem more stabilized and to single out a useful solution. This is the purpose of regularization.[2] Ideally there is an abundance of additional information in many types about the solution *f* to eq. 3.5 that the dominating approach to regularization is to allow a certain residual associated with the regularized solution, with residual norm

$$\rho(f) = \left\| \int_0^1 K(s,t) f(t) dt - g(s) \right\|_2 \tag{3.19}$$

and then use one of the following four schemes as mentioned by P.C.Hansen.[2]

1. Minimize $\rho(f)$ subject to the constraint that f belongs to a specified subset, $f \in S_f$.
2. Minimize $\rho(f)$ subject to the constraint that a measure $\omega(f)$ of the "size" of f is less than some specified upper bound δ, i.e., $\omega(f) < \delta$.
3. Minimize $\omega(f)$ subject to the constraint $\rho(f) < \beta$.
4. Minimize a linear combination of $\rho(f)^2$ and $\omega(f)^2$:

$$\min\{\rho(f)^2 + \alpha\omega(f)^2\}, \tag{3.20}$$

where α is a specified weighting factor. Here, α,δ, and β are known as regularization parameters, and the function ω is sometimes referred to as the "smoothing norm." The fourth scheme is the well-known Tikhonov regularization scheme. The idea behind all four schemes is that a regularized solution satisfying all constraints as well as having a small residual norm

will be not too far from the desired, unknown solution to the unperturbed problem.[2]

From a statistical point of view, the introduction of regularization decreases the size of the solution's covariance matrix at the cost of adding bias to the solution. In practice, the regularization problem should be discretized for it to be solved numerically. There are numerous methods to discretize integral equations, the two main classes of methods, namely, quadrature methods and Galerkin methods.[2] Both methods compute an approximation $\tilde{f}$ to *f*. In the quadrature, method, a quadrature rule with abscissas $y_1,...,y_n$ and corresponding weights $w_1,...,w_n$ is used to approximate an integral as

$$\int_0^1 \phi(y)dy \approx \sum_{j=1}^{n} w_j \phi(y_j) \tag{3.21}$$

and when this rule is applied to the integral eq. 3.5 for *m* distinct values $x_1,..., x_m$, then we obtain an *m x n* matrix *A* and a right-hand side *b* with elements given by

$$a_{ij} = w_j K(x_i, y_j), \quad b = g(x_i) \tag{3.22}$$

The solution vector is $(\tilde{f}(t_1),..., \tilde{f}(t_n))^T$, i.e., samples of $\tilde{f}$. In the Galerkin method, one chooses two sets of basis function φ_i and ψ_j, and then the matrix and right-hand side elements are given by

$$a_{ij} = \int_0^1 K(x,y)\varphi_i(x)\psi_j(y)dxdy, \quad b_i = \int_0^1 g(x)\varphi_i(x)dx \tag{3.23}$$

Solving the linear system of equations $A\zeta = b$ for the vector ζ, we obtain

$$\tilde{f}(y) = \sum_{i=1}^{n} \zeta_i \psi_i(y) \tag{3.24}$$

Some collocation methods are special cases of the Galerkin method with delta functions as the φ_i basis functions, $\varphi_i(x) = \delta(x - x_i)$. If K is symmetric and $\varphi_i = \psi_i$,, then A is symmetric and Galerkin's method is called the Rayleigh-Ritz method. [2]

When a rank-deficient or ill-posed problem is discretized, then the inherent difficulties are carried over to the discrete problem in the sense that the coefficient matrix will also have either a cluster of small singular values or singular values that decay gradually to zero. Hence, the discrete problem will also be effectively underdetermined. This is true for any discretization method. Therefore regularization is also required to solve the discretized problem. [2]

The most useful approach to adding regularization to the discrete problem is by discretizing the regularized problem. And as P.C. Hansen said "first regularize, then discretize".[2] this will lead in determining which information will actually be enforced on the regularized solution. Thus, if the discretization leads to a square system,

$$Ax = b, \quad A \in \Re^{mxn} \tag{3.25}$$

or an overdetermined system,

$$\min \|Ax - b\|_2, \quad A \in \Re^{mxn}, \quad m > n \tag{3.26}$$

where the vector x represents the function f. For example, the discrete Tikhonov regularization scheme becomes

$$\min\{\|Ax - b\|_2^2 + \lambda^2 \Omega(x)^2\} \tag{3.27}$$

The function Ω is termed the discrete smoothing norm, and it is often—but not always—of the form

$$\Omega(x) = \|Lx\|_2 \tag{3.28}$$

where the matrix L is typically either the identity matrix, a diagonal weighting matrix, or a p x n discrete approximation of a derivative operator (e.g., $\Omega(x) \approx \omega(f) = \|f^{"}\|_2$), in which case L is a banded matrix with full row rank. For example, for certain discretizations, the matrices[2]

$$L_1 = \begin{pmatrix} 1 & -1 & & \\ & \cdot & \cdot & \\ & & \cdot & \cdot \\ & & 1 & -1 \end{pmatrix} \in \Re^{(n-1)xn} \tag{3.29}$$

and

$$L_2 = \begin{pmatrix} 1 & -2 & 1 & & \\ & \cdot & \cdot & \cdot & \\ & \cdot & \cdot & \cdot & \\ & & \cdot & \cdot & \cdot \\ & & 1 & -2 & 1 \end{pmatrix} \in \Re^{(n-2)xn} \tag{3.30}$$

are scaled approximations to the first and second derivative operators. When $p < n$ then $\|L\ .\|_2$ is said to be a seminorm; i.e., there exist vectors $x \neq 0$ (in the null space of L) such that $\|Lx\|_2 = 0$. We stress that even when $\omega(f) = \|f\|_2$ the matrix L will depend on the discretization scheme used.[2]

If an *a priori* estimate x^* of the desired regularized solution is available, then this can be taken into account by including x^* in the discrete smoothing norm $\Omega(x)$, which then takes the form

$$\Omega(x) = \left\| L(x - x^*) \right\|_2 \tag{3.31}$$

In this way, the regularized solution will be biased towards the *a priori* estimate *x**, and the simple version of *Ω(x)* in eq. 3.28 is when *x* = 0*.[2,19]

3.4. EEDF Extraction by Regularization

In order to obtain the EEDF from Langmuir probe data, either an *a priori* assumption of the functional characteristics of the EEDF need to be assumed (Maxwellian, Druyvesteyn, etc.) or the differentiation of experimental data, complete with noise, needs to be carried out. A regularized solution makes global assumptions about the final solution. This methodology also uses the collective data obtained from the Langmuir probe over the range of applied voltages to extract the EEDF at a specific energy, as opposed to local perturbation-type analysis about a single point to obtain second-derivative information, as highlighted in eq.3.2.

3.4.1 Methodology

The first step is the formulation of the kernel *K* in eq. 3.5 for the EEDF integral problem. The methodology starts with the derivation of the electron current collected by a probe as a function of applied potential referenced to the plasma potential using eq. 3.2 and a step function distribution given by

$$f(E)=\begin{cases} 0 & if \quad E < E_L \\ \dfrac{n_e}{E_H - E_L} & if \quad E_L \le E \le E_H \\ 0 & if \quad E > E_H \end{cases} \tag{3.32}$$

where n_e is the density of electrons (assumed to be constant) between a low energy limit E_L and a high energy limit E_H. If this distribution function is inserted into the Druyvesteyn derivation of electron current for an arbitrary EEDF (eq. 3.33), the relationship between the electron current I_e and the term n_e that defines the density of electrons in this energy band is derived below:[37]

$$f(E)_{E=-eV_{probe}} = -\frac{4}{A_p e^2}\sqrt{-\frac{m_e V_{probe}}{2e}}\frac{d^2 I_e}{dV_{probe}^2} \tag{3.33}$$

Assuming that $V_{probe} = V_{plasma} - V = -E/e$, and reducing the distribution function to

$$f(E) = -\frac{4}{A_p}\sqrt{\frac{m_e E}{2e^2}}\frac{d^2 I_e}{dE^2} \tag{3.34}$$

Isolating the derivative of the current gives

$$\frac{d^2 I_e}{dE^2} = \frac{A_p e}{4}\sqrt{\frac{2}{m_e E}}f(E) \tag{3.35}$$

From (3.35) for $E<E_L$, $f(E)=0$ therefore

$$\frac{d^2I}{dE^2}=0 \tag{3.36}$$

$$\frac{dI}{dE}=C_1 \tag{3.37}$$

$$I(E)=C_1\times E+C_2 \tag{3.38}$$

for $E_L \le E \le E_H$, f (E)=n_e /E_H –E_L , therefore

$$\frac{d^2I}{dE^2}=\frac{n_e}{E_H-E_L}\times\frac{A_p e}{4}\sqrt{\frac{2}{m_e E}} \tag{3.39}$$

$$\frac{dI}{dE}=\frac{n_e}{E_H-E_L}\times\frac{A_p e}{2}\sqrt{\frac{2E}{m_e}}+C_3 \tag{3.40}$$

$$I(E)=\frac{n_e}{E_H-E_L}\times\frac{A_p e}{3}\sqrt{\frac{2E^3}{m_e}}+C_3\times E+C_4 \tag{3.41}$$

For $E>E_H$, $f(E)=0$, therefore

$$\frac{d^2I}{dE^2}=0 \tag{3.42}$$

$$\frac{dI}{dE}=C_5 \tag{3.43}$$

$$I(E)=C_5\times E+C_6 \tag{3.44}$$

So the current can be written in the following form

$$I_e(E)=\begin{cases} C_1\times E+C_2 & if \quad E<E_L \\ \dfrac{n_e}{E_H-E_L}\cdot\dfrac{A_p e}{3}\sqrt{\dfrac{2E^3}{m_e}}+C_3\times E+C_4 & if \quad E_L\le E\le E_H \\ C_5\times E+C_6 & if \quad E>E_H \end{cases} \tag{3.45}$$

Applying the following boundary conditions

1) The continuity of the zeroth derivative of the current at the boundaries.
2) The continuity of the first derivative of the current at the boundaries.
3) The assumption that the current for $E>E_H$ tends to zero.

Solving for the constants we obtain the following equation

$$I_e(E)=\begin{cases} \dfrac{n_e A_p e}{2(E_H-E_L)}\sqrt{\dfrac{2}{m_e}}\left[\left(\sqrt{E_L}-\sqrt{E_H}\right)E+\dfrac{\sqrt{E_H^{\,3}}-\sqrt{E_L^{\,3}}}{3}\right] & if \quad E<E_L \\ \dfrac{n_e A_p e}{6(E_H-E_L)}\sqrt{\dfrac{2}{m_e}}\left(2\sqrt{E^3}-3\sqrt{E_H}E+\sqrt{E_H^{\,3}}\right) & if \quad E_L\le E\le E_H \\ 0 & if \quad E>E_H \end{cases} \tag{3.46}$$

Which is referred to as (3.32) in the methodology.

Figure 3.1 shows a comparison between the methodology outlined above and the analytical solution of (3.46) for a Maxwell-Boltzmann distribution with electron density $N = 10^{10} cm^{-3}$ and $T_e = 3eV$. Note that the resulting electron currents for both cases are identical and also that a simple step function histogram representation of the EEDF is sufficient.

$$I_e(E) = \begin{cases} \dfrac{n_e A_p e}{2(E_H - E_L)} \sqrt{\dfrac{2}{m_e}} \left[\left(\sqrt{E_L} - \sqrt{E_H} \right) E + \dfrac{\sqrt{E_H^{\,3}} - \sqrt{E_L^{\,3}}}{3} \right] & if \quad E < E_L \\ \dfrac{n_e A_p e}{6(E_H - E_L)} \sqrt{\dfrac{2}{m_e}} \left(2\sqrt{E^3} - 3\sqrt{E_H} E + \sqrt{E_H^{\,3}} \right) & if \quad E_L \le E \le E_H \\ 0 & if \quad E > E_H \end{cases} \tag{3.47}$$

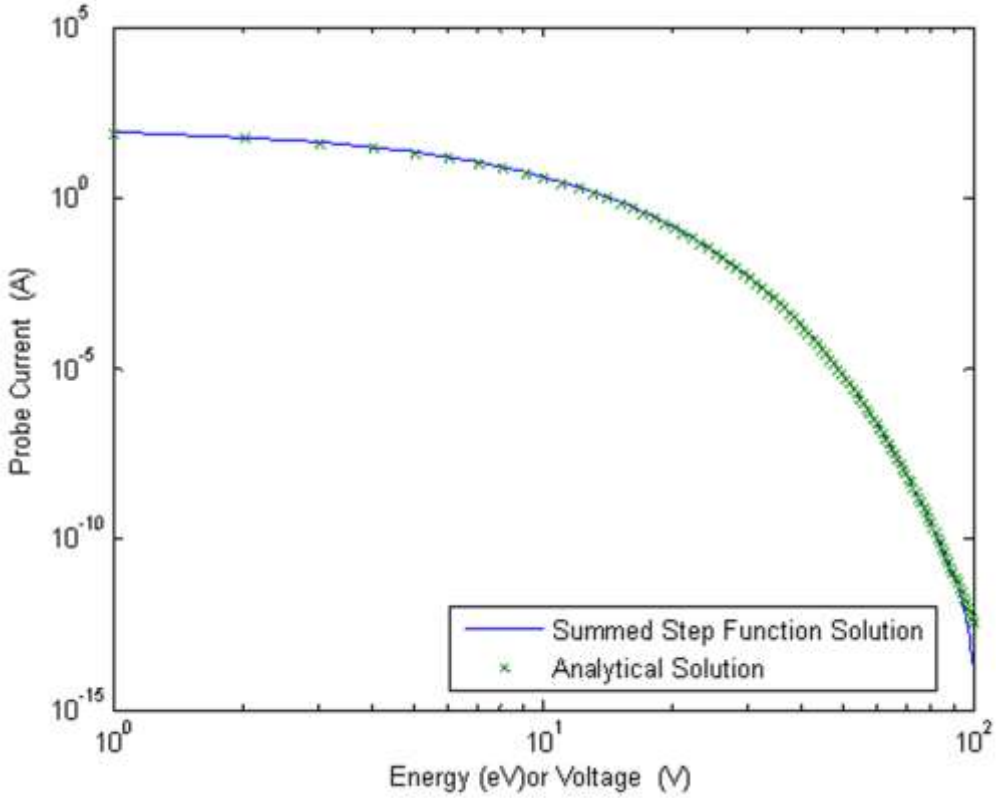

Figure 3.1. Comparison of electron current calculated using proposed methodology and analytical solution (dashed curve) for a 3eV Maxwellian distribution. Note that the analytical solution and the step function model give identical results.

These step functions can now be overlaid with arbitrary magnitudes of each step to form arbitrary electron energy distribution functions. A collective electron energy distribution function is now represented by:

$$f(E)=\sum_{i=1}^{N}\begin{cases}0 & if \quad E<E_{Li}\\ \dfrac{n_{ei}}{E_{Hi}-E_{Li}} & if \quad E_{Li}\le E\le E_{Hi}\\ 0 & if \quad E>E_{Hi}\end{cases} \tag{3.48}$$

where n_{ei}, E_{Hi}, and E_{Li} represent the magnitude, high energy limit, and low energy limit of each individual step function used to approximate the final distribution. Similarly, the total electron current can be represented by a similar summation over all step functions:

$$I_e(E)=\sum_{i=1}^{N}\begin{cases}\dfrac{n_{ei}A_p e}{2\left(E_{Hi}-E_{Li}\right)}\sqrt{\dfrac{2}{m_e}}\left[\left(\sqrt{E_{Li}}-\sqrt{E_{Hi}}\right)E+\dfrac{\sqrt{E_{Hi}^{3}}-\sqrt{E_{Li}^{3}}}{3}\right] & if \quad E<E_{Li}\\ \dfrac{n_{ei}A_p e}{6\left(E_{Hi}-E_{Li}\right)}\sqrt{\dfrac{2}{m_e}}\left(2\sqrt{E^{3}}-3\sqrt{E_{Hi}}E+\sqrt{E_{Hi}^{3}}\right) & if \quad E_{Li}\le E\le E_{Hi}\\ 0 & if \quad E>E_{Hi}\end{cases} \tag{3.49}$$

Now that the integral kernel K has been obtained for a step function, eq. 3.49 can be compared to the known electron current function produced by a known electron energy distribution function. In this case, a comparison of the electron current obtained using this methodology can be made to the expected electron current obtained analytically for a Maxwell-Boltzmann distribution,

$$I_e\left(V_{probe}\right) = -eA_p N\sqrt{\frac{kT_e}{2\pi m_e}}e^{\left(\frac{-eV_{probe}}{kT_e}\right)} \tag{3.50}$$

where k is the Boltzmann constant and T_e is the average temperature of the electrons defined by the Maxwell-Boltzmann distribution[20,21]. A step by step derivation of the methodology and comparison between the methodology outlined above and the analytical solution of eq. 3.50 can be found in the Appendix with the result that the electron currents for both cases are identical and that a simple step function histogram representation of the EEDF is sufficient.

The formulation of the set of eqs. 3.48, and 3.49 provide a mechanism to reduce this problem to a system of linear equations from which the EEDF can be solved. Equation 3.36 can be represented by a column matrix f, and the electron current obtained from the Langmuir probe as a function of probe voltage can be represented by another column matrix I_e:

$$f = \begin{bmatrix} \frac{n_{e1}}{E_1 - E_0} \\ \frac{n_{e2}}{E_2 - E_1} \\ \vdots \\ \frac{n_{eN}}{E_N - E_{N-1}} \end{bmatrix} \tag{3.51}$$

and

$$I_e = \begin{bmatrix} I_{e1} \\ I_{e2} \\ \vdots \\ I_{eM} \end{bmatrix} \tag{3.52}$$

where n_{e1}, n_{e2} … n_{eN} are the previously defined densities of N individual step function that makes up the total EEDF and where I_{e1}, I_{e2}, … I_{eM} are the M measurements of electron current made at M probe voltages. In this case, the elements of f make up the N unknowns that we would like to solve for in order to obtain an EEDF from measured electron current data. These column matrices can be brought together to form a linear system of equations by setting up a system matrix that relates these two column matrices together as shown in eq. 3.3, where K is an M x N matrix with a large condition number $M \geq N$, whose elements are defined by eq. 3.32, and serves as the integral kernel of eq. 3.5:

$$K = \begin{bmatrix} \frac{I_{e1}(E_1 - E_0)}{n_{e1}} & \frac{I_{e1}(E_2 - E_1)}{n_{e2}} & \cdots & \frac{I_{e1}(E_N - E_{N-1})}{n_{eN}} \\ \frac{I_{e2}(E_1 - E_0)}{n_{e1}} & \cdot & & \\ \vdots & & \cdot & \\ \frac{I_{eM}(E_1 - E_0)}{n_{e1}} & \cdot & \cdot & \frac{I_{eM}(E_N - E_{N-1})}{n_{eN}} \end{bmatrix} \tag{3.53}$$

A linear least squares solution of eq. 3.52 is a solution to the problem

$$\min_{f \in C^m} \left\| Kf - I_e \right\|^2 \tag{3.54}$$

where the Euclidian vector norm in C^m is used. Using the notation introduced in other papers we say that the algebraic problems presented by eqs. 3.52 and 3.54 are discrete ill-posed problems [2]. There are many numerical methods for solving ill-posed problems in function spaces, as well as for solving discrete ill-posed problems. These methods are based on so-called regularization methods. The most well known is the Tikhonov approach, which consists of replacing the least squares problem of eq. 3.54 by the problem of a suitably chosen Tikhonov functional. The simplest version of this method has the form

$$\min_{f \in C^m} \|Kf - I_e\|^2 + \alpha^2 \|f\|^2 \qquad (3.55)$$

where $\alpha \in R$ is called the regularization parameter. An important and still current problem is a proper choice of the regularization parameter. There are several possible strategies that depend on additional information concerning the considered problem and its solution. To determine α, Reginska suggests then minimizing the product of the residual and the norm of the regularizer,

$$G(\alpha) = \|I_e - Kf(\alpha)\|^2 \; x \; \|Df(\alpha)\|^2 \qquad (3.56)$$

with respect to α [22]. Reginska actually considers only the case $D=I$, the identity operator. A similar approach to that taken by Holloway et. al. will produce some similar results for the more general case $D \neq I$, but in a somewhat more direct way that does not rely on the singular value decomposition of K[23].

This system of equations can now be solved using a pseudo-inverse matrix solution for f. Additionally, the incorporation of *a-priori* assumptions of the final solution of f (smoothly

rolling, derivative magnitude and polarity constraints, etc.) can also be employed by implementing a regularized solution to the problem:

$$f = \left[K^T K + \alpha D^T D \right]^{-1} K^T I_e \tag{3.57}$$

where D is an *a-priori* conditioning matrix.

3.4.2 Preliminary Results

In this section the ability of the regularized algorithm described above to address the ill-posedness of the EEDF extraction problem is studied and compared to an unregularized algorithm (a Savitzky Golay filter to smooth electron current data). A kernel space of $M=N=600$ where the energy ranges from 0 to 60 eV is used. The regularized solution can be validated by taking a known distribution function f_{test}, calculating model electron current I_{etest} by the operation $I_{etest} = Kf_{test}$, adding statistical random noise of various levels to I_{etest}, and reconstructing the distribution function for comparison to the known input f_{test}.

Several distributions that are typically observed in low temperature plasmas are studied using this methodology. Figure 3.2 highlights this analysis for a Maxwell-Boltzmann distribution with $n_e = 10^{14}\text{cm}^{-3}$ and $T_e = 5\text{eV}$ with a signal-to-noise ratio (*SNR*) of *SNR*=100 and *SNR*=20 added to the calculated current I_{etest}. The noise applied in these cases is White Gaussian Noise. The analysis also is carried out on Druyvesteyn and Bi-Maxwellian distributions as shown in figures 3.3 and 3.4. Figure 3.3 highlights the analysis for a Druyvesteyn for $n_e = 10^{14}\text{cm}^{-3}$ and $T_e = 5\text{eV}$ with both *SNR*=100 and *SNR*=20 added to the calculated current I_{etest}. Figure 3.4 is the analysis for a Bi-Maxwellian for $n_{e1} = 10^{14}\text{cm}^{-3}$ and $n_{e2} = 4*10^{13}\ \text{cm}^{-3}$ $T_{e1} = 5\text{eV}$ and $T_{e2} = 15\text{ eV}$ with both *SNR*=100 and *SNR*=20.

Figures 3.2 a-c. Noise added to calculated electron current and the resulting deviation of EEDF solution from the test structure using optimized regularized solution.

Figure 3.2 a. The straight curve represents original current, while the dashed curve is the current with noise added to it.

Figure 3.2 b. The straight curve represents the original Maxwellian distribution, while the dashed curve represents the Reconstructed Maxwellian with *SNR*=100.

Figure 3.2 c. The straight curve represents the original Maxwellian distribution, while the dotted curve represents the Reconstructed Maxwellian with *SNR*=20

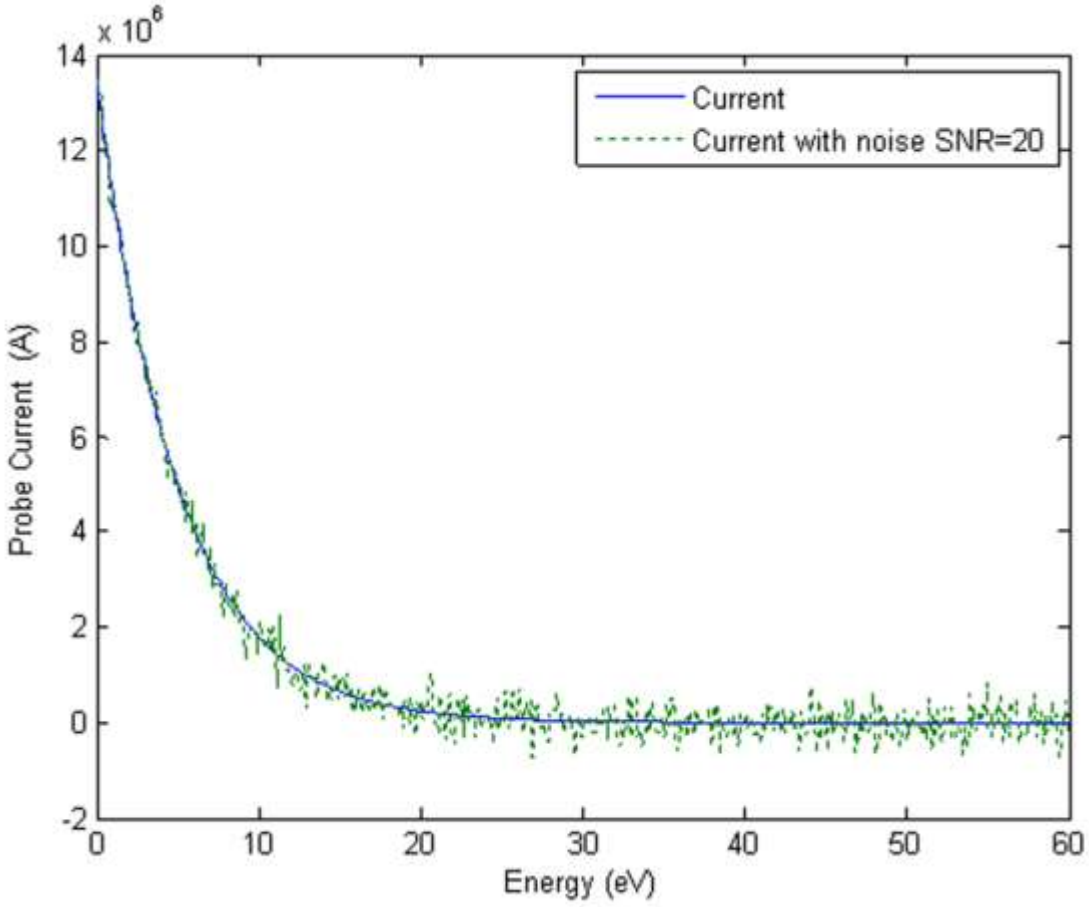
x 10^6
14
12
10
8
6
4
2
0
-2
Probe Current (A)
0
10
20
30
40
50
60
Energy (eV)
Current
Current with noise SNR=20

(a)

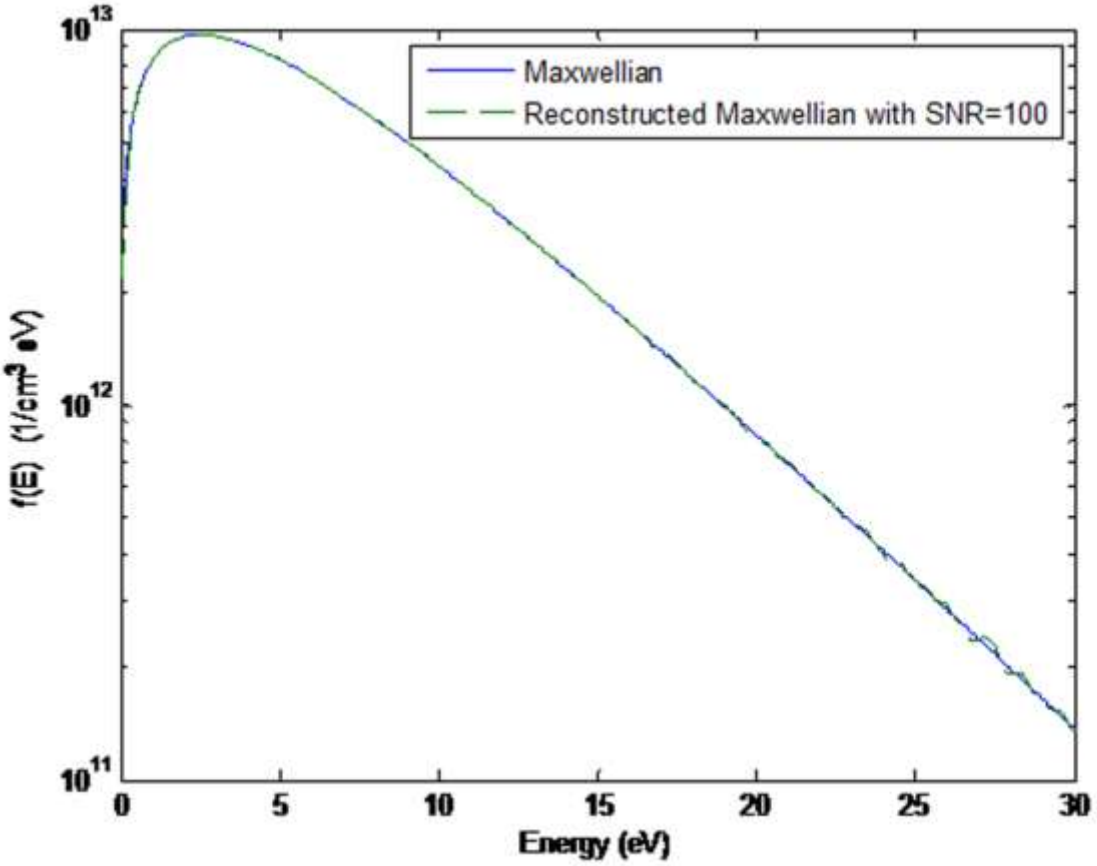
Maxwellian
Reconstructed Maxwellian with SNR=100
f(E) (1/cm3 eV)
Energy (eV)
10^13
10^12
10^11
0
5
10
15
20
25
30

(b)

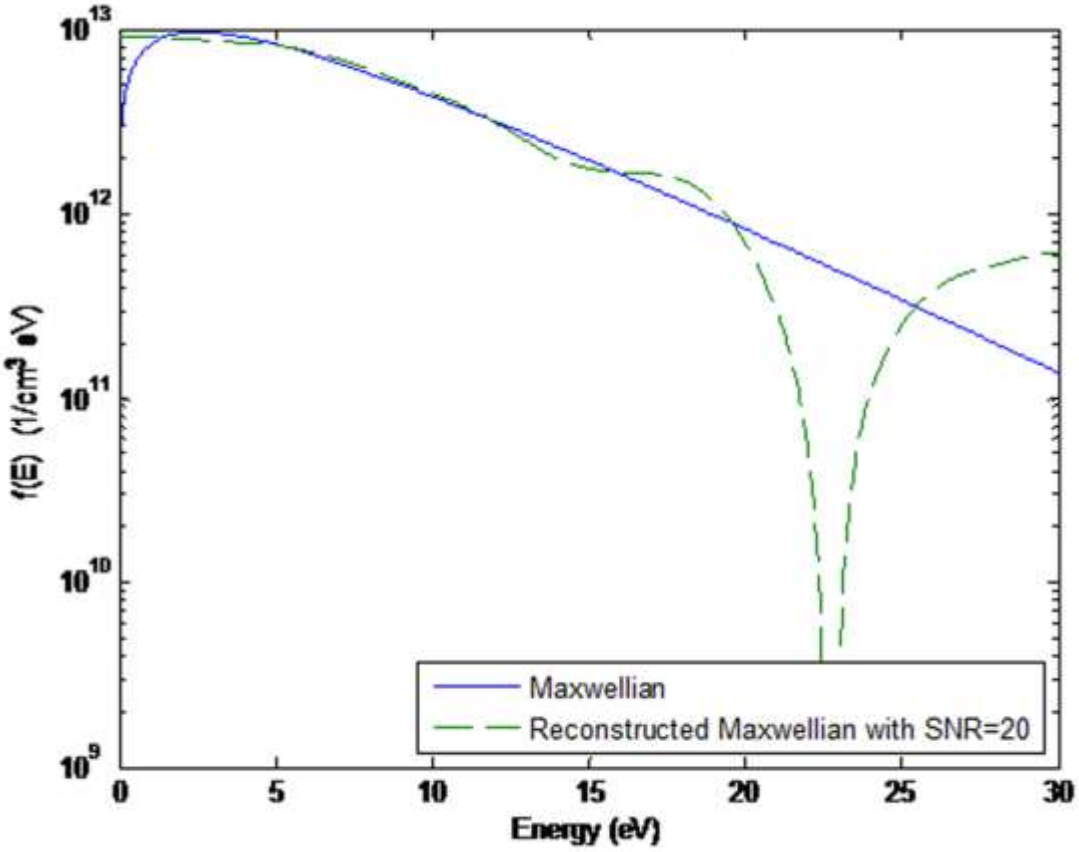
10^13
10^12
10^11
10^10
10^9
f(E) (1/cm^3 • eV)
0
5
10
15
20
25
30
Energy (eV)
Maxwellian
Reconstructed Maxwellian with SNR=20

(c)

Figures 3.3 a-b. The resulting deviation of EEDF solution from the test structure using optimized regularized solution.

Figure 3.3 a. The straight curve represents the original Druyvesteyn distribution, while the dotted curve represents the Reconstructed Druyvesteyn with *SNR*=100.

Figure 3.3 b. The straight curve represents the original Druyvesteyn distribution, while the dashed curve represents the Reconstructed Druyvesteyn with *SNR*=20.

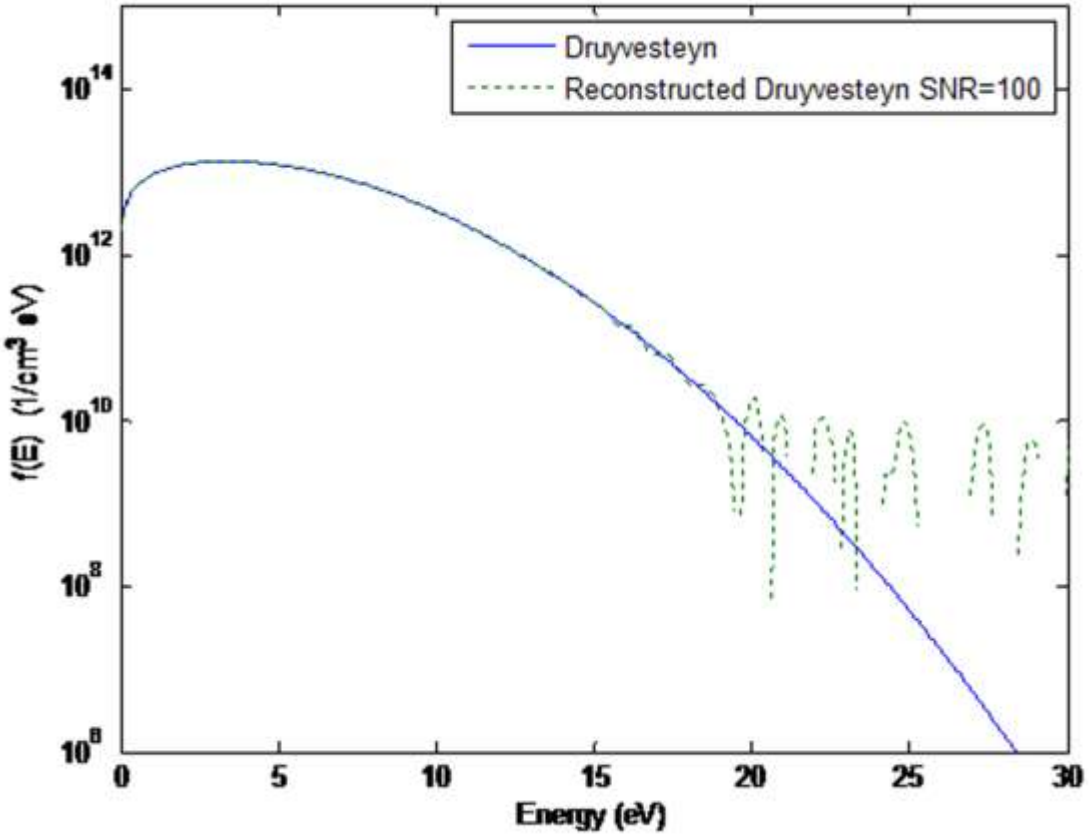
Druyvesteyn
Reconstructed Druyvesteyn SNR=100
f(E) (1/cm³ •V)
10^14
10^12
10^10
10^8
10^6
0
5
10
15
20
25
30
Energy (eV)

(a)

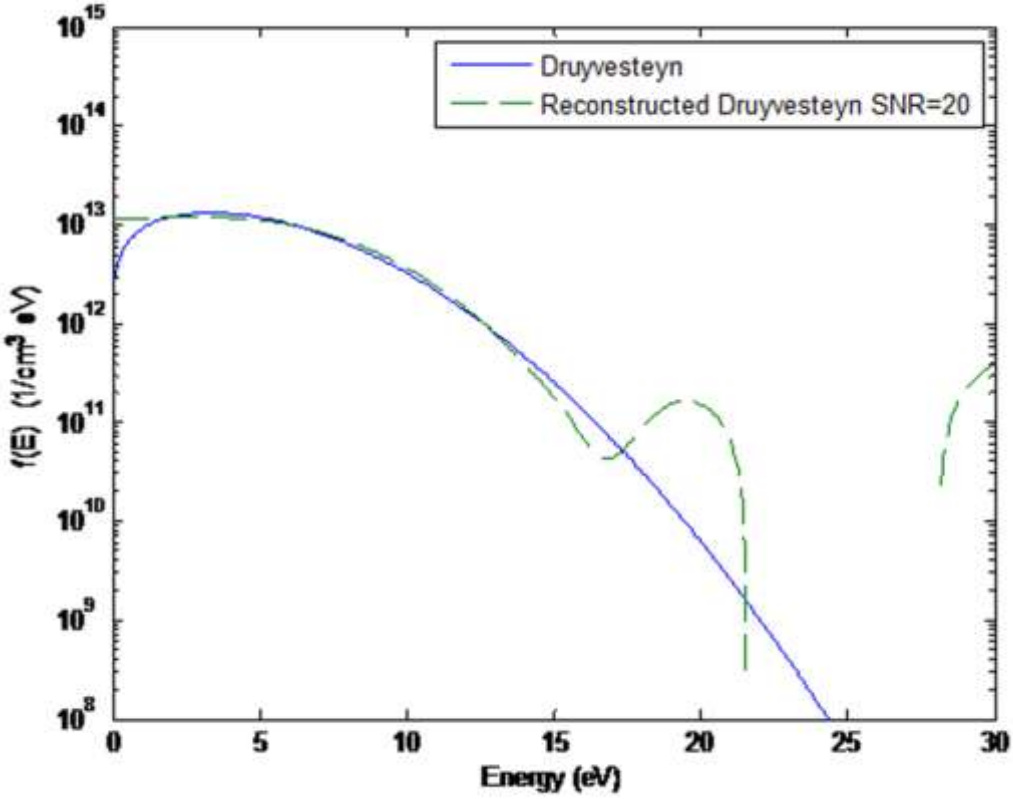
Druyvesteyn
Reconstructed Druyvesteyn SNR=20
f(E) (1/cm³ •V)
Energy (eV)
10^15
10^14
10^13
10^12
10^11
10^10
10^9
10^8
0
5
10
15
20
25
30

(b)

Figures 3.4 a-b. The resulting deviation of EEDF solution from the test structure using optimized regularized solution.

Figure 3.4 a. The straight curve represents the original Bi Maxwellian distribution, while the dotted curve represents the Reconstructed Bi Maxwellian with *SNR*=100.

Figure 3.4 b. The straight curve represents the original Bi Maxwellian distribution, while the dashed curve represents the Reconstructed Bi Maxwellian with *SNR*=20

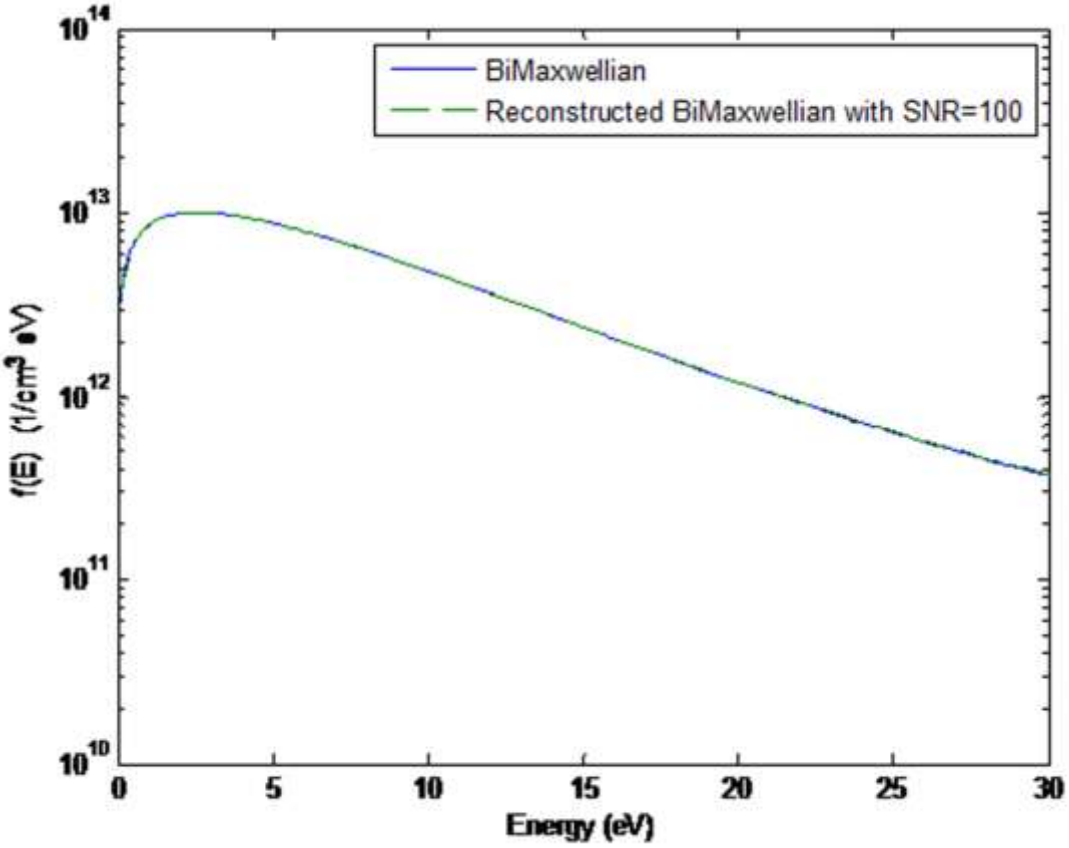
BiMaxwellian
Reconstructed BiMaxwellian with SNR=100
f(E) (1/cm3 •V)
Energy (eV)
10^14
10^13
10^12
10^11
10^10
0
5
10
15
20
25
30

(a)

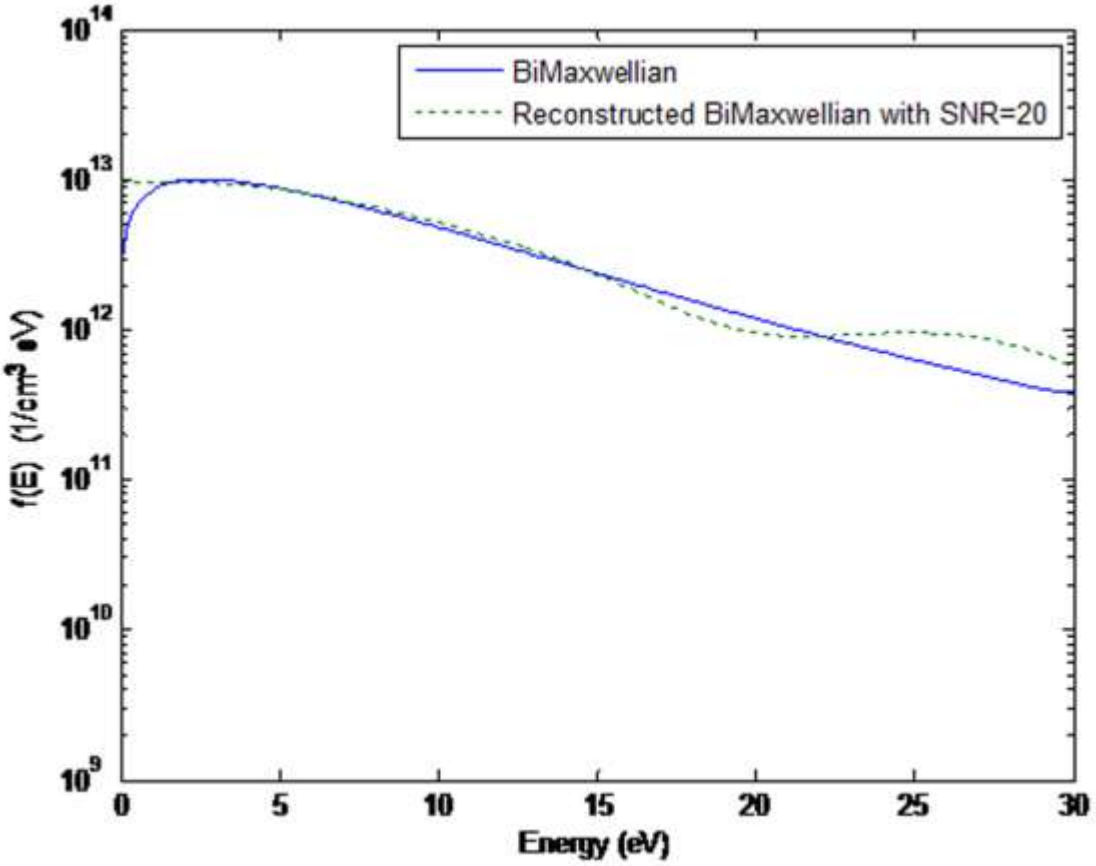
BiMaxwellian
Reconstructed BiMaxwellian with SNR=20
f(E) (1/cm³ • eV)
Energy (eV)
10^14
10^13
10^12
10^11
10^10
10^9
0
5
10
15
20
25
30

(b)

Figure 3.5 offers a comparison of this optimized regularization algorithm to a traditional minimum norm least squares solution of the matrix problem (effectively eq. 3.55 with $\alpha \rightarrow 0$) namely $f(0)=(K^TK)^{-1}K^TI_e$, as well as a comparison to curve fitting techniques as a function of noise level which is unique in all of the cases considered in this paper. We see in this figure that the error in the reconstruction increases rapidly in an unregularized reconstruction, while the regularized reconstruction is much less sensitive to error.

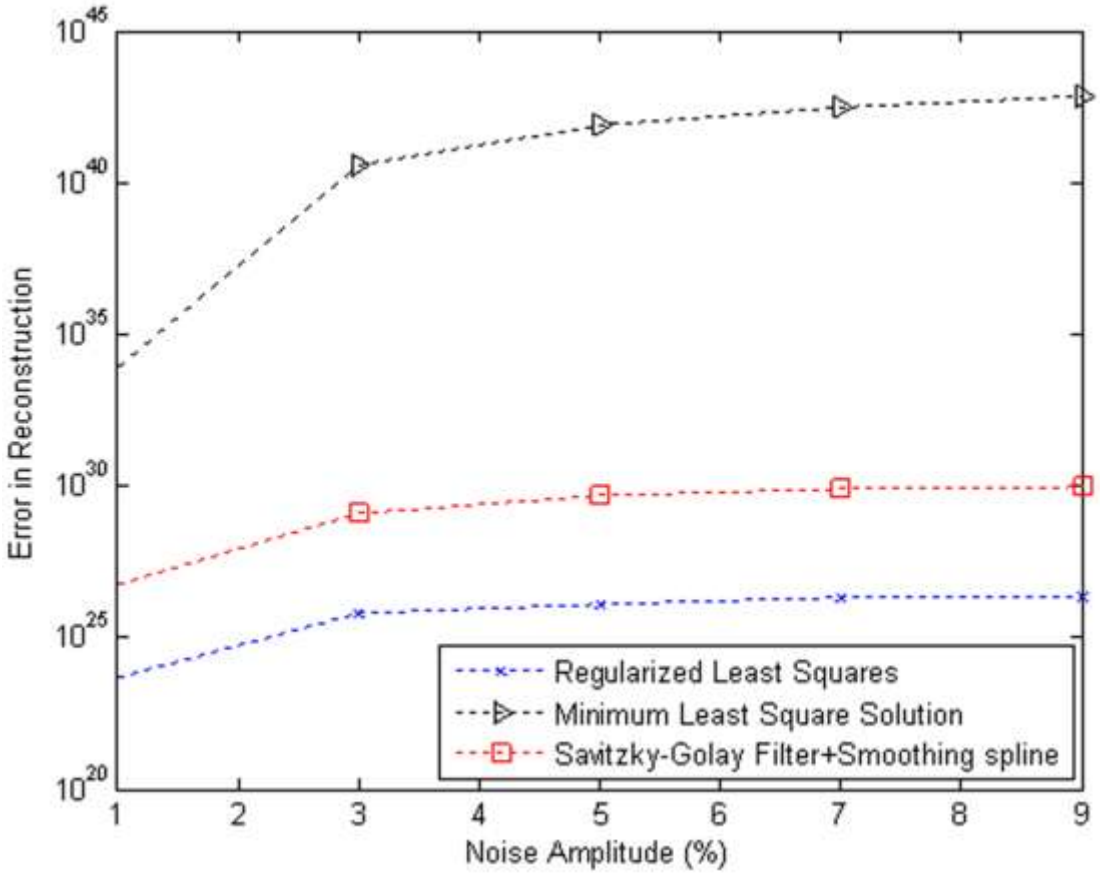

Figure 3.5. The error in reconstruction vs different noise amplitudes for Regularised Least Squares compared to MLSS, and Curve Fitting.

TABLE 3.1
ERROR IN RECONSTRUCTION

Distrbution	SNR	Error(%)
Maxwellian	100	0.0486
Maxwellian	20	0.35
Druyvesteyn	100	0.04514
Druyvesteyn	20	0.64
Bi Maxwellian	100	0.0272
Bi Maxwellian	20	0.14

The large amount of noise present in the unregularized solution is the result of the ill-posed nature of the problem - small errors in the input data I_e result in large errors in the reconstruction *f,* and renders this unregularized solution essentially useless. In contrast, the regularized reconstruction is free of noise and much more accurate as presented in Table 3.1.

From this analysis, several observations can be made with regard to the capability of Tikhonov regularization to reconstruct EEDF's from Langmuir probes given a reasonable amount of noise in the collection of electron current. Firstly, at higher noise levels, the first derivative regularizing constraint fails to capture the steep positive slope on the low energy side of the distribution maximum for all three distributions. The need for a smoothing constraint to capture the higher energy distribution characteristics compete with the steeper slope typically observed at lower energies, resulting in distortion of the reconstructed EEDF in that region. Secondly, at moderately high electron energies, even with modest *SNR*, the algorithm is capable of reproducing the EEDF with a high level of accuracy. As previously alluded to in the introduction, it is these higher energies where inelastic events begin to

influence the EEDF that is of particular interest for several low temperature plasma applications. These competing distribution characteristics pose a challenge for single parameter regularization techniques, and more exotic implementation of Tikonov regularization may need to be employed to accurately capture both of these distribution characteristics simultaneously.

3.4.3 Reconstruction Challenges

Low temperature plasmas exhibit an array of EEDF shapes, ranging from Maxwellian distributions, bi-Maxwellian's, Druyvestians, bump-in-tail, and others. Most of these distributions exhibit similar characteristics: they fall to zero at E = 0, they can typically be broken up into a "bulk electron region" and a "high energy tail" region that both present different insight into the plasma itself (as well as different challenges in reconstruction of the distribution in that region), and they tend to have a relatively smooth shape absent of discontinuities in magnitude or slope.

$$f_e(E) = \frac{2\pi}{(\pi kT)^{3/2}} \sqrt{E} \exp(-\frac{E}{kT}) \tag{3.58}$$

When applying a Tikhonov regularization in order to reconstruct the EEDF a challenge appears where the reconstructed distribution does not start at zero.

$$f_e(\alpha) = \left[K^T K + \alpha D^T D \right]^{-1} K^T I_e \tag{3.59}$$

The reconstructed distribution starts at some value causing a disruption in the peak of the distribution by shifting it a few eV, thus giving inaccurate information about the low energy portion and forcing the disruption to propagate to the high energy tail as well. This result could be attributed to the fact that the singular values of the kernel *K* are small (in the range of e-15). Assuming that the singular value decomposition of *K* is

$$K = U\Sigma V^T = \sum_{i=1}^{n} u_i \sigma_i v_i^T \tag{3.60}$$

where *U* is an *M*-by-*M* unitary matrix over *K*, and V^T denotes the conjugate transpose of *V*, an *N*-by-*N* unitary matrix over *K*, and v_i are the column vectors of *V*, which are called right singular vectors, and u_i are the column vectors of *U*, which are called the left singular vectors (it should be noted that there are other conflicting notational conventions)[24,25]. By applying these singular values to eq. 3.59 and assuming for simplicity that D=I, we obtain the following

$$f_e(\alpha) = \frac{\sigma_i (u_i^T I_e)}{\sigma_i^2 + \alpha} v_i \tag{3.61}$$

At the beginning where the distribution should start from zero the regularization parameter is small compared to the singular values ($\alpha << \sigma$) causing eq. 3.61 to become

$$f_e(\alpha) = \frac{(u_i^T I_e)}{\sigma_i} v_i \tag{3.62}$$

Thus the current is divided by a small value causing it to never start at zero but some higher value as shown in figure 3.6.

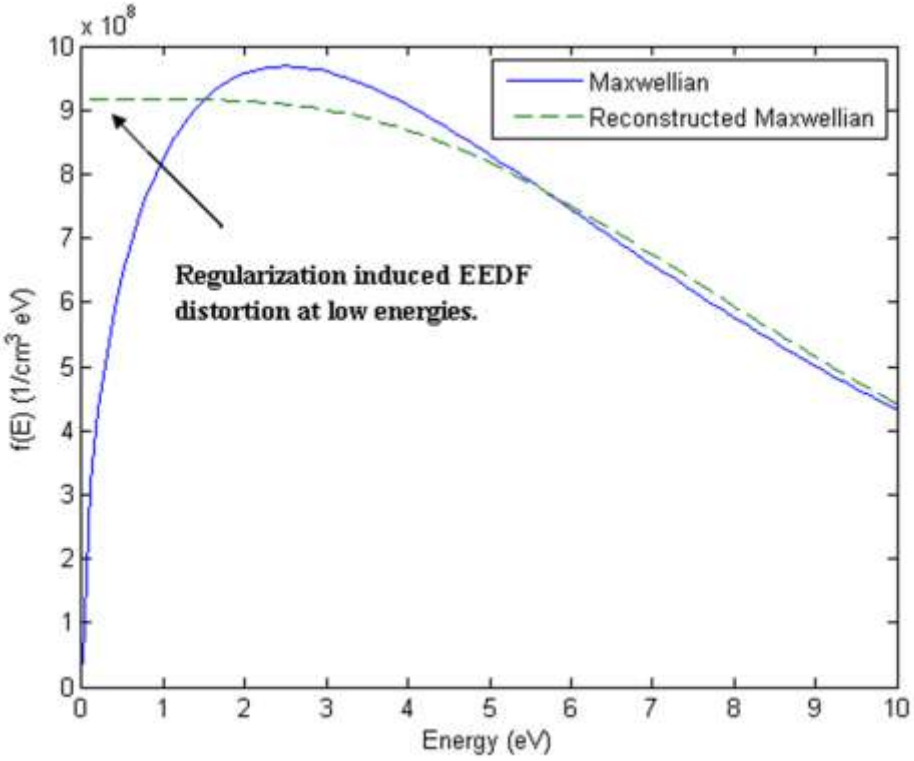

Figure 3.6. The resulting deviation of reconstructed EEDF by beginning at a high value not at zero.

Optimization of the regularization parameter α also presents a significant challenge in accurate reconstruction of EEDF's. Over regularization allows the regularizing constraint

D to over-condition the solution, and tends to capture the high energy portion of the distribution at the expense of the low energy portion. Under regularization does not fully address the noise amplification generated by the ill-posed nature of the integral problem. This tends to produce solutions where the low energy portion is captured at the expense of the high energy portion, where the noise effects present as strong oscillations in the final solution. In order to solve the problem of over and under regularization a technique for optimizing the regularization parameter is required. One of the most famous optimizing methods is the L-Curve method [26]. The L-Curve is simply the plot of the semi norm $||f_{reg}||_2$ – of the regularized solution versus $||K f_{reg} - I_e ||_2$ which is the residual norm. From eq. 3.1 writing the left hand side as

$$I_e = I_e^{exact} + e \tag{3.63}$$

where *e* represents the perturbation added to the original current. Rewriting eq. 3.3 to include eq. 3.63 we obtain

$$f_{e(reg)} = K\, I_e^{exact} + K\, e \tag{3.64}$$

In a general case the error is given by (assuming $D \neq I$)

$$f_e^{exact} - f_{e(reg)} = (f_e^{exact} - K\, I_e^{exact}) - K\ \mathrm{e} \tag{3.65}$$

$$f_e^{exact} - f_{e(reg)} = \sum_{i=1}^{m}(1-f_i)\frac{u_i^T I_e^{exact}}{\sigma_i} f_{e(i)} \\ -(\sum_{i=1}^{m} f_i \frac{u_i^T e}{\sigma_i} f_{e(i)} + \sum_{i=1}^{l} u_i^T e\, f_{e(i)}) \quad (3.66)$$

where f_i represents the filter factor[26]. The error is made up of two parts. The first part is the perturbation error $K\,e$ that is mainly due to the error e. The second part is the regularization error $f_e^{exact} - K\,I_e^{exact}$ that is mainly due to the regularization of I_e^{exact} that is free of error.

In the case of under-regularization, the filter factors f_i are 1 and the error is dominated by the perturbation error $K\,e$. This case corresponds to a point on the L-Curve on top of the middle corner (See Figure 3.6 and3.7). In the case of over regularization a large amount of regularization is introduced so the filter factors are so small $f_i << 1$, that the error is dominated by the regularization error $f_e^{exact} - K\,I_e^{exact}$. This case corresponds to a point on the right most part of the L-Curve to the right of the corner as shown in figure 3.8. As discussed above, the challenges in reconstruction have a serious impact on EEDF reconstruction. In order to address these challenges a number of alternate solutions are evaluated.

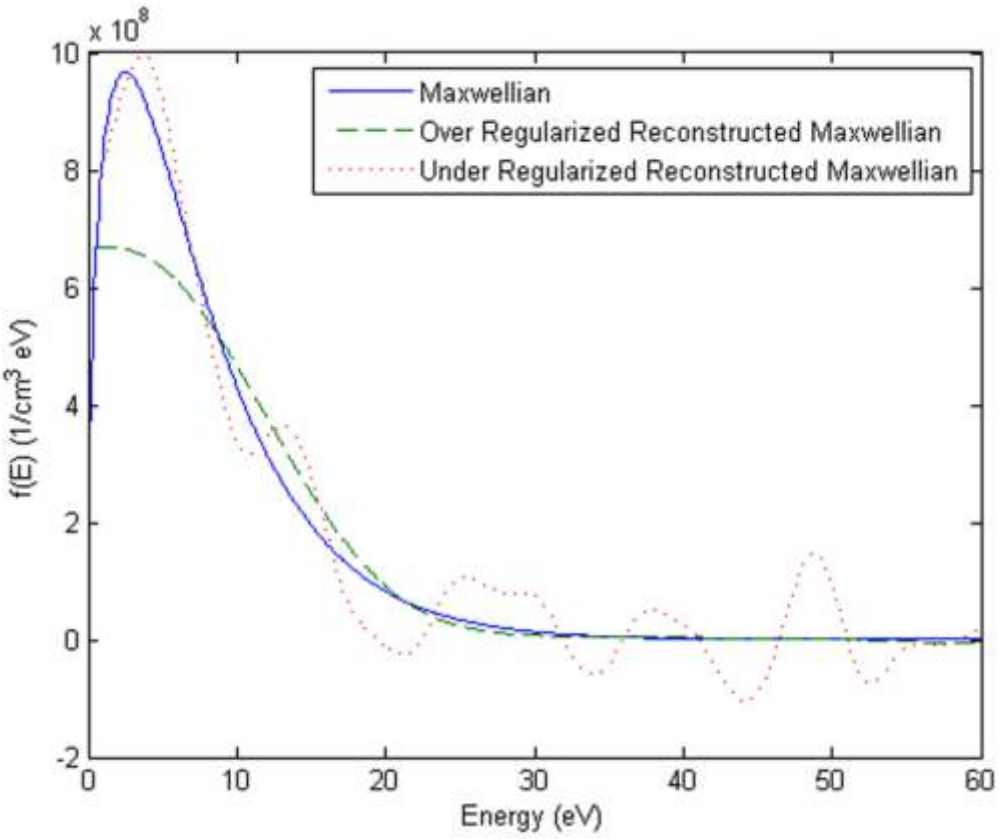

Figure 3.7. A comparison between both under regularization (dotted curve) and over regularization (dashed curve).

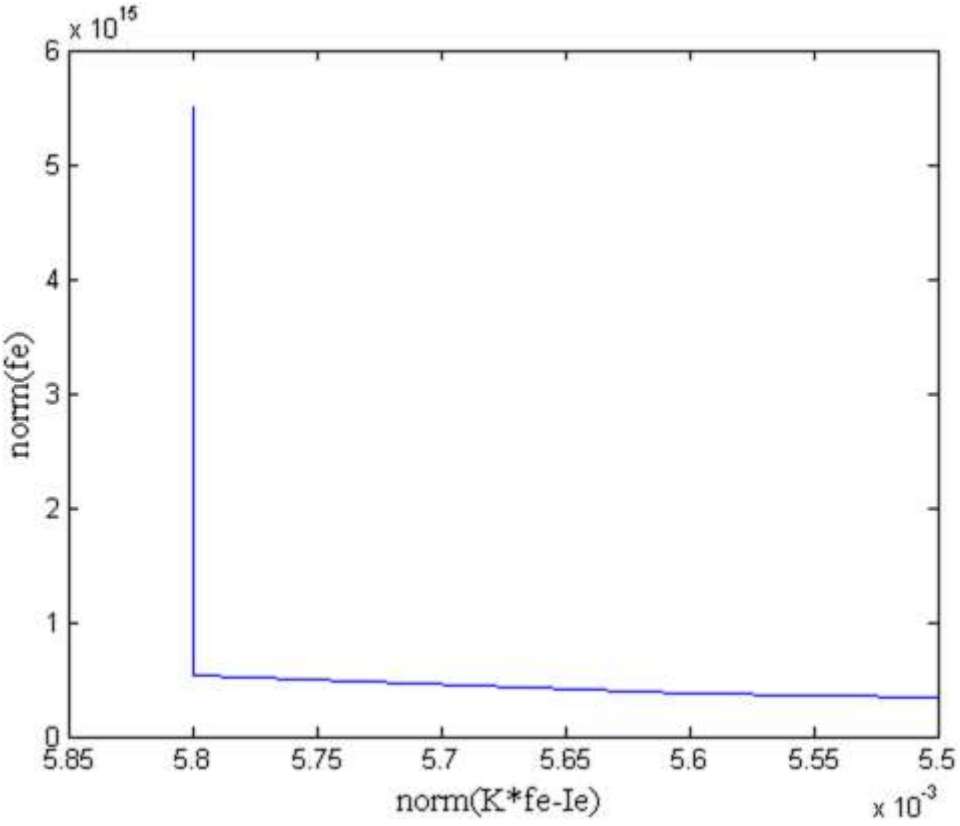

Figure 3.8. The seminorm of the regularized solutions versus the residual norms.

3.4.4 Advanced Algorithms

Modification of the D matrix

1. The first of these solutions is to force the first column in the kernel K to zero, thus forcing $f_e(0)=0$. Although the first column was forced to zero but due to the fact that the kernel is being added to a regularization parameter we ended up with the situation where the distribution starts at some value not zero.
2. The second solution that was evaluated was to look at the apriori conditioning matrix D, and evaluate alternative conditioning matrices. Reginska actually considers only the case D=I, the identity operator[22]. A similar approach to that taken by Holloway et. al. produces some similar results for the more general case $D \neq I$ [27]. Normally the first derivative constraint was considered for D and the results obtained included both the challenges discussed above. Taking higher derivative constraints such as the second or even the third made no difference in the results except the fact that the regularization parameter α was increasing in value(due simply to the fact that the at higher derivative constraints the product D^TD becomes smaller causing the regularization parameter to increase so that the term αD^TD could have an effect on the K^TK term). This observed invariance to higher order derivative constraints is due to the fact that most of the distributions being reconstructed have ”near exponential” characteristics. Because of this, increasing the derivative constraints to higher values will have no apparent effect (particularly in the high energy tail where the exponential portion of distributions tend to dominate.

Truncated Singular Value Decomposition

Another method for solving discrete ill-posed problems is to improve the conditioning number of the system matrix through modifications such as truncated singular value decomposition of the *K* matrix. To apply a truncated SVD solution is to assign a numerical rank *k* to *K.* Setting to zero all singular values σ_i , $i > k$, the corresponding solution can be expanded in the form

$$x = \sum_{i=1}^{k} \frac{c_i}{\sigma_i} v_i, \quad c = U^T I_e \tag{3.67}$$

The TSVD solution solves the related least squares problem

$$\min_x \left\| K_k f_e - I_e \right\|_2, \qquad K_k = \sum_{i=1}^{k} u_i \sigma_i v_i^T \tag{3.68}$$

where K_k is the best rank *k* approximation of *K*[2]. This numerical method gives a better approximation than ordinary least square solution.

Sharp Filter Regularization

Another technique considered was modifying Tikhonov's method to achieve a sharper filter factor [26,28]. This method results in solving the following system of equations

$$f_e(\alpha) = (K^T K + \alpha^2 I + \alpha^2 (K^T K + \alpha^2 I)^{-1})^{-1} K^T I_e \tag{3.69}$$

Where the corresponding filter factors are

$$f_i = \frac{\sigma_i^2}{\sigma_i^2 + \alpha^2 + \dfrac{\alpha^2}{\sigma_i^2 + \alpha^2}} \tag{3.70}$$

Where f_i represents the filter of the modified Tikhonov, σ_i is the singular values of the K, I is identity matrix, and α is the regularization parameter. We have the values

$$f_i \approx \begin{cases} \dfrac{\sigma_i^2}{(\alpha^2+1)} & \sigma_i < \alpha \\ \dfrac{\sigma_i^4}{\alpha^2} & \alpha < \sigma_i < \alpha^{1/2} \quad \text{for } \alpha \le 1 \\ 1 & \alpha^{1/2} < \sigma_i \end{cases} \tag{3.71}$$

$$f_i \approx \begin{cases} \dfrac{\sigma_i^2}{(\alpha^2+1)} & \sigma_i < \alpha \quad \text{for } \alpha \ge 1 \\ 1 & \alpha < \sigma_i \end{cases} \tag{3.72}$$

As seen in the case where $\alpha \le \sigma_i \le \alpha^{1/2}$, a sharper cut-off for singular values is achieved [26].

Hybrid Tikhonov Filter / SVD Method

Finally a hybrid method is proposed in which the filter of the Tikhonov is extracted and is implemented to the singular value decomposition (SVD), where the SVD of K is

$$K = U\ diag(\sigma_i)\ V^T \tag{3.73}$$

where U is an M-by-M unitary matrix over K, and V^T denotes the conjugate transpose of V, an N-by-N unitary matrix over K.

By extracting Tikhonov filter and adding it to the SVD of the K matrix we obtain the following result,

$$K = U\ diag(\frac{\sigma_i}{\sigma_i^2 + \alpha})\ V^T \tag{3.74}$$

By taking this modified K matrix and returning to eq. 3.1 f can be obtained using an ordinary least square solution with better accuracy. As for over and under regularization, this challenge is solved by using an L-Curve plot where the optimum position where accurate results are obtained is the regularization parameter that corresponds to the corner on the L-Curve. This corner analysis is typically acknowledged as the optimal compromise between the unregularized LLS solution and a-priori assumptions invoked by α and D. [24,26]

Tikhonov Regularization EEPF

The first step is the formulation of the kernel K in eq. 3.3 for the EEDF integral problem. The methodology starts with the derivation of the electron current collected by a probe as a function of applied potential referenced to the plasma potential using eq. 3.2 and a step function distribution given by:

$$f(E)=\begin{cases} 0 & if \quad E<E_L \\ \dfrac{n_e}{E_H-E_L}\dfrac{1}{\sqrt{E_H}} & if \quad E_L\le E\le E_H \\ 0 & if \quad E>E_H \end{cases} \tag{3.75}$$

where n_e is the density of electrons (assumed to be constant) between a low energy limit E_L and a high energy limit E_H. By applying the same derivation in [3] we obtain the following collective electron energy distribution function represented by

$$f(E)=\sum_{i=1}^{N}\begin{cases} 0 & if \quad E<E_{Li} \\ \dfrac{n_{ei}}{E_{Hi}-E_{Li}}\dfrac{1}{\sqrt{E_{Hi}}} & if \quad E_{Li}\le E\le E_{Hi} \\ 0 & if \quad E>E_{Hi} \end{cases} \tag{3.76}$$

where n_{ei}, E_{Hi}, and E_{Li} represent the magnitude, high energy limit, and low energy limit of each individual step function used to approximate the final distribution, and the total electron current can be represented by a similar summation over all step functions:

$$I_e(E)=\sum_{i=1}^{N}\begin{cases} \dfrac{n_{e\,i}A_p e}{2\left(E_{H\,i}-E_{L\,i}\right)}\sqrt{\dfrac{2}{m_e}}\left[\left(\dfrac{\sqrt{E_{L\,i}}}{\sqrt{E_{H\,i}}}-1\right)E+\dfrac{E_{H\,i}-\sqrt{E_{L\,i}^{\,3}/E_{H\,i}}}{3}\right] & if \quad E<E_{L\,i} \\ \dfrac{n_{e\,i}A_p e}{\left(E_{H\,i}-E_{L\,i}\right)}\sqrt{\dfrac{2}{m_e}}\left(\dfrac{\sqrt{E^3}}{3*\sqrt{E_{H\,i}}}-\dfrac{E}{2}+\dfrac{E_{H\,i}}{6}\right) & if \quad E_{L\,i}\le E\le E_{H\,i} \\ 0 & if \quad E>E_{H\,i} \end{cases} \tag{3.77}$$

Now that the integral kernel K has been obtained for a step function, by applying the values of Kernel K and current I_e to eq. 3.57 we obtain the electron energy probability function through Tikhonov regularization.

3.4.5 Comparison Between Advanced Algorithm Methods

In this section the ability of the hybrid TSVD regularized algorithm described above to address the challenges of the EEDF extraction problem by Tikhonov method is studied. A kernel space of $M=N=600$ where the energy ranges from 0 to 60 eV is used. The regularized solution can be validated by taking a known distribution function f_{test}, calculating model electron current I_{etest} by the operation $I_{etest} = Kf_{test}$, adding White Gaussian Noise of various levels to I_{etest}, and reconstructing the distribution function for comparison to the known input f_{test}.

The figures below highlight this analysis for a Maxwell-Boltzmann distribution with $n_e = 10^{14}\text{cm}^{-3}$ and $T_e = 5\text{eV}$ with a signal-to-noise ratio (SNR) of $SNR=100$ added to the calculated current I_{etest}. As appears in figure 3.9 when TSVD was applied to the problem it was observed that we are able to overcome one of the debilitating challenges which is now it is possible to start at zero but at the expense of the high energy tail and a shifted peak.

In figure 3.10 the modified Tikhonov method with sharper filter is applied. The distribution starts at zero and a portion of the high energy tail but on the expense of a shifted peak energy of approximately 20%.

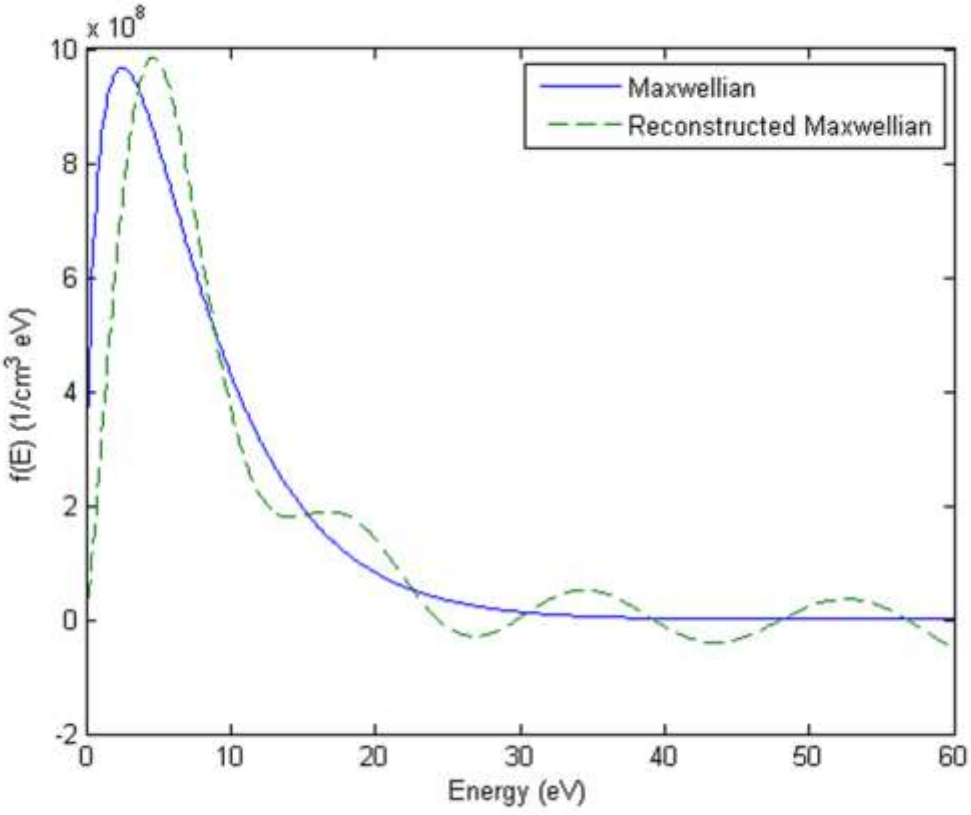

Figure 3.9. The application of TSVD. The straight curve represents the original Maxwellian distribution, while the dashed curve represents the Reconstructed Maxwellian with *SNR*=100.

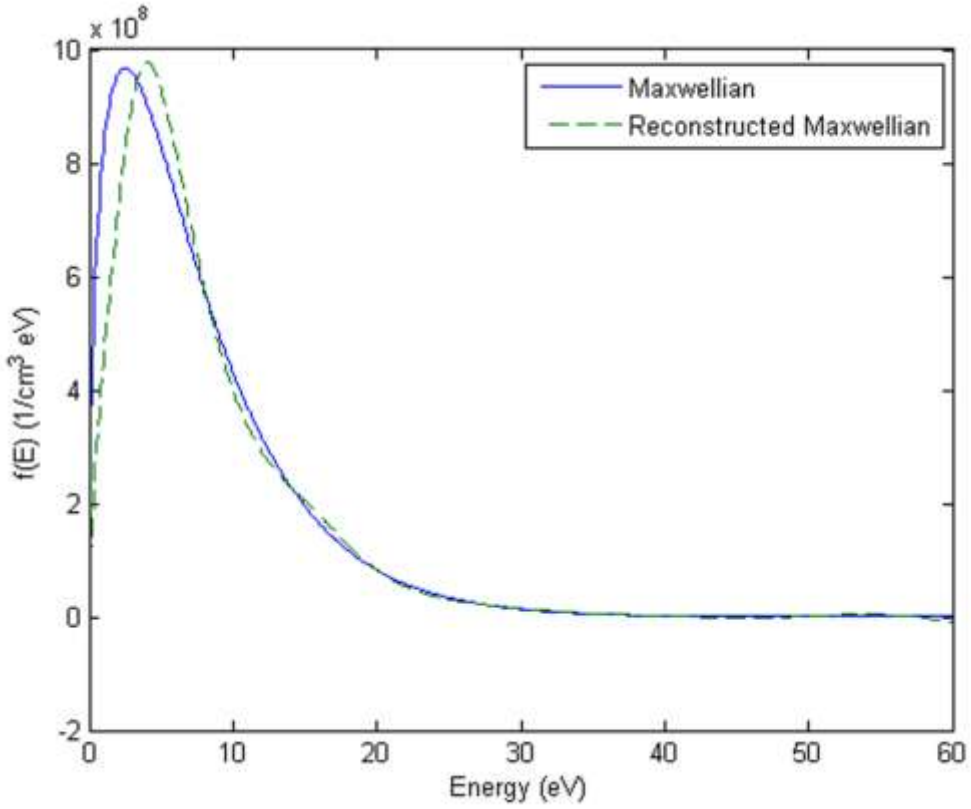

Figure 3.10. The application of a modified sharpening filter.The straight curve represents the original Maxwellian distribution, while the dashed curve represents the Reconstructed Maxwellian with *SNR*=100.

As shown in figure 3.11 it can be seen that by applying the hybrid method where the Tikhonov filter is extracted and being added to the SVD good results are achieved. Finally in figure 3.12 by comparing the results obtained by the hybrid method and the EEPF by Tikhonov method, it is concluded that at SNR values ranging from 100 to 50 both methods are successful in extracting the EEDF while as the SNR values extend from 50 to 10, EEPF by Tikhonov method has shown an advantage over the hybrid method.

Figures 3.11 a-b. The application of the Hybrid method.

Figure 3.11 a. The straight curve represents the original Maxwellian distribution, while the dashed curve represents the Reconstructed Maxwellian with *SNR*=100.(normal plot).

Figure 3.11 b. The straight curve represents the original Maxwellian distribution, while the dashed curve represents the Reconstructed Maxwellian with *SNR*=100.(semilog plot).

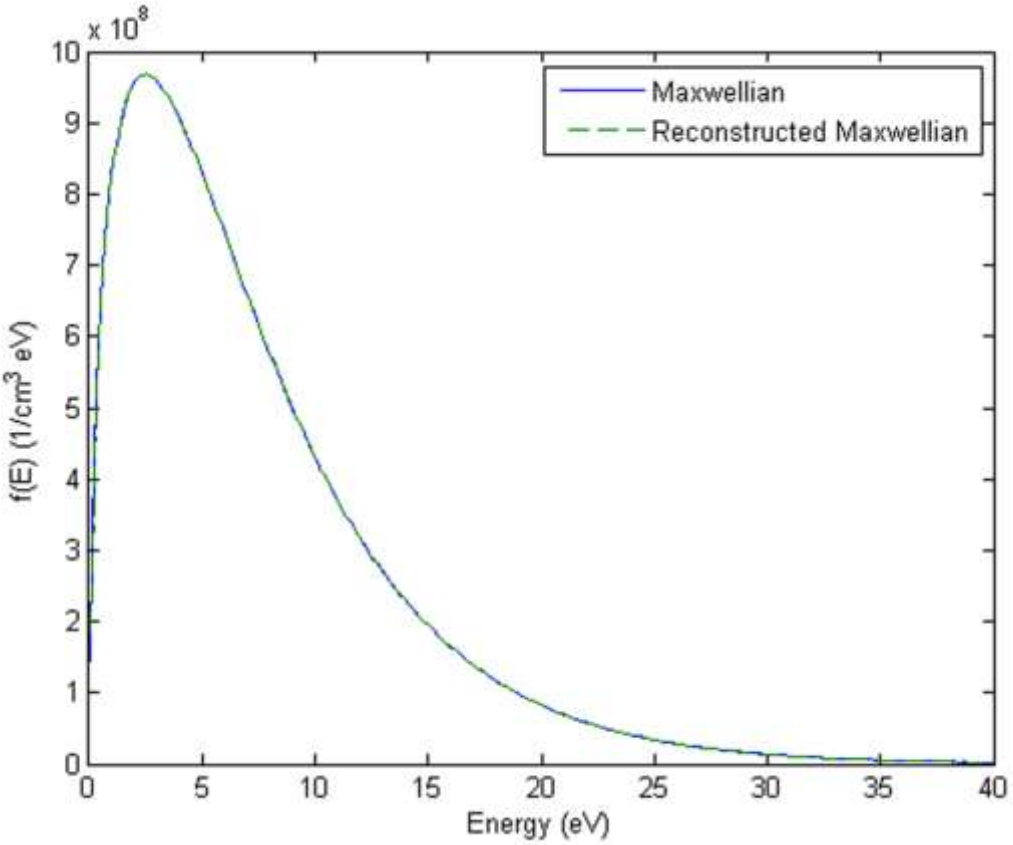
x 10^8
10
9
8
7
6
5
4
3
2
1
0
f(E) (1/cm^3 eV)
0
5
10
15
20
25
30
35
40
Energy (eV)
Maxwellian
Reconstructed Maxwellian

(a)

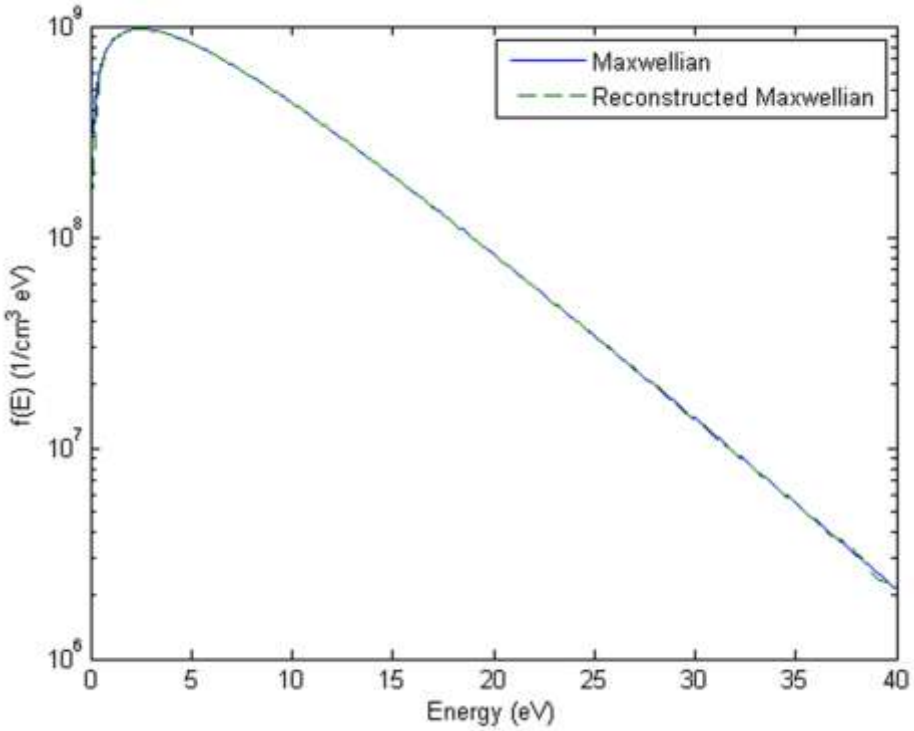
Maxwellian
Reconstructed Maxwellian
f(E) (1/cm3 eV)
Energy (eV)
10^9
10^8
10^7
10^6
0
5
10
15
20
25
30
35
40

(b)

Figures 3.12 a-d. Comparison between Hybrid method and EEPF Tikhonov method for different SNR values.

Figure 3.12 a. SNR=100.

Figure 3.12 b. SNR=50.

Figure 3.12 c. SNR=20.

Figure 3.12 d. SNR=10.

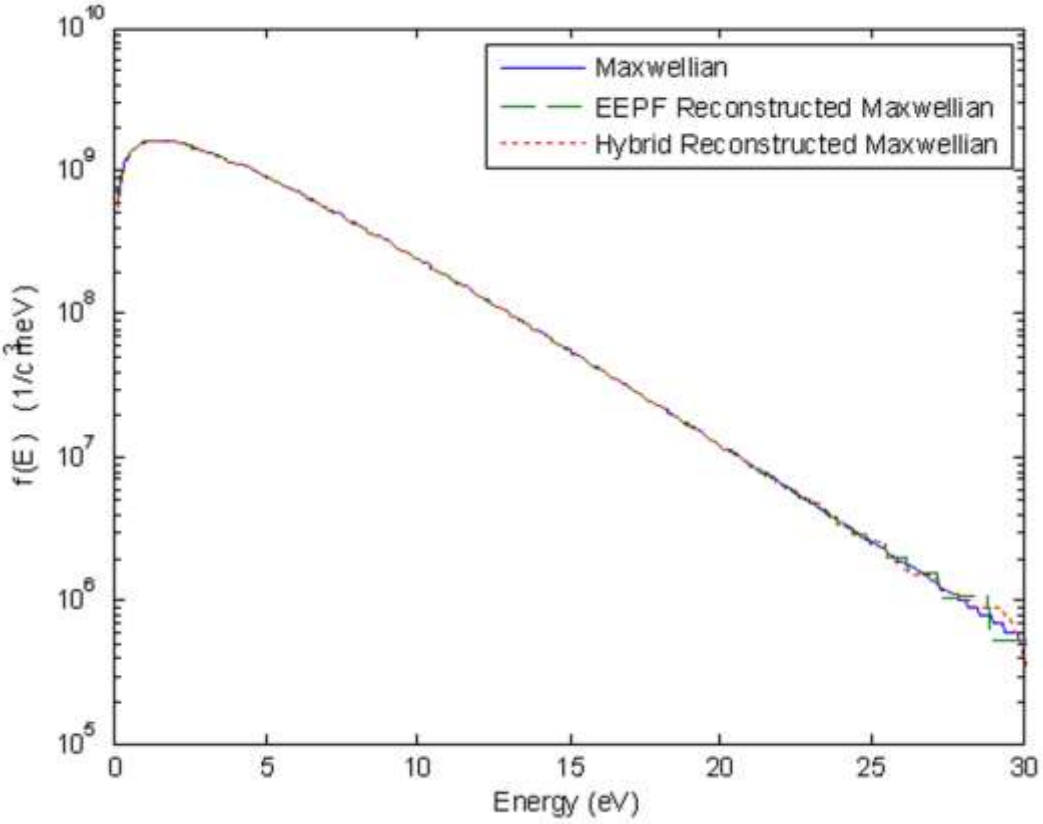
Maxwellian
EEPF Reconstructed Maxwellian
Hybrid Reconstructed Maxwellian
f(E) (1/cm³eV)
Energy (eV)
10^10
10^9
10^8
10^7
10^6
10^5
0
5
10
15
20
25
30

(a)

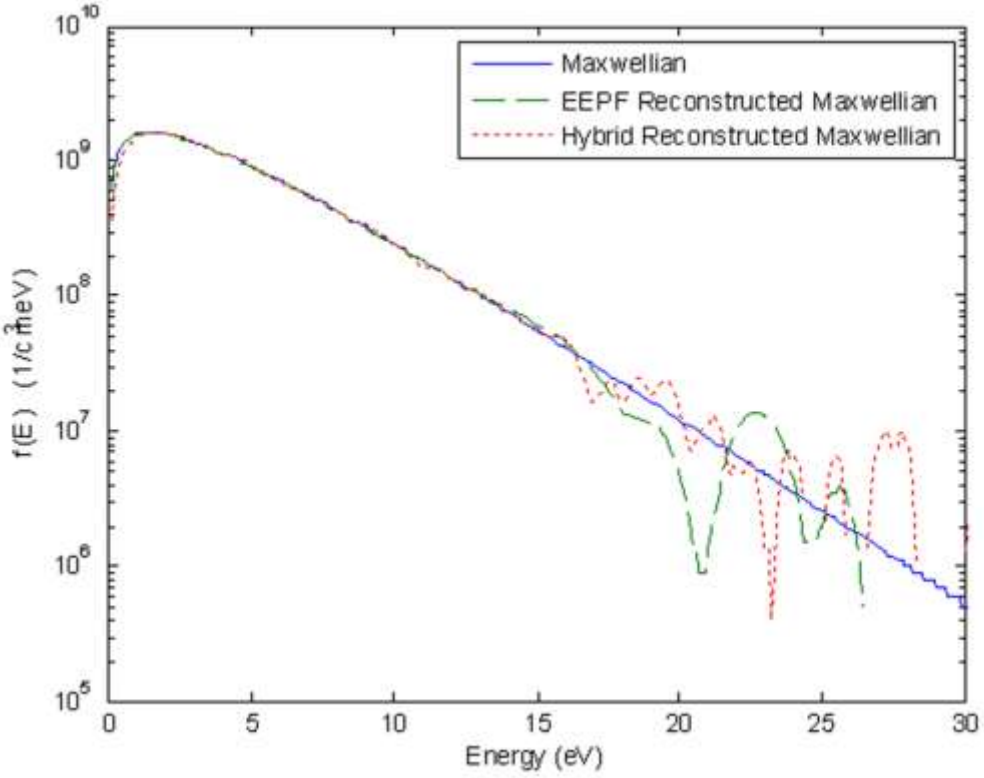
Maxwellian
EEPF Reconstructed Maxwellian
Hybrid Reconstructed Maxwellian
f(E) (1/cm³eV)
Energy (eV)
10^10
10^9
10^8
10^7
10^6
10^5
0
5
10
15
20
25
30

(b)

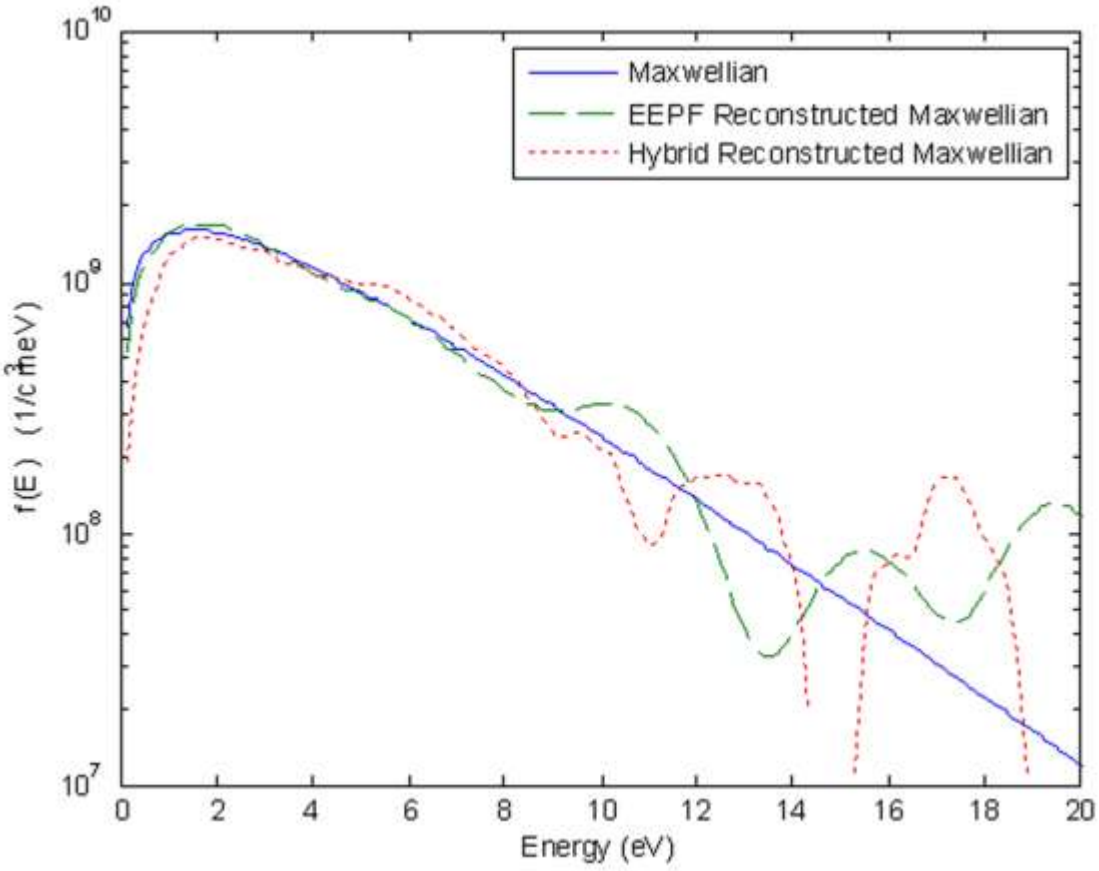
Maxwellian
EEPF Reconstructed Maxwellian
Hybrid Reconstructed Maxwellian
f(E) (1/cm³eV)
Energy (eV)
10^10
10^9
10^8
10^7
0
2
4
6
8
10
12
14
16
18
20

(c)

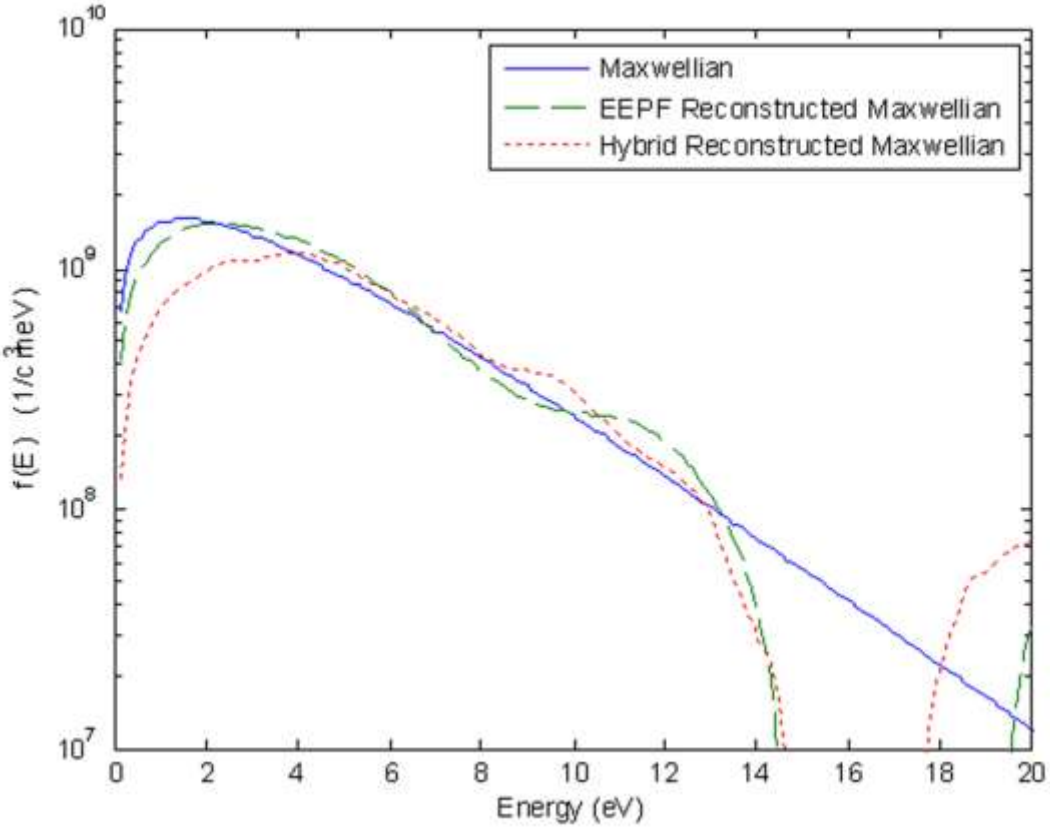
Maxwellian
EEPF Reconstructed Maxwellian
Hybrid Reconstructed Maxwellian
f(E) (1/cm³eV)
Energy (eV)
10^10
10^9
10^8
10^7
0
2
4
6
8
10
12
14
16
18
20

(d)

3.5. Limitations of Regularization Methods

Other methods of representing the distribution of energies for electrons are typically used. These include Electron Energy Probability Functions (EEPF) and Electron Velocity Probability Functions (EVPF). EEPF's normalize the EEDF to $\sqrt{E}$ in order to provide a straight forward linear analysis for Maxwellian distributions.

EVPF's provide the velocity distribution for the electrons, and have been evaluated as an alternate means of obtaining distribution functions by other groups.[29] Although these representations serve as different means to represent the same collective distribution of electrons, each has it's own unique integral relationship between electron current and distribution function as well as it's own unique challenges in accurate extraction of the distribution function in the variable of interest. Assuming an isotropic distribution of electrons in proximity to the biased probe, the integral relation for the EVPF has a similar integral relationship to electron current as the EEDF:

$$I_e(V_p) = 2A_p e \int_{\sqrt{\frac{2eV_p}{m_e}}}^{\infty} f(v) \sqrt{1 + \frac{2eV_p}{mv^2}} v dv \qquad (3.78)$$

albeit with a different integral kernel *k*. This change in *k* presents a very different integral problem than the EEDF problem, and presents challenges that cannot be solved using similar reconstruction methodologies. When talking about electron velocity distribution function the numerical methods mentioned above as well as Tikhonov regularization cease to be useful in the sense that the ill conditioned matrix *k* can not be transformed into a well conditioned matrix without sacrificing the majority of singular eigen values through elimination. This

results in a well conditioned matrix which lacks enough singular eigen values to produce reliable results, particularly in the sensitive tail portion of the distribution. This is due to the fact that the modified kernel *k* that the EVDF integral in eq. 3.78 presents results in a rank-deficient system matrix when the problem is discretized. Rank-deficient problems are characterized by the matrix *k* having a cluster of small singular values, and there is a well-determined gap between large and smaller singular values. Figure 3.13 compares the singular value matrix for both ill posed (EEDF formulation) and rank deficient (EVDF) kernels[30]. Note the rapid drop in the EVDF singular values as a function of index compared to the EEDF formulation. These characteristics present significant challenges in reconstruction that cannot be accounted for in Regularized solutions.[31] To illustrate the impact of this modified kernel, a side by side comparison of EEDF and EVDF reconstructions using the integral formulations of eq. 3.1 and 3.78 for a typical electron distribution can be made, highlighting the challenges of introducing rank-deficient matrices into this integral problem.[31,32]

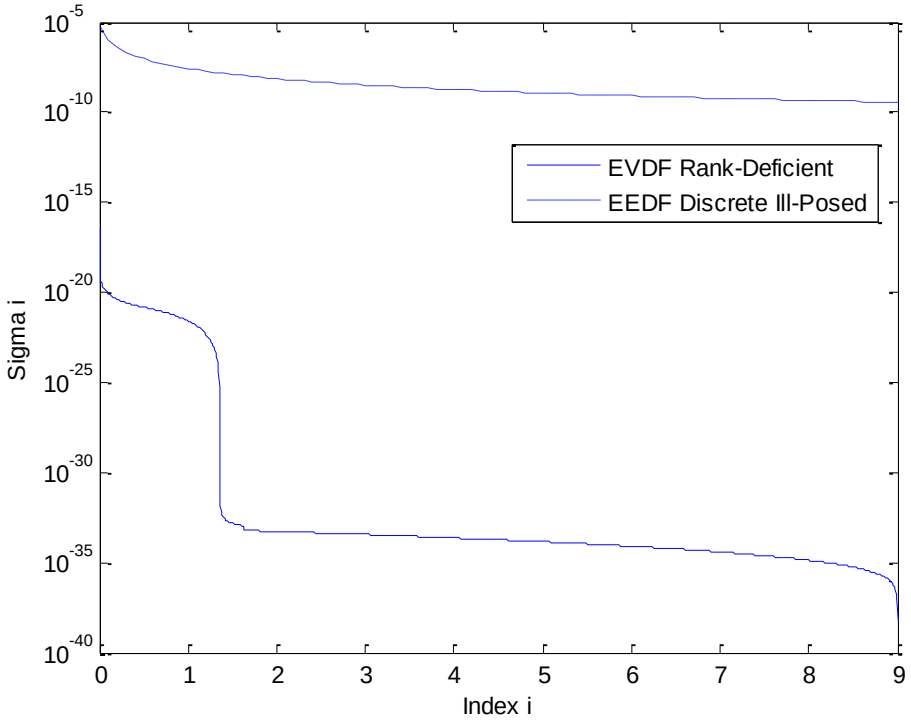

Figure 3.13. The distribution of singular values sigma i(σ_i) of K for both the EEDF and the EVDF.

To illustrate the discussion above, the EEDF and EVPF of comparable distributions are compared using identical I_e matrices. The details of the EEDF reconstruction are provided in previous works [3,30]. The descretization of the EVPF integral follows a similar methodology outlined here. Assuming a planar probe geometry, the number density of electrons with velocity between v and $v+dv$ in the x direction (assuming the planar probe is oriented perpendicular to the x-axis) is

$$dn = f(v)dv \tag{3.79}$$

Where the number density is related to the electron current through eq. 3.79

$$dI = evA_p dn \tag{3.80}$$

By applying a step function distribution given by:

$$f(v) = \begin{cases} 0 & if \quad v < v_L \\ \dfrac{n_e}{v_H - v_L} & if \quad v_L \le v \le v_H \\ 0 & if \quad v > v_H \end{cases} \tag{3.81}$$

where n_e is the density of electrons (assumed to be constant) between a low velocity limit v_L and a high velocity limit v_H. By applying the same derivation in [3] we obtain the following collective electron energy distribution function represented by

$$f(v) = \sum_{i=1}^{N} \begin{cases} 0 & if \quad v < v_{Li} \\ \dfrac{n_{ei}}{v_{Hi} - v_{Li}} & if \quad v_{Li} \le v \le v_{Hi} \\ 0 & if \quad v > v_{Hi} \end{cases} \tag{3.82}$$

where n_{ei}, E_{Hi}, and E_{Li} represent the magnitude, high energy limit, and low energy limit of each individual step function used to approximate the final distribution. By applying eq. 3.82

into 3.80 the total electron current can be represented by a similar summation over all step functions:

$$I_e\left(V_p\right)=\sum_{i=1}^{N}\begin{cases}\dfrac{n_{e\,i}A_p e}{2\left(v_{H\,i}-v_{L\,i}\right)}\left(v_{L\,i}^2-v_{H\,i}^2\right) & \text{if} \quad v<v_{L\,i}\\ \dfrac{n_{ei}A_p e}{2\left(v_{H\,i}-v_{L\,i}\right)}\left(v^2-v_{H\,i}^2\right) & \text{if} \quad v_{L\,i}\le v\le v_{H\,i}\\ 0 & \text{if} \quad v>v_{H\,i}\end{cases} \tag{3.83}$$

Now that the integral kernel *K* has been obtained for a step function by plotting the singular eigen values with respect to velocity distribution a well identified gap appears as shown in figure 3.13. Next let us consider the collection of electrons by a retarding probe of cylindrical geometry, then the number density of electrons with velocity between *v* and *v*+*dv* is

$$dn=2\pi v f(v)dv \tag{3.84}$$

The contribution to the current due to electrons will be given by[33→40]

$$dI=A_p e(1-\frac{V_p}{V_o})^{1/2}\,f(v)v dn \tag{3.85}$$

where V_p is the probe voltage and V_o is the initial energy of electron. Applying the same step function and repeating the same procedure as mentioned for the planar probe then the total electron current is :

$$I_e\left(V_p\right) = \sum_{i=1}^{N} \begin{cases} \dfrac{2n_{e\,i}A_p e}{3\left(v_{H\,i} - v_{L\,i}\right)}\left(1-\dfrac{V_p}{V_o}\right)^{1/2}\left(v_{L\,i}^3 - v_{H\,i}^3\right) & \text{if} \quad v < v_{L\,i} \\ \dfrac{2n_{e\,i}A_p e}{3\left(v_{H\,i} - v_{L\,i}\right)}\left(1-\dfrac{V_p}{V_o}\right)^{1/2}\left(v^3 - v_{H\,i}^3\right) & \text{if} \quad v_{L\,i} \le v \le v_{H\,i} \\ 0 & \text{if} \quad v > v_{H\,i} \end{cases} \tag{3.86}$$

Using the formulation for EEDF reconstruction detailed in [30] and the formulation for EVDF detailed in the previous section, the reconstruction of an identical distribution either in velocity space or energy space is carried out with identical electron currents obtained by applying eqs. 3.1 and 3.88 to a known distribution, adding noise, and then reconstructing the distribution to study variation produced by the introduction of noise into the integral problem. Both reconstructions are performed using Tikhonov regularization of the respective matrix problems. The regularizing parameter is optimized so as to minimize the difference between the reconstructed solution and the starting distribution in order to provide a "best fit" comparison for both problems. A Maxwellian EEDF representing an electron density of 10^{10} and temperature of 5 eV is used to construct electron current using eq. 3.1. An EVPF representing an electron density of 10^{10} cm^{-3} and average velocity of

$\sqrt{2T_e/m_e}$ presents identical electron current as a function of probe voltage. A kernel space of $M=N=900$ where the energy ranges from 0 to 9 m/s is used. The regularized solution can be validated by taking a known distribution function f_{test}, calculating model electron current I_{etest} by the operation $I_{etest} = Kf_{test}$, adding statistical random noise of various levels to I_{etest}, and reconstructing the distribution function for comparison to the known input f_{test}. The figure below highlights this analysis for a Maxwell-Boltzmann distribution with $n_e = 10^{10}\text{cm}^{-3}$ and $T_e = 5\text{eV}$ with a signal-to-noise ratio (*SNR*) of $SNR=100$ added to the calculated current I_{etest}. As appears in figure 3.14 when Tikhonov regularization was applied to the problem it was observed that the reconstruction is identical to the original distribution up to a point which is around 1.2 m/s which is the point as seen in figure 3.13 where the well determined gap appears. After applying TSVD to the kernel matrix *K* the result is only a distribution which extends to 1.2 m/s since all the other singular eigen values are eliminated. By applying reconstruction mechanisms and numerical techniques to both planar and cylindrical kernel the results start to deteriorate at certain identified points, these points represent the beginning of the singular eigen values gap thus rendering the solution inaccurate at best.

Figures 3.14 a-b. Comparison The application of Tikhonov regularization to a maxwellian distribution with SNR 100.

Figure 3.14 a. EVDF.

Figure 3.14 b. EEDF.

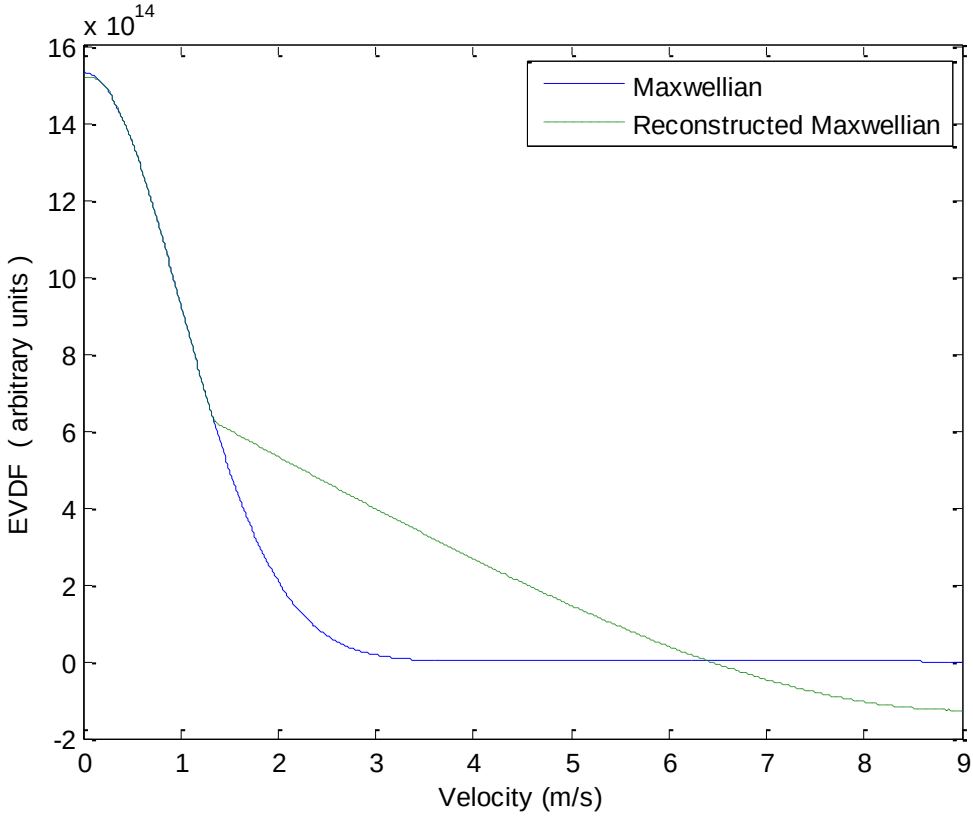
x 10^14
16
14
12
10
8
6
4
2
0
-2
0
1
2
3
4
5
6
7
8
9
EVDF (arbitrary units)
Velocity (m/s)
Maxwellian
Reconstructed Maxwellian

(a)

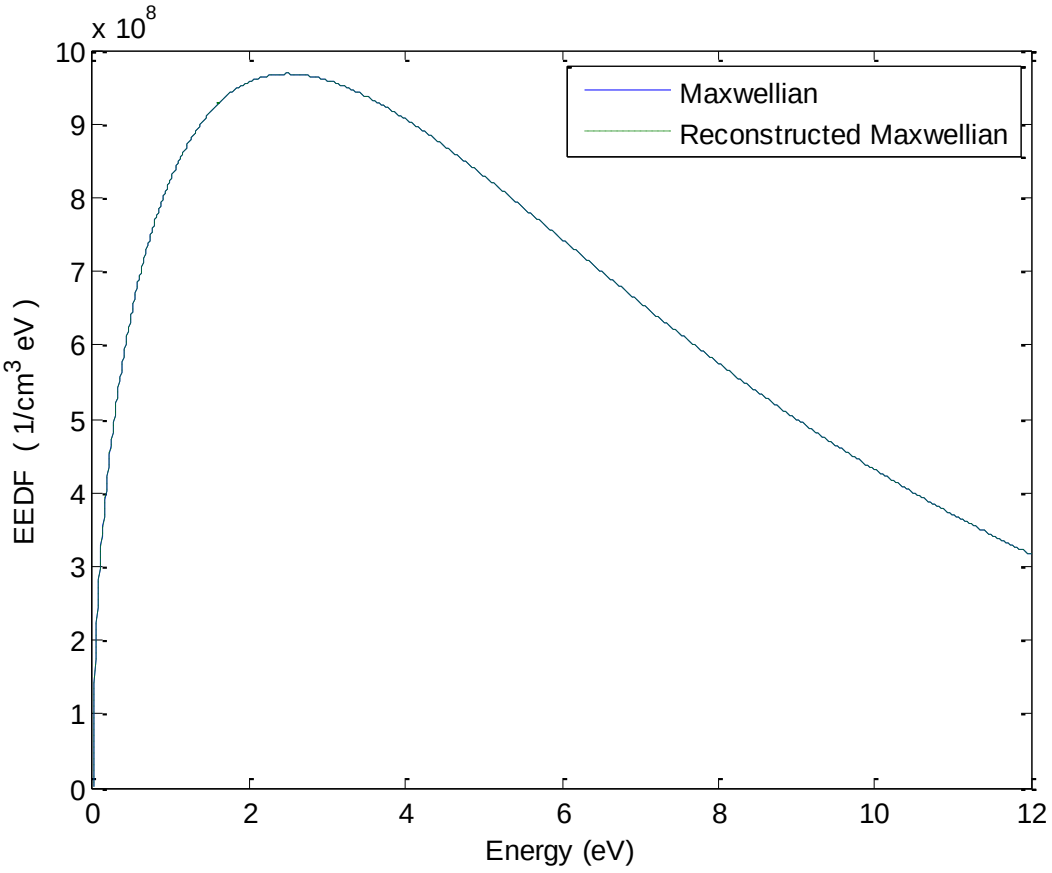
x 10^8
10
9
8
7
6
5
4
3
2
1
0
EEDF (1/cm^3 eV)
0
2
4
6
8
10
12
Energy (eV)
Maxwellian
Reconstructed Maxwellian

(b)

3.6. References

[1] Druyvesteyn M.J.,"Der Niedervoltbogen" *Z. Phys*., 64,1930, pp. 781-798.

[2] Per Christian Hansen; "Rank-Deficient and Discrete Ill-Posed Problems", Society for Industrial and Applied Mathematics, 1998, ch 5.

[3] El Saghir A., Kennedy C., Shannon S., " Electron Energy Distribution Function Extraction Using Integrated Step Function Response and Regularization Methods", *IEEE Transactions on Plasma Science*, 38(2),2010,pp. 156-162.

[4] Vogel C. R., "Computational Methods for Inverse Problems" Society for Industrial and Applied Mathematics, 2002, ch 1.

[5] Santosa F., Pao Y., Symes W., and Holland C., "Inverse Problems of Acoustic and Elastic Waves", Society for Industrial and Applied Mathematics, 1984.

[6] Craig I., and Brown J., "Inverse Problems in Astronomy", Adam Hilger, Bristol, UK, 1986.

[7] Natterer F., "The Mathematics of Computerized Tomography", Wiley, New York, 1986.

[8] Carasso A., "Overcoming Holder Discontinuity in Ill-Posed Continuation Problems", *SIAM J. Numer. Anal*., 31, 1994, pp. 444-464.

[9] Bertero M., PoggioT., and Torre V., "Ill-Posed Problems in Early Vision", *Proc. IEEE*, 76, 1988, pp. 869-889.

[10] Harrington R., "Field Computations by Moment Methods", Macmillan, New York, 1868.

[11] Menke W., "Geophysical Data Analysis: Discrete Inverse Theory", Academic Press, San Diego, 1989.

[12] Parker R, "Geophysical Inverse Theory", Princeton University Press, Princeton, NJ, 1994.

[13] Cuppen J., " A Numerical Solution of the Inverse Problem of Electrocardiography", Ph.D. Thesis, Dept. of Mathematics, University of Amsterdam, 1983.

[14] Barakat R., and Newsam G., "Remote sensing of the refractive index structure parameter via inversion of Tatarski 's integral equation for both spherical and plane wave situations", *Radio Science*, 19, 1984, pp. 1041-1056.

[15] Groetsch C., “Generalized Inverses of Linear Operators”, Marcel Dekker, New York, 1977.

[16] Bertero M., De Mol C., and Pike E., “Linear inverse problems with discrete data: I. General formulation and singular system analysis”, *Inverse Problems*, 1, 1985, pp. 301-330.

[17] Wahba G., “Ill-Posed Problems: Numerical and Statistical Methods for Mildly, Moderately and Severely Ill-Posed Problems with Noisy Data”, Technical Report 595, Dept. of Statistics, University of Wisconsin, Madison, 1980.

[18] Engl H. W., Hanke M., and Neubauer A., “Regularization of Inverse Problems”, Netherlands: Kluwer Academic Publishers, 1996, pg. 31-32.

[19] Tikhonov A. N.,and Arsenin V. Y., “Solutions of Ill Posed Problems” , ed. By John F., Washington D.C.: V. H. Winston & Sons, 1977, pg 7-9.

[20] Godyak V. A., Piejak R. B., and Alexandrovich B. M., “Probe diagnostics of non-Maxwellian plasmas” *J. Appl. Phys.,* 73 (8),1993, pp. 3657 -3663.

[21] Bernstein I. B., Greene J. M., and Kruskal M. D., “Exact nonlinear plasma oscillations”, *Phys. Rev.,* 108, 1957, pp. 546-550.

[22] Reginska T., “A regularization parameter in discrete ill-posed problems” *SIAM J Sci Comput*, 17,1996,pp.740-749.

[23] Swift J. D., and Schwar M. J., “Electrical Probes for Plasma Diagnostics”,New York: American Elsevier Publishing Company, 1969, ch 4,5.

[24] Bjork A., “Numerical Methods for Least Squares Problems”, Society for Industrial and Applied Mathematics, 1996, ch 2.

[25] Weisstein, Eric W. "Singular Value Decomposition." From MathWorld--A Wolfram Web Resource. http://mathworld.wolfram.com/SingularValueDecomposition.html

[26] Per Christian Hansen; “Analysis of Discrete Ill-Posed Problems by Means of The L-Curve”, *SIAM Review*, 34(4), 1992, pp561-580.

[27] Holloway J.P., Shannon S., Sepke S., Brake M.L., “A reconstruction algorithm for a spatially resolved plasma optical emission spectroscopy sensor” *J. Quant. Spect. And Rad. Trans*, 68(1),2001, pp.101-115.

[28] Per Christian Hansen; “The Truncated SVD as a Method for Regularization”, *BIT Numerical Mathematics*, 27, 1987, pp534-553.

[29] Knappmiller S., Robertson S., Sternovshy Z., " Metod to find the Electron Distribution Function from Cylindrical Probe Data", *Physical Review E*, 73, 2006.

[30] El Saghir A., Shannon S., "Reduction of EEDF Measurement Distortion in Regularized Solutions of the Druyvesteyn Relation ", *IEEE Transactions on Plasma Science*, 39(1) 2011, pp596-602.

[31] Golub G., Van Loan C., " Matrix Computations", John Hopkins University Press, 1996, ch 5.

[32] Lawson C., Hanson R., " Solving Least Squares Problems", Prentice-Hall, Englewood Cliffs, NJ, 1974, ch 25,26.

[33] Allen J.E., "Probe Theory-The Orbital Motion Approach", *Physics Scripta*, 45, 1992, pp. 497-503.

[34] Wing G. M., A Primer On Integral Equations of the First Kind, The Problem of Deconvolution and Unfolding, Philadelphia; Society for Industrial and Applied Mathematics, 1991, ch 6.

[35] Chung P. M., Talbot L., and Touryan K. J., "Electric Probes in Stationary and Flowing Plasmas" New York: Springer-Verlag, 1975, ch 2.

[36] Gutierrez-Tapia C., Flores-Llamas H., "A comparative analysis of the electron energy distribution function obtained by regularization methods and by a least-squares-fitting" *Phys. Plasmas*, 11(11) ,2004,pp. 5102-5107 .

[37] Ruzic D.N., AVS Monograph Series: Electric Probes for Low Temperature Plasmas, New York :American Vacuum Society Press, 1994,pp. 86-89.

[38] Volkova, L.M., Deviatov, A.M., Kralkina, E.A., Sedov, N.N., Sherif, M.A.; "The use of regularizing algorithms for calculating the electron energy", *Vestnik Moskovskogo universiteta seriia III, fizika, astronomia*., 16, 1975, pp 502-504.

[39] Chegotov M. V., "A new regularization procedure as an appropriate algorithm for the evaluation of Langmuir-probe and Thompson scattering measurements", *J. Phys. D*, 24, 1994, pg.54-62.

[40] Allen J. E., "On the Applicability of the Druyvesteyn Method of Measuring Electron Energy Distributions", *J. Phys. D: Appl. Phys.*, 11, 1978, pp. L35–L36.

[41] Hadamard J., “Lectures on Cauchy’s Problem in Linear Partial Differential Equations”, Yale University Press,1923.

CHAPTER 4

The Impact of Langmuir Probe Geometries on Electron Current Collection and the Integral Relation for Obtaining Electron Energy Distribution Functions

4.1. Introduction

In Chapter 3, methods for addressing the influence of experimental noise in electron energy distribution function analysis from Langmuir probe data were presented. A method new to Langmuir probe analysis that combined Tihkonov regularization with truncated singular value decomposition was introduced that provided highly accurate EEDF reconstructions with minimal EEDF shape distortion was presented. In this Chapter, the derivation of the actual integral relationship that defines the integral kernel *K* introduced in Chapter 3 is revisited. Specifically, the long standing assumption that the integral relationship in the electron retardation regime (from which the EEDF is extracted) is invariant with respect to probe geometry is revisited. This assumption was originally put in place to simplify the integral relationship to a derivative formuation that enabled simplier analysis. In this Chapter, the geometry invariant formulation introduced by Druyvesteyn is compared to the integral formulation originally posed by Mott-Smith and Langmuir in 1926 to determine the extent to which the geometry invariance assumption impacts cylindrical Langmuir probe analysis of EEDF's.

Langmuir probes come in many shapes and sizes. The main criteria in their design are ease of manufacture and minimal perturbation of the plasma discharge being studied. The geometry that is typically employed that meets these two criteria is a cylindrical probe

where the probe is a finite cylinder of length L and radius r_p. This probe configuration currently dominates the commercial Langmuir probe marketplace, with vendors such as Plasmart, Scientific Systems, Plasma Sensors, and Hiden Analytical offering turnkey systems with this probe geometry. Spherical probes are also employed, but are more difficult to manufacture and not as commonly used as the cylindrical option. Planar probes are a third common option, typically used under conditions where plasma isotropy around the probe cannot be assumed, but are also useful in isotropic conditions.[1] All of these systems provide a relatively straight forward means for scientists and engineers to measure plasma parameters such as electron density, ion density, electron temperature, and plasma potential.

One of the unique measurement capabilities of these Langmuir probe systems is the ability to obtain Electron Energy Distribution functions (EEDF's) from the probe's voltage vs. current response. By subtracting the ion contribution of the probe current, the shape of the electron current for probe potentials lower than the plasma potential is used to reconstruct the EEDF. In this voltage regime, the probe effectively acts as a retarding probe for the surrounding electrons, and the current response with respect to this retarding potential provides a relationship between electron energy and probe current. An integral relationship for both spherical and cylindrical geometries was originally presented by Mott-Smith and Langmuir in 1926.[2] The spherical formulation was further advanced by Druyvesteyn in 1930, providing an analytical means to obtain the EEDF from a probes electrical characteristic.[3] In its original form, it states that

$$f(E)_{E=-eV_{probe}} = -\frac{4}{A_p e^2}\sqrt{-\frac{m_e V_p}{2e}}\frac{d^2 I_e}{dV_{probe}^2} \qquad (4.1)$$

where *f(E)* is the electron energy distribution function, A_p is the surface area of the probe (typically approximated for a spherical probe by $4\pi r_p^2$ and for a cylindrical probe by $2\pi r_p L$), *e* is electron charge, m_e is electron mass, V_{probe} is probe voltage, and I_e is the electron current through the probe circuit. This formulation where the integral formulation is replaced by a differentiation of probe data enabled straight forward analysis of electron energy distribution functions through analog differentiation of measured data (such as the Boyd-Twiddy method detailed in Chapter 2) or curve fitting of discrete data sets; both of these methodologies provided a practical means to address the ill-posed nature of the original integral problem.[4,5] Because of its practical application, the Druyvesteyn relation of eq. 4.1 is the means by which all EEDF's are currently obtained from probe characteristics.

In general, the assumption of distribution isotropy and spherical probe geometry are employed to obtain the differential relationship of eq. 4.1, integrating over the full range of variables in whatever preferred coordinate system is employed. Since the range of integration spans the full range for each coordinate (ie. the geometry is not presented as a range limitation) this formulation is typically used for all probe geometries, and is valid under the assumption that the limits of integration are not defined by the probe condition. Most efforts to date have instead focused primarily on the collection of ions in this regime, as the probe's attractive potential to positive ions in combination with the spatial extent of this potential generated by the sheath surrounding the probe has presented an analytical challenge

in the subtraction of the ion current from the total probe current to obtain the electron current, particularly under conditions where the sheath thickness is on the same scale length as the probe dimension.[6,7]

In Chapter 2, the integral relationship between EEDF and electron current was reviewed, with a focus on the geometry dependence of this integral formulation. Since Druyvesteyn's original assumption that the spherical derivation applies to the cylindrical case, it has been stated by several groups that the probe geometry does not influence electron collection efficiency since the distribution function must remain constant in phase space (Liouville Theorem), and thus is coordinate system invariant.[8] However, a review of this original work by Kagen and Perel that is frequently sited refers to EEDF distortion due to probe insertion, and not the efficiency of probe collection due to geometric considerations. The principal caveat to date is that the probe geometry be purely convex so-as not to provide a mechanism for electron shading.[9]

Probe geometries may, however, present an additional mechanism for electron retardation that is not accounted for in the Druyvesteyn formulation. In the original works of Mott-Smith and Langmuir, a geometry dependence with respect to current density ratios infinitely far from the probe and the probe surface was reported.[2]

Several years after the work of Kagan and Perel, Emeleus cautioned that this geometry invariance may not be valid for "sharp" distribution functions, noting that Kagan and Perel assumed a Boltzmann energy distribution in their assertion.[10] In 2006, Knappmiller and Robertson demonstrated matching distributions functions using both cylindrical and planar probes using a geometry modified differential relation between electron current and electron

velocity distribution.[11] This collection of works and observations suggest that, at least within the context of measuring non-Maxwellian distribution functions, that the concept of geometry invariance in the electron retarding regime of a Langmuir probe characteristic needs to be revisited, and that an additional geometry dependent mechanism does exist that is not currently accounted for in EEDF analysis that employs the original formulation of Druyvesteyn.

This geometry dependent mechanism impacting electron collection originates from the centrifugal retarding potential whose strength is determined by the initial angular momentum of the system when the electrons are sufficiently far away from the probe so as not to be influenced by the probe's surrounding space charge potential. This additional term can influence the collection of electrons of a particular energy beyond that predicted by the Druyvesteyn relation; several works have previously highlighted it's importance in charge collection in both the ion saturation regime and electron saturation regime.[7,12] This influence is a function of both electron energy and probe potential and can therefore distort the EEDF integral relationship with respect to probe geometry and probe potential if not properly accounted for.

Although this mechanism has been thoroughly studied for ion interaction with biased probes, a similar study has yet to be carried out for the electron retarding region of the probe characteristic, in large part due to the long standing assumption that there is no geometry dependence in this regime as well as the substantially less subtle collection efficiency dependences in attractive potential regimes where the effective collection area varies with applied potential.

This chapter presents a formulation of the relationship between electron current, probe potential, and EEDF that accounts for this geometric term, essentially revisiting the original integral relationship posed by Mott-Smith and Langmuir for both spherical and cylindrical geometries to elucidate the impact of probe geometry on electron current collection and EEDF extraction. Specifically, we quantify the distortion of EEDF's due to probe geometry and the different integral relationships that they present and assumed to have minimal impact in the derivative formulation of Druyvesteyn. Using the techniques to solve the integral form of the problem that are detailed in Chapter 3, the distortion of the EEDF when extracted using the Druyvesteyn formulation is determined, and a methodology for the extraction of EEDF data taking into account cylindrical geometry is presented.

4.2. Formulation of The Integral Relation Between Electron Current and EEDF

The integral relation between electron current and EEDF centers on a probe with some defined finite geometry defined by a parameter r_p that provides a retarding potential for surrounding electrons. The probe surface is surrounded by a space charge sheath with some characteristic dimension *s* that is also a function of the retarding potential magnitude V_p. This sheath region separates the probe surface from an assumed isotropic uniform plasma characterized by electron density n_e and electron energy distribution function *f(E)*. This dependence between *s* and V_p is determined by the plasma conditions, particularly the magnitude of the potential and the collisionality between the electrons and the background gas. For purposes of this geometry comparison, this sheath dimension is assumed to be much

smaller than the probe geometry. Previous work has suggested a similar dependence with respect to electron repulsion around the probe, to the extent of having no impact on electron current collection.[8] These geometry parameters are detailed in Figure 4.1.

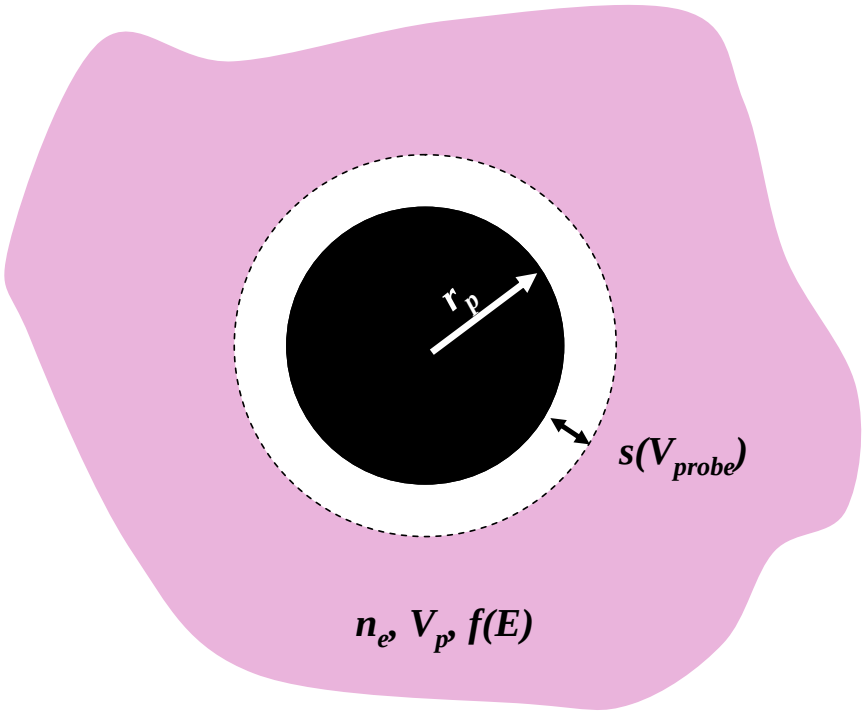

Figure 4.1. The cylindrical probe problem. The axis of the probe points out of the page. The field produced in the region defined by $s(V_{probe})$ is assumed to be purely radial.

To determine the flux of electrons incident on the probe surface as a function of applied probe potential (referenced to the plasma potential), the surrounding electrons need to be characterized with respect to their velocity relative to the probe surface. Both the magnitude of the velocity and the translational distance *b* between the velocity vector and the probe centerpoint will determine whether the electron reaches the probe surface, similar to any two body central potential problem. This translated distance can be related to the angles

of incidence θ and φ of an electron (and the more typical integral variables for calculating flux) using the cutaway illustrated in Figure 4.2.

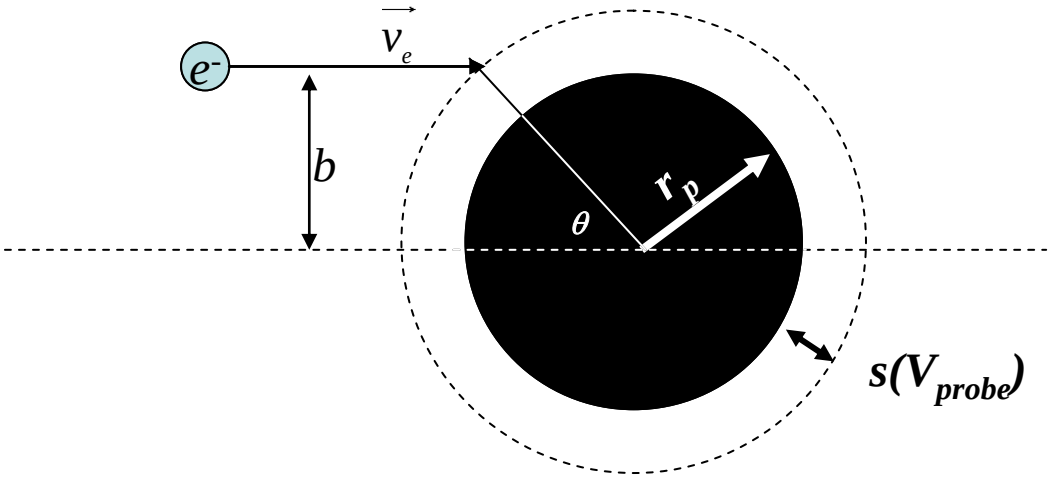

Figure 4.2. Geometry relating angle of incidence θ to probe geometry parameters r_p and $s(V_{probe})$ and the impact parameter b

To obtain the general integral solution for electron current, the EEDF is defined as an arbitrary function $f(E)$. The probe is assumed to present a space charge field that is purely perpendicular to the probe surface (ie. the finite characteristics of cylindrical probe length and subsequent complexity in field calculation [13] are not accounted for in this analysis; probe length is only used to establish a probe surface area and the probe is assumed to behave as an infinitely long cylinder with respect to field formation. Likewise, the spherical case is assumed to be a perfect sphere with no perturbation). The probe is surrounded by a space charge region defined by some V_{probe} dependent thickness s. As mentioned earlier, this sheath thickness does not significantly influence the efficiency of electron collection, and for

the purpose of illustration, the thin sheath approximation ($s << r_p$) is used for this integral formulation.[8]

To start, the number of electrons per unit volume with energy from E to $E+dE$ and angles of incidence from θ to $\theta+d\theta$ is defined by:

$$f(E)\frac{1}{2\pi}d\theta dE \tag{4.2}$$

where the angle of incidence θ is between the trajectory of the electron and the normal vector that defines the surface of the plasma / sheath interface surrounding the probe. Integrating over all angles for energies from the probe voltage to infinity defines the electron current collected by the probe as a function of applied voltage. For the cylindrical case, this integral is:

$$I\left(V_p\right)=\frac{-A_p e}{2\pi}\int_{E=V_p}^{\infty} f(E)\sqrt{\frac{2E}{m}}\int_{\theta=0}^{\frac{\pi}{2}}\cos\theta d\theta dE \tag{4.3}$$

When the relationship between the incident velocity vector normal to the probe center and the translational distance between the trajectory of the electron and the centerline of the probe's circular cross section are considered, Eq. 4.3 can be rewritten in terms of this translational distance b (typically referred to as the impact parameter in binary collisions). The geometric relationship between angle of incidence θ, probe geometry (defined by r_p and

s), and impact parameter *b* is shown in Figure 2. Assuming that $r_p >> s$ (thin sheath approximation), and noting the following geometric relationships:

$$\cos\theta = \sqrt{1-\frac{b^2}{r_p^{\,2}}}\ ,\ \sin\theta = \frac{b}{r_p}\ ,\ \theta = \arcsin\frac{b}{r_p}\ ,\ \text{and}\ d\theta = \frac{1}{\sqrt{1-\frac{b^2}{r_p^{\,2}}}}\frac{db}{r_p} \qquad \text{(4.4a-4.4d)}$$

additionally noting that the upper limit of *b* is restricted by the conservation of the two body system's angular momentum that defines the distance of closest approach for a two body system in a central potential by the relation

$$0 = 1-\frac{V(r_m)}{E}-\frac{b^2}{r_m^{\,2}} \qquad (4.5)$$

where r_m is the distance of closest approach, an upper limit for the distance of closest approach between the electron and the probe center is established. Setting this maximum distance of closest approach to r_p, Eq. 4.3 is rewritten in terms of *b* that now includes an energy and probe voltage component and establishes a convenient criteria for whether an electron is collected at the probe surface. For the cylindrical case:

$$I_e\left(V_{probe}\right) = \frac{-A_p e}{2}\int_{E=V_{probe}}^{\infty} f(E)\sqrt{\frac{2E}{m}}\int_{b=0}^{r_p\sqrt{1-\frac{V_{probe}}{E}}} db\,dE \qquad (4.6)$$

The integration about *b* yields the final integral relation accounting for cylindrical probe geometry:

$$I_e\left(V_{probe}\right)=\frac{-A_p e}{2}\sqrt{\frac{2}{m}}\int_{E=V_{probe}}^{\infty} f(E)\sqrt{E}\left(1-\frac{eV_{probe}}{E}\right)^{1/2} dE \qquad (4.7)$$

This is identical to the integral formulation presented originally by Mott-Smith and Langmuir; the commonly used Druyvesteyn formulation is derived for the spherical formulation only, and presents a very different integral relation between f(E) and Ie(Vprobe) from which eq. 4.1 is derived,

$$I_e\left(V_{probe}\right)=\frac{-A_p e}{4}\sqrt{\frac{2}{m_e}}\int_{E=V_{probe}}^{\infty} f(E)\sqrt{E}\left(1-\frac{eV_{probe}}{E}\right)dE\,. \qquad (4.8)$$

Druyvesteyn states in his original work that the differential form of this equation (eq. 4.1) can be extended to any geometry that does not have concave surfaces that would cause shading of the probe including the cylindrical integral problem of eq. 4.7; this geometric invariance was later formulated by Kagen and Purel for Maxwellian distributions, and this geometric invariance has been widely sited to extend the Druyvesteyn formulation to arbitrary probe geometries including cylindrical and planar probes.

4.3. Impact of The Cylindrical Integral Relation on EEDF Extraction Using The Druyvestyen Equation

In order to illustrate the derivation of collected electron current to the probe surface as simply as possible, the step function histogram representation of an arbitrary EEDF introduced in Chapter 3 is used to solve Equations 4.7 and 4.8 analytically for any arbitrary user defined distribution function. In this method, a simple step function of height $n_e/(E_H - E_L)$ and width $E_H - E_L$ located between $E = E_L$ and $E = E_H$ is used to represent the arbitrary EEDF $f(E)$, where n_e is the total electron density formed by the step function and E_L and E_H define the limits of the step function. This simplified model of the EEDF can be used to form more complex EEDF's such as Druyvesteyn functions and bi-Maxwellians, as well as to calculate $I_e(V_{probe})$ through summation of multiple step function with different values of n_e.

This method has been previously used to calculate electron current to a spherical probe for arbitrary EEDF's, and will be extended to cylindrical geometries in this present work.[14] It is important to note that unlike the work detailed in Chapter 3, the constructed probe current as a function of EEDF is noise free; in this chapter the systematic error generated by the integral formulation is evaluated, not the impact of experimental noise.

In order to quantify the impact of this modified integral relationship on EEDF extraction, known EEDF's are inserted into eq. 4.7 to obtain electron currents for cylindrical probes. To simplify this analysis and provide an analytical solution to eq. 4.7, the thin sheath condition is assumed, and $s(V_p) << r_p$ for all V_p. Arbitrary EEDF's are generated using a histogram representation of the distribution function, where a collection of step functions defined by

$$f(E)=\begin{cases}0 & E<E_L \\ \dfrac{n_e}{E_H-E_L} & E_L<E<E_H \\ 0 & E_H<E\end{cases} \tag{4.9}$$

are used to form distribution functions of arbitrary shape. 15] For the cylindrical case, to account for the energy component parallel to the probe axis, the step function is modified to account for the energy component on the plane perpendicular to the probe axis only (defined here as $E_{\perp}$), assuming a uniform distribution of electron energies with respect to the incident angle θ that effectively extends the step function to $E = 0$ on the low energy side while

maintaining the same integrated area under the curve:

$$g(E_{\perp})=\begin{cases}\dfrac{2n_e}{(E_L+E_H)} & E_{\perp}<E_L \\ \dfrac{2n_e}{(E_L^2-E_H^2)}(E_{\perp}-E_H) & E_L<E_{\perp}<E_H \\ 0 & E_H<E_{\perp}\end{cases} \tag{4.10}$$

Inserting this distribution function into eq. 4.7 then yields the electron current for a step function distribution,

$$I_e = \begin{cases} \dfrac{2A_p e n_e}{3\pi(E_L + E_H)}\sqrt{\dfrac{2}{m}}\,(E_L - V_p)^{3/2} & E < E_L \\ \dfrac{2A_p e n_e}{3\pi(E_L^2 - E_H^2)}\sqrt{\dfrac{2}{m}}\left[\dfrac{1}{5}(3E_H + 2V_p)(E_H - V_p)^{3/2} - E_H(E_H - V_p)^{3/2} - \dfrac{1}{5}(3E_L + 2V_p)(E_L - V_p)^{3/2} + E_H(E_L - V_p)^{3/2}\right] & E_L < E < E_H \\ 0 & E_H < E \end{cases} \quad (4.11)$$

By further restricting the upper limit of *b* in eq. 4.6 from r_p to $r_p(1-V_{probe}/E_\perp)^{1/2}$, a correction factor is applied to the total current to account for the discretized nature of the stepwise distribution function representation of *f(E)*,

$$Correction\ factor\ = \left(\frac{n}{\sum_{V_p=0}^{E_H} \sqrt{1 - \dfrac{V_p}{E_H}}} \right)^2 \quad (4.12)$$

where *n* denotes the number of discretized step functions in energy space used to represent the continuous function *f(E)*. The thin sheath simplification of eq. 4.7 allows for a direct comparison to the classical Druyvesteyn relation for a simplified step function electron energy distribution function to the integral relationship of eq. 4.8 that defines the electron current collected by a cylindrical probe. Consider a step function distribution of height $n_e/(E_H - E_L)$ and width $E_H - E_L$ located between $E = E_L$ and $E = E_H$ and equal to zero elsewhere, where $n_e = 10^{10} cm^{-3}$, $E_L = 3eV$, and $E_H = 4eV$. The spherical (Druyvesteyn) geometry electron current is calculated using the formulation of Reference 14, while the

cylindrical probe electron current is calculated using eqs. 4.4 and 4.7. A comparison of calculated results for this example is shown in Figure 4.3.

This formulation can be extended to any arbitrary distribution function by incorporating a histogram approach using overlapping step functions. The electron current for a *5eV* Maxwellian distribution with an integrated electron density of $10^{10}cm^{-3}$ is shown for both the spherical Druyvesteyn case and cylindrical cases in Figure 4.4.

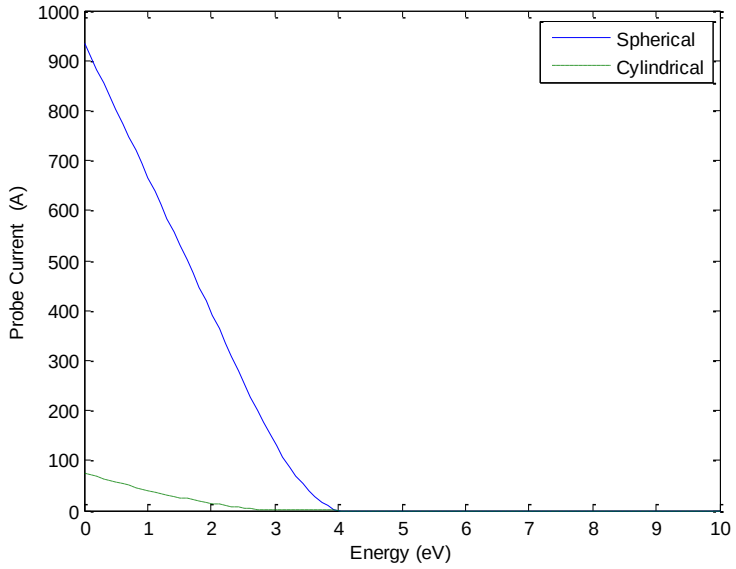

Figure 4.3. Electron current vs. probe voltage for a step function EEDF characterized by an integrated density of $10^{10}cm^{-3}$ uniformly distributed between 3eV and 4eV using the integral formulations of eq. 4.7 (cylindrical) and eq. 4.8 (spherical).

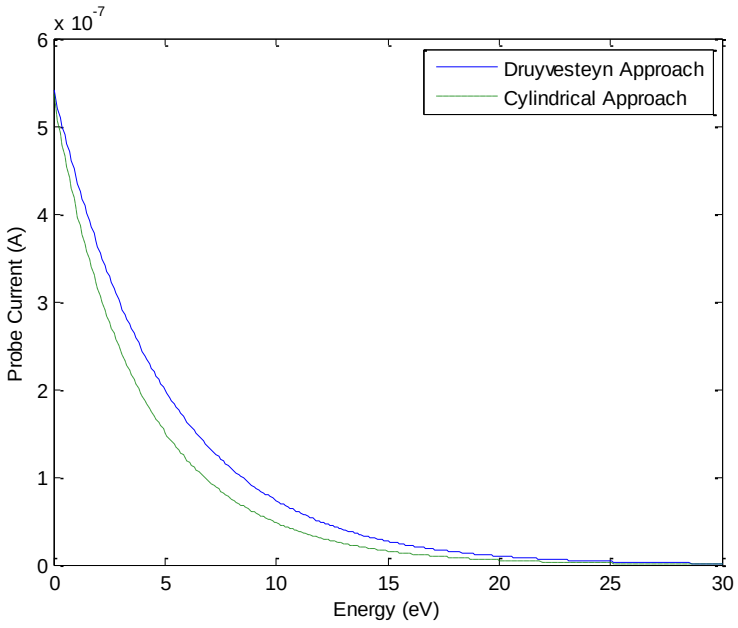

Figure 4.4. Comparison of the electron current calculated from both Druyvesteyn's relation and the cylindrical approach for a Maxwell-Boltzmann distribution where T_e = 5eV and $n_e = 10^{10}cm^{-3}$.

4.4. Numerical Results

In this section a comparison is carried out between the EEDF reconstructed by the spherical geometry from which Druyvesteyn's relation is derived and the cylindrical approach described above. This comparison is designed to illustrate the deviation from the actual EEDF when the Druyvesteyn relation that is derived from spherical geometry is used to analyze data from a cylindrical probe. To this end, a numerical study is carried out following the flow chart of Figure 4.5.

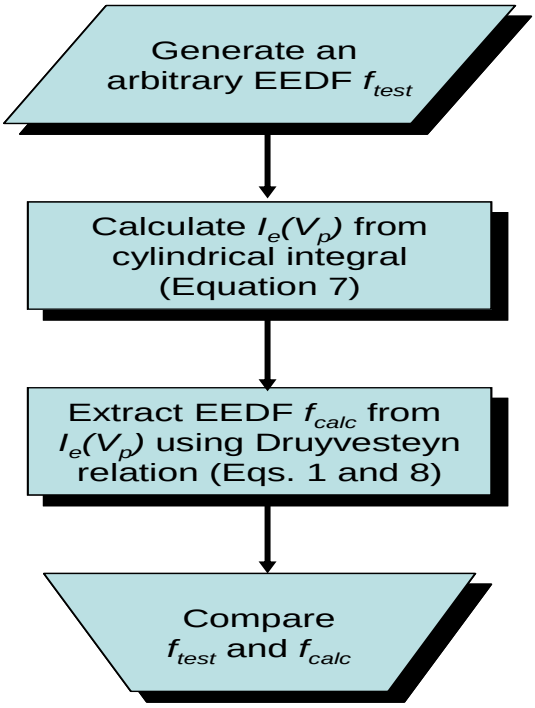

Figure 4.5. Flowchart for process used to compare cylindrical electron current to EEDF reconstruction using the Druyvesteyn formulation.

To illustrate the impact of geometry on EEDF reconstruction, this methodology was carried out for representative distribution functions of interest in low temperature plasmas.

Specifically, distributions that exhibit either Maxwell-Boltzmann distributions or high electron energy tail suppressed Druyvesteyn distributions have been observed in low temperature plasmas.[16-18] A generalized distribution function that enables intermediate forms between these two limits has been used to characterize distribution functions as a function of the energy variable power in the exponential term of the distribution function:[19]

$$f_x(E) = c_1 \sqrt{\frac{E}{T_x^{\,3}}}\, e^{-c_2\left(\frac{E}{T_x}\right)^x} \tag{4.13}$$

where

$$c_1 = x\left(\frac{2}{3}\right)^{3/2} \sqrt{\frac{\left(\Gamma\left(\frac{5}{2x}\right)\right)^3}{\left(\Gamma\left(\frac{3}{2x}\right)\right)^5}} \tag{4.14}$$

and

$$c_2 = \left(\frac{2\Gamma\left(\frac{5}{2x}\right)}{3\Gamma\left(\frac{3}{2x}\right)}\right)^x \tag{4.15}$$

where $\Gamma(\zeta)$ is the Gamma function of ζ.

Note that when $x = 1$, eqs. 4.13-4.15 give the Maxwell-Bolzmann distribution function. When $x = 2$, eqs. 4.13-4.15 give a Druyvesteyn distribution function. As x varies between 1 and 2, a smooth transition between these two distributions can be produced. This distribution provides a means for characterizing an electron energy distribution function in terms of the variable x, and has recently been used to provide a means for elucidating EEDF functionality from optical emission spectroscopy data.[20]

For the purpose of understanding the impact of the integral formulation on the reconstructed EEDF, this x parameter is used to evaluate the sensitivity of the analysis to the

shape of the final solution. As will be shown in the next section, as x increases and the distribution function becomes "less Maxwellian" the level of distortion in the reconstruction becomes more pronounced.

To illustrate the impact of the integral formulation on common representations of the electron energy distribution, two distributions (Maxwell-Boltzmann and Druyvesteyn) with similar characteristics ($n_e = 10^{10}\text{cm}^{-3}$ and $T_x = 5\text{eV}$) were compared. Figures 4.6 and 4.7 illustrate the results of this numerical exercise, with the actual EEDF and reconstructed EEDF for each distribution overlaid for comparison. Additionally, the error in the reconstructed distribution's average energy (effective electron temperature) and total electron density are illustrated in Figure 4.8.

Figures 4.6 a-c. Numerical comparison between Druyvesteyn's relation and the cylindrical approach using the methodology outlined in Section 3 for a Maxwell-Boltzmann distribution with $T_e = 5eV$ and $n_e = 10^{10}cm^{-3}$. Three graphical representations of the results are provided for comparison.

Figure 4.6 a. EEDF log plot.

Figure 4.6 b. EEDF log-log plot.

Figure 4.6 c. EEPF ($f(E)/E^{1/2}$ vs. E) log plot.

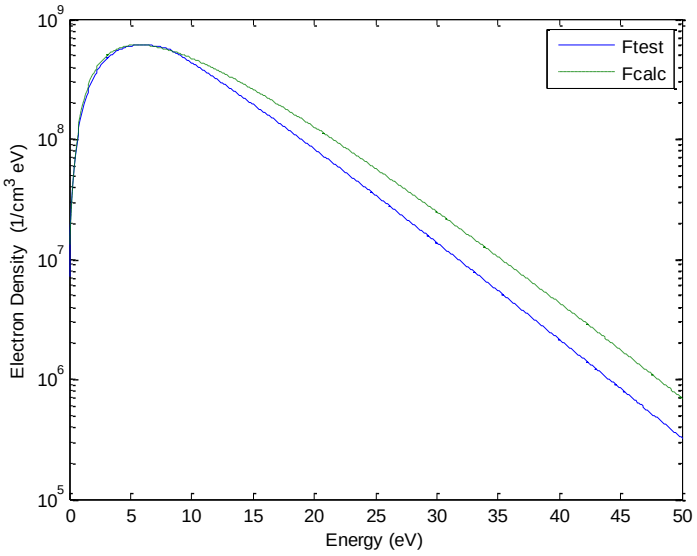
Ftest
Fcalc
Electron Density (1/cm3 eV)
Energy (eV)
10^9
10^8
10^7
10^6
10^5
0
5
10
15
20
25
30
35
40
45
50

(a)

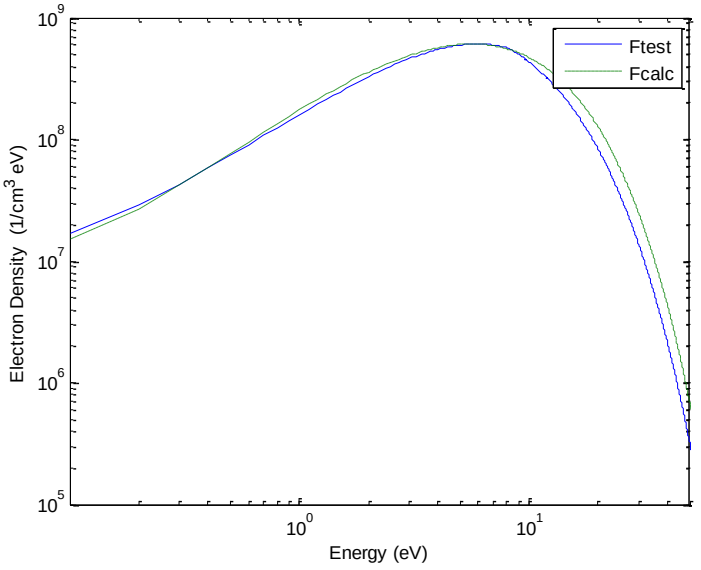
Ftest
Fcalc
Electron Density (1/cm3 eV)
Energy (eV)
10^9
10^8
10^7
10^6
10^5
10^0
10^1

(b)

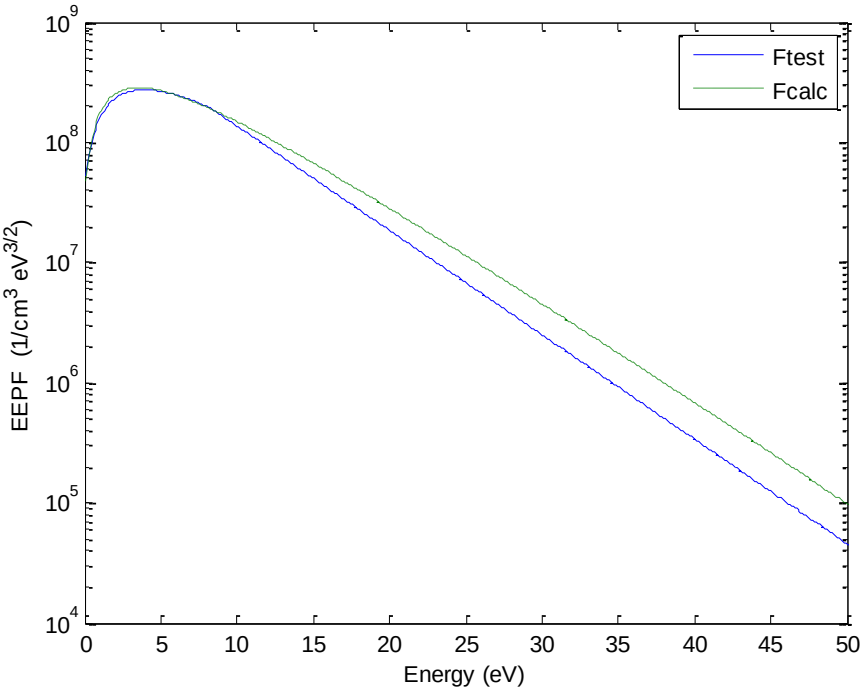
Ftest
Fcalc
EEPF (1/cm3 eV3/2)
Energy (eV)
10^9
10^8
10^7
10^6
10^5
10^4
0
5
10
15
20
25
30
35
40
45
50

(c)

Figures 4.7 a-c. Numerical comparison between Druyvesteyn's relation and the cylindrical approach using the methodology outlined in Section 3 for a Druyvesteyn distribution with $T_e = 5eV$ and $n_e = 10^{10}cm^{-3}$. Three graphical representations of the results are provided for comparison.

Figure 4.7 a. EEDF log plot.

Figure 4.7 b. EEDF log-log plot.

Figure 4.7 c. EEPF ($f(E)/E^{1/2}$ vs. E) log plot.

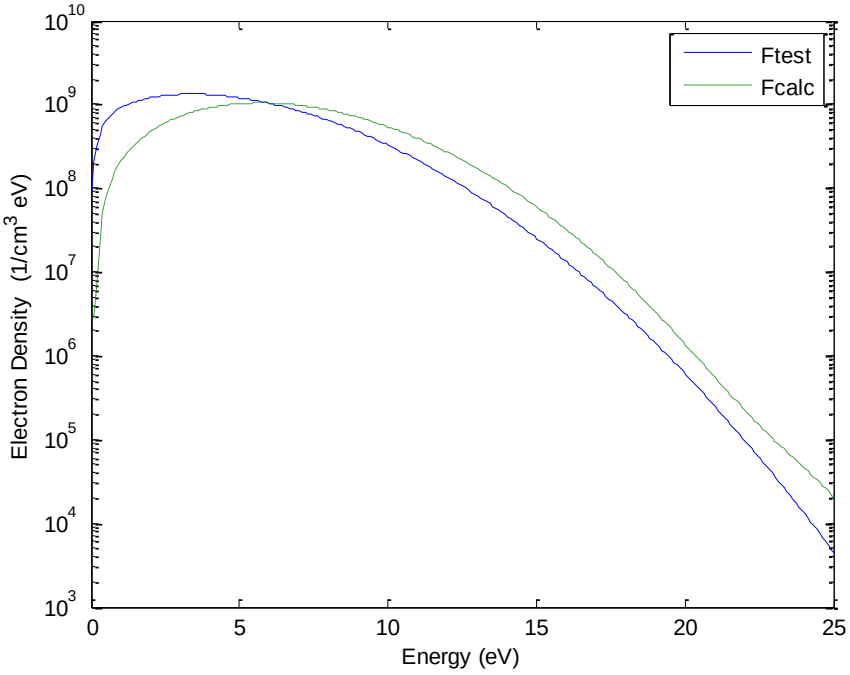
Ftest
Fcalc
Electron Density (1/cm3 eV)
Energy (eV)
10^10
10^9
10^8
10^7
10^6
10^5
10^4
10^3
0
5
10
15
20
25

(a)

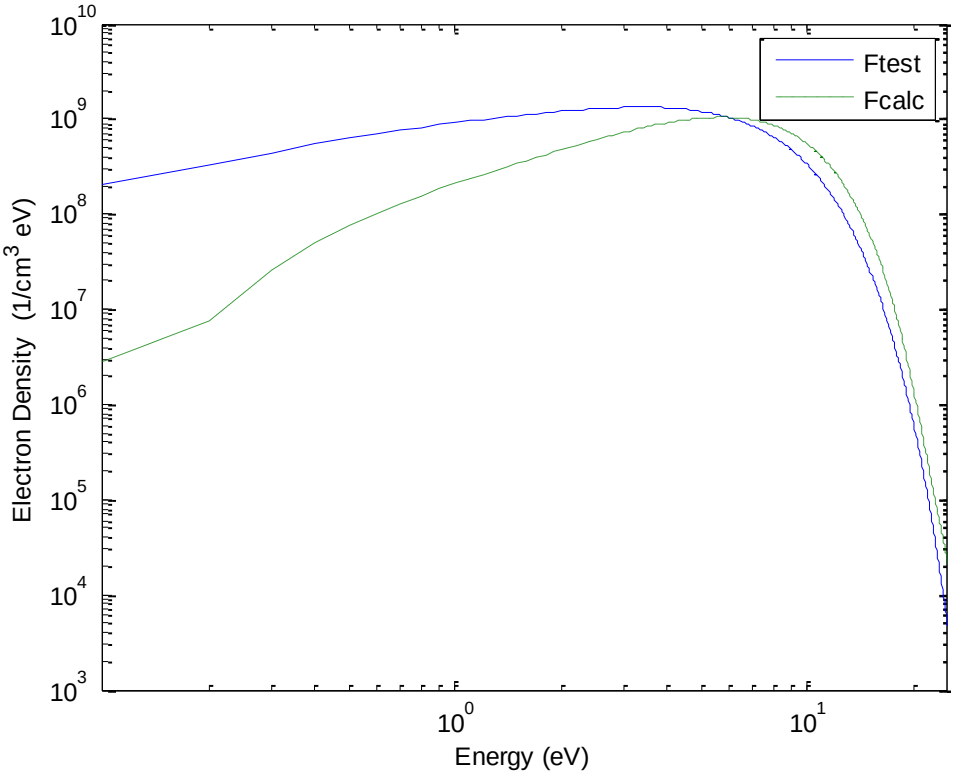
Ftest
Fcalc
Electron Density (1/cm3 eV)
Energy (eV)
10^10
10^9
10^8
10^7
10^6
10^5
10^4
10^3
10^0
10^1

(b)

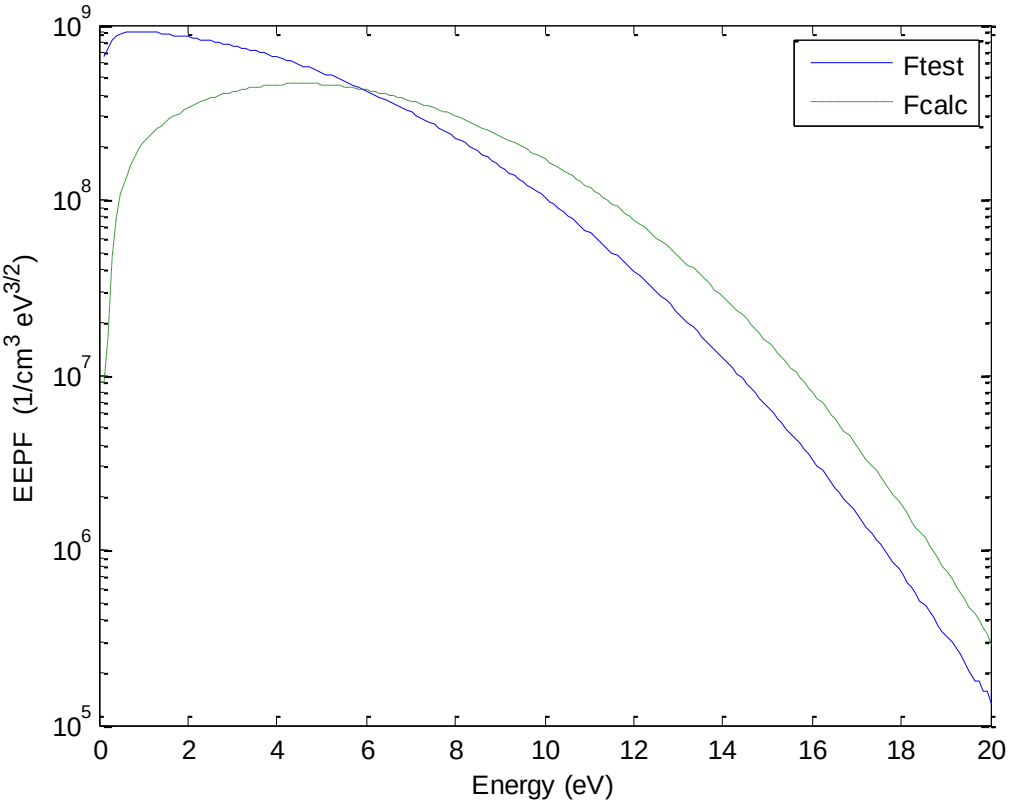
Ftest
Fcalc
EEPF (1/cm3 eV3/2)
Energy (eV)
10^9
10^8
10^7
10^6
10^5
0
2
4
6
8
10
12
14
16
18
20

(c)

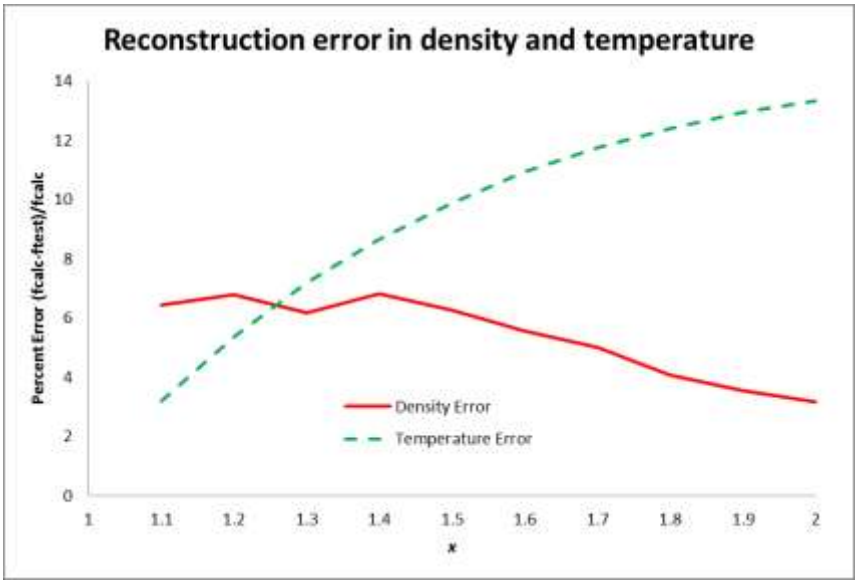

Figure 4.8. Reconstructed error in integrated density (solid line) and average energy (dashed line) as a function of *x*.

4.5. Discussion

A comparison of the test distributions are summarized in Figures 4.6-4.8. Figure 4.6 shows a comparison of a test Maxwell Boltzman distribution plotted against a calculated distribution obtained using the flowchart in Figure 4.5. Figure 4.7 shows a similar comparison for a Druyvesteyn distribution. Both Figure 4.6 and Figure 4.7 show lin/log (a), log/log (b), and electron energy probability function lin/log graphical representations of the distributions. These are selected for comparison due to their ability to highlight key difference in the curves and present a comparison in a format that is commonly employed in Langmuir probe analysis. Figure 4.8 highlights the trend in distribution function error with

respect to average electron temperature and total electron density as a function of the x parameter defined by eqs. 4.13-4.15.

The reconstruction of the Maxwell-Boltzmann distribution shown in Figure 4.6 matches up very well for temperatures out to $2T_e$. For energies greater than $2T_e$, the overall shape of the distribution is maintained, but with a slightly elevated tail temperature (as noted by the slightly shallower tail slope on the log). Compared to the typical uncertainty of experimental Langmuir probe measurements, these distortions are minimal, accounting for a temperature error on the order of less than 2%, and the analysis appears to be consistent with the original assumption of Druyvesteyn as well findings of Kagen et. al. with respect to the impact of probe geometry on electron energy distribution function measurement.

The reconstruction of the Druyvesteyn distribution shown in Figure 4.7 demonstrates how this geometric invariance does begin to impact non-Maxwellian EEDF extraction. At low temperatures (less than Te), the calculated distribution presents a significantly underestimated density profile. At higher temperatures (~2Te), the shape of the distribution recovers and the tail trend with energy is maintained, albeit at a slightly elevated density level. Interestingly, the integrated distribution yields minimal error in total electron density; the geometric effect appears to only substantially impact distribution shape and therefore temperature measurement.

As the distribution function is transitioned from Maxwellian to Druyvesteyn by performing the same analysis as a function of x using eqs. 4.13-4.15, a clear trend with respect to deviation in average electron temperature obtained by the first moment of the

distribution can be seen. As x increases (and the distribution function becomes "less Maxwellian") there is a gradual increase in the difference between the test distributions first moment and the calculated distribution's first moment. The error in the zero moment (integrated density) remains relatively constant, and is at a level that would be inconsequential in most probe experiments. This trend is consistent with the prediction of Emeleus that the assumption of probe geometry invariance in EEDF reconstruction may have to be reconsidered for non-Maxwellian distribution functions.

4.6. Conclusions

In conclusion, using the Druyvesteyn relation for EEDF analysis of data obtained using a cylindrical Langmuir probe may generate marked distortion of the distribution function shape, particularly for highly non-Maxwellian distribution functions. This distortion is due to the geometry dependent integral relationship between electron current and EEDF originally presented by Mott-Smith and Langmuir and later generalized by Druyvesteyn in his formulation of the more commonly used derivate relationship used for EEDF extraction. The derivative formulation does provide an adequate reconstruction of "near-Maxwellian" distributions. However, for non-Maxwellian profiles, particularly those transitioning to a more Druyvesteyn-like distribution shape, an integral solution that incorporates the original cylindrical formulation presented by Mott-Smith and Langmuir in 1926 may be needed.

It should be noted that although the derivation in this chapter is different from what Druyvesteyn suggested or what was carried out in chapter 3but the end result is still the

same, in which in both cases the problem is discretely ill-posed. By carrying out a comparison between their singular eigen values it can be observed that both of them are close regarding the degree of ill-posedness, which suggests that the techniques discussed previously (ch. 3) to solve such problems are applicable to the case described in this chapter.

4.7. References

[1] Sheridan TE, Goeckner MJ, Goree J., "Electron Distribution Functions in a Sputtering Magnetron Discharge", *Jpn. J. Appl. Phys*., 34(1) No. 9A. 1995, pp. 4977-4982.

[2] Mott-Smith HM, Langmuir I., "The Theory of Collectors in Gaseous Discharges" *Phys. Rev.*, 28, 1926, pp. 727-763.

[3] Druyvesteyn MJ., " Der Niedervoltbogen. Zeitschrift für Physik", *A Hadrons and Nuclei*, 64(11-12). 1930, pp. 781-798.

[4] Boyd RLF, Twiddy ND., "Electron Energy Distributions in Plasmas I", *Proc. R. Soc. Lond. A*, 250, 1959, pp. 53-69.

[5] Crowley B, Dietrich S., "A Langmuir probe system incorporating the Boyd-Twiddy method for EEDF measurement applied to an inductively coupled plasma source", *Plasma Sources Sci. Technol*., 18, 2008, 014010.

[6] Thornton JA., "Comparison of theory and experiment for ion collection by spherical and cylindrical probes in a collisional plasma", *AIAA Journal*, 9, 1971, pp 342.

[7] Laframboise JG., "Theory of spherical and cylindrical Langmuir probes in a collisionless, Maxwellian plasma at rest", UTIAS Report Number 100,1966.

[8] Sudit ID., "Langmuir Probe and Optical Emission Diagnostics for Low Pressure DC Discharges", The University of Wisconsin – Madison (PhD Thesis), 1992, pp 75-83.

[9] Kagan YM, Perel VI., "Probe Methods in Plasma Research", *Usp. Fiz. Nauk*, 81, 1963, pp. 409-452.

[10] Emeleus KG., "Electron reflection in probe analysis of plasmas", *Physical Letters A*, 71A(2,3), 1979, pp. 231-232.

[11] Knappmiller S and Robertson S., "Method to find the electron distribution function from cylindrical probe data", *Phys. Rev. E*, 73, 2006, 066402.

[12] Chen F. F., "Electric Probes for Plasma Diadnostics Techniques", ed. Huddlestone R. H., and Leonard S. L., (New York Academic), 1965, chapter 4, pp 113–200.

[13] Hoskinson AR, Hershkowitz N., "Effect of finite length on the current–voltage

characteristic of a cylindrical Langmuir probe in a multidipole plasma chamber", *Plasma Sources Sci. Technol.*, 15, 2006, pp. 85–90.

[14] El Saghir A, Kennedy C, Shannon S., "Electron Energy Distribution Function Extraction Using Integrated Step Function Response and Regularization Methods" *IEEE Trans. Plasma Sci*., 38(2), 2009, pp. 156-162.

[15] El Saghir A, Shannon S., "Reduction of EEDF Measurement Distortion in Regularized Solutions of the Druyvesteyn Relation", *IEEE Trans. Plasma Sci.,* 39(1), 2010, pp. 596-602.

[16] Godyak V, Demidov V., "Probe Measurements of Electron Energy Distributions in Plasmas: What Can We Measure and How Can We Achieve Reliable Results?", *To appear in Plasma Sources Science and Technology*, 2011.

[17] Lee HC, Lee MH, Chung CW., "Low energy electron heating and evolution of the electron energy distribution by diluted O_2 in an inductive Ar/O_2 mixture discharge", *Phys. of Plasmas*, 17, 2010, 013501.

[18] Godyak VA, Piejak RB, Alexandrovich BM., "Electron energy distribution function measurements and plasma parameters in inductively coupled argon plasma", *Plasma Sources Sci. Technol.*, 11, 2002, pp.525-543.

[19] Gundmondsson JT ., “On the effect of the electron energy distribution on the plasma parameters of an argon discharge: a global (volume averaged) model study”, *Plasma Sources Sci. Technol.*, 10, 2001, pp. 76-81.

[20] Boffard JB, Jung RO, Lin CC et. al., “Depletion of high energy electrons in argon inductively coupled plasmas”, *Submitted to Plasma Souces Sci. Technol*. 2011.

CHAPTER 5

Experimental Setup and Results

In Chapter 3 and Chapter 4, methods for obtaining more accurate electron energy distribution functions with less distortion over a large range of energies were presented. In this chapter this expanded capability of EEDF analysis is demonstrated in two cases. The first case is a comparison between our hybrid method and Savitzky-Golay filtering used by a research group in University of Kansas. The second case is an experiment conducted in an inductively coupled low pressure argon plasma with dilute hydrogen addition. The conditions where dilute hydrogen added to argon plasma produce subtle changes in the high energy tail of the EEDF that have been theoretically demonstrated but not experimentally shown, [1], and therefore present a compelling test bed for these analysis methods. In Chapter 5, the experimental setup including the plasma chamber and the Langmuir circuit will be described. EEDF reconstruction for a range of hydrogen additions will be presented.

5.1. Experimental Validation of the Hybrid Model

In this experiment, an RF compensated Langmuir probe was used to acquire current as a function of probe voltage at the center of an inductively coupled reactor for plasma etching of GaAs. Pressure, feedgas (SF_6, BCl_3, and N_2) and source power were varied; probe traces were then acquired across this process space in order to study trends in plasma condition with respect to these process conditions. EEDFs were extracted from these traces using both the

Hybrid method and data smoothing and compared. Across the entire process space, the Hybrid method demonstrated improvement in both EEDF shape and energy range compared to S-G filtering techniques. Figure 5.1 illustrates this comparison. Figure 5.1a compares both techniques for data obtained as a function of pressure for N_2 at 50W power. In general, the hybrid filter and the S-G filter have similar global trends with respect to EEDF. However, the overall shape of the hybrid filter does not have the high level of distortion seen in the S-G reconstruction. At high pressures the S-G filter fails to capture the low energy portion of the distribution compared to the Hybrid which shows a smooth curve. Figure 5.1b compares both reconstruction techniques as a function of source power for SF_6 at 50mtorr pressure. Again, both techniques demonstrate similar trends with respect to process condition, with the hybrid method showing improved levels of distortion in the final reconstruction. The S-G filter captures the distribution up to 11 eV and beyond that the distribution begins to deteriorate due to the high level of noise, while the Hybrid method can extend to 20 eV.

5.2. Argon-Hydrogen plasmas in an ICP Experimental Cell

Dilute amounts of hydrogen gas added to argon plasmas have demonstrated the ability to modify the overall shape of the electron energy distribution function. Bogaerts et.al. demonstrated computationally the influence of as little as 1% hydrogen dilution in the EEDF of a capacitively driven argon plasma.[1] Based on these original computational results, the impact of dilute hydrogen addition to argon plasmas was studied to demonstrate the capabilities of the hybrid reconstruction method to capture these trends.

The experiment was performed in a modified Gaseous Electronics Conference (GEC) RF (13.56 MHz) Reference cell. The GEC cell was first developed in 1988-1989 to allow researchers to compare between experimental data and simulated or modeled data.[2,3] The main chamber, ports, and manifolds are constructed from ultrahigh vacuum stainless-steel components. The original GEC cell had two four inch diameter electrodes spaced one inch apart. Later, a standard design for an inductively coupled "pancake" source that could replace the top electrode was introduced.[4,5]

This modification provided a reference cell capable of operating in higher electron density modes than the original reference cell. In the modified system where the experiments detailed in this chapter were conducted, the upper electrode was replaced with this inductive source and lower electrode of the GEC cell was removed. A photograph of an argon/hydrogen plasma in this system (including the position of the Langmuir probe in this study) is shown in figure 5.2.

This modification provided a reference cell capable of operating in higher electron density modes than the original reference cell. In the modified system where the experiments detailed in this chapter were conducted, the upper electrode was replaced with this inductive source and lower electrode of the GEC cell was removed. The upper electrode inductively coupled plasma source (ICP) assembly is shown in figure 5.3. The ICP source is an antenna which consists of five turn spiral coil (water cooled copper) through which RF power is coupled into the plasma. The coil is placed above a quartz disk outside the cell. The RF generator (EGR 4800-B) can provide power up to 600 watts of power at a frequency of 13.56MHz.

Figures 5.1 a-b. Comparison between the Hybrid method and Savitzky-Golay filter, the dotted line represents the S-G filter and solid ine represents the Hybrid method.

Figure 5.1 a. Pressure sweep.

Figure 5.1 b. Power sweep.

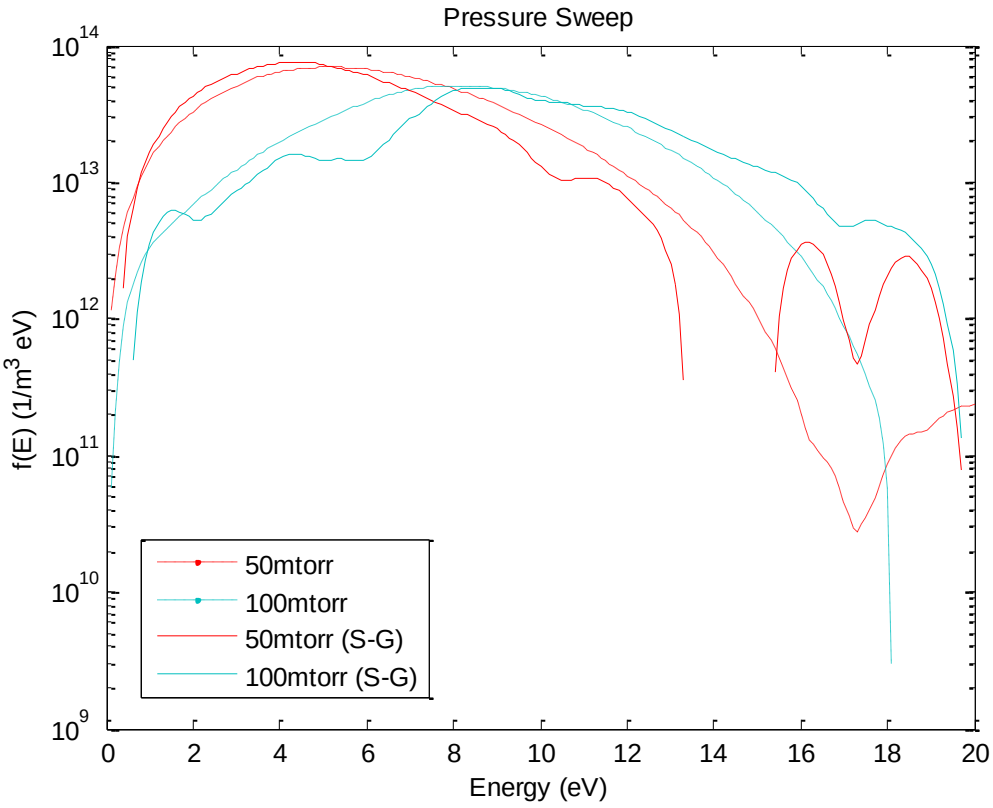
Pressure Sweep
f(E) (1/m3 eV)
Energy (eV)
50mtorr
100mtorr
50mtorr (S-G)
100mtorr (S-G)

(a)

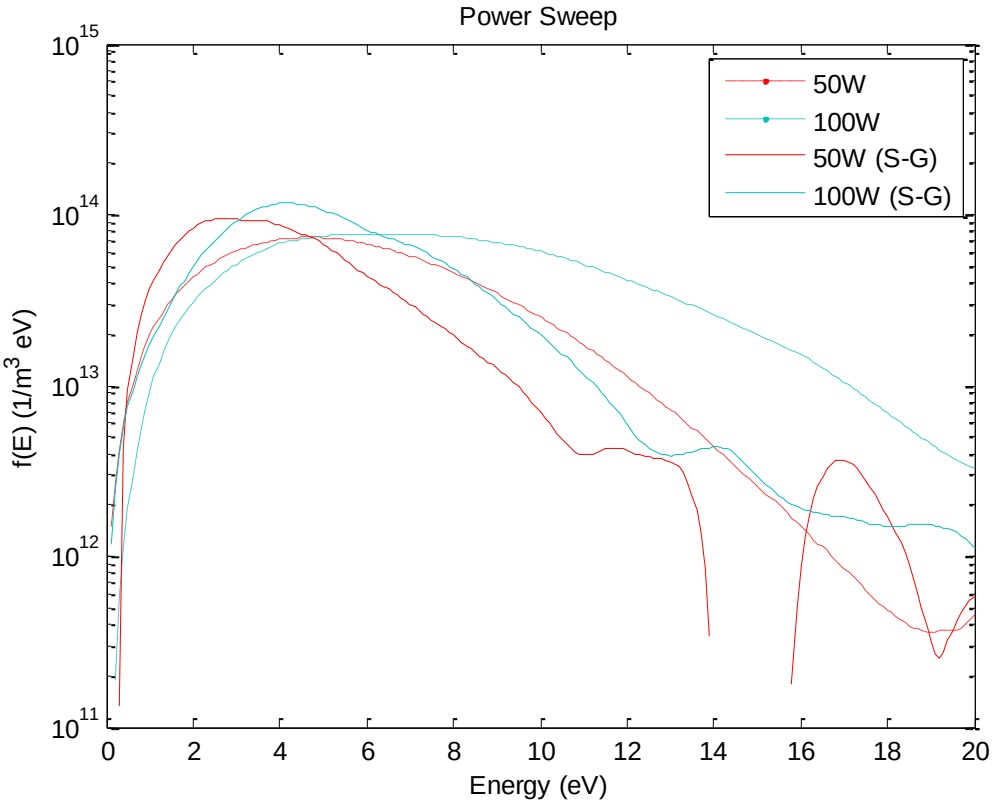
Power Sweep
50W
100W
50W (S-G)
100W (S-G)
f(E) (1/m3 eV)
Energy (eV)
10^15
10^14
10^13
10^12
10^11
0
2
4
6
8
10
12
14
16
18
20

(b)

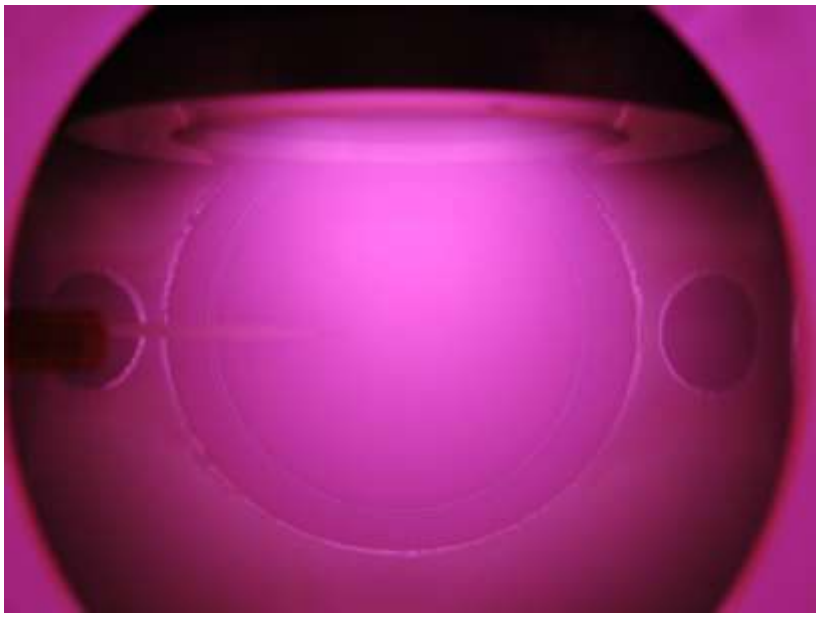

Figure 5.2. Modified GEC reference cell with top inductive electrode. The Langmuir probe (also pictured) is centered in the discharge approximately two inches from the quartz window on the top electrode.

An L-type matching network with two variable vacuum capacitors provide impedance matching for the power delivery system, thereby minimizing reflected power back to the RF generator. Forward and reflected power was measured using a Bird Technology Tru-Line power meter. The matching network's variable capacitors were manually tuned for each individual run to provide less than 2% reflected power to the generator. The power settings of the generator were controlled externally through 8116A Pulse/Function Generator. This expanded operation of the generator, enabling pulsed RF operation as well as waveform synchronized operation with additional sources. Neither of these modes of operation was used in these experiments. Instead, the ICP source was driven by a constant waveform, constant sinusoidal waveform drive similar to a standard radiofrequency generator.

Argon and hydrogen gas flow was controlled through an MKS Model 247D Four Channel Power Supply and Readout. Gas pressure was controlled by an MKS Baratron Model 629D connected to an MKS Model 250E Pressure Controller. The pressure was manually tuned in the conductance of the vacuum system by setting the position of a sliding gate valve. Vacuum pumping was provided through a standard turbo pump / mechanical roughing pump setup.

5.3. Langmuir Probe

In this work the Langmuir probe used was constructed in the lab. The Langmuir probe consisted of a hollow copper tube soldered to a BNC connector. At the top of the copper tube a long thin tungsten wire was inserted which acted as the probe tip. A ceramic tube surrounded the tungsten wire. This ceramic tube was used to control the length of the tungsten exposed to the plasma (in this experiment the length was 1 cm and the diameter of the probe was 0.01 inch) as shown in figure 5.4. It should be noted that the portion of the probe where the copper is soldered to the BNC is surrounded with a stainless steel tube which is glued to the BNC using an ultra high vacuum glue. The purpose of the stainless steel tube is to absorb any shock or pressure exerted on the probe while being inserted into the cell to prevent the ceramic from breaking. The probe was constructed so it can move from the chamber wall to the center of the discharge.

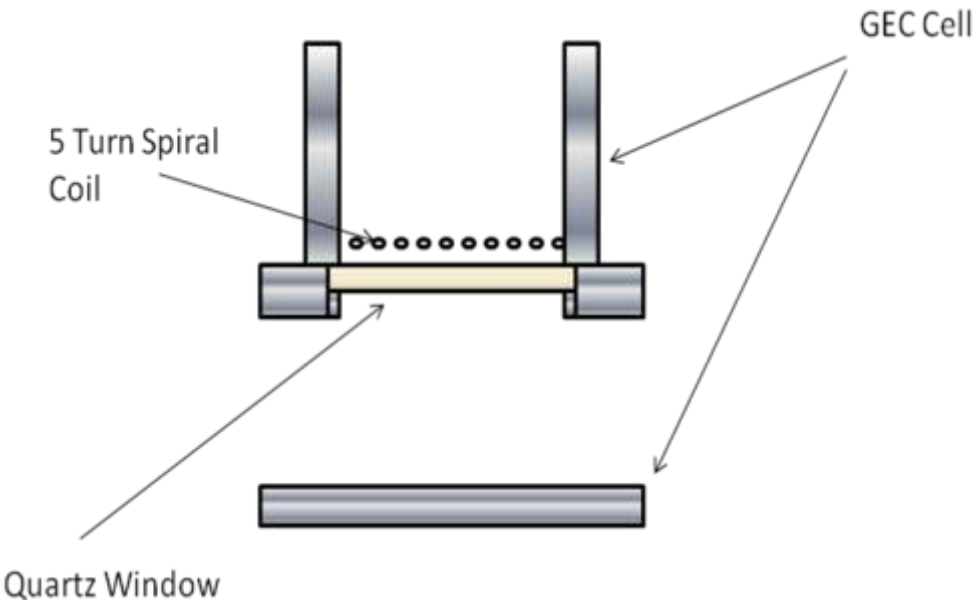

Figure 5.3. Experimental Setup

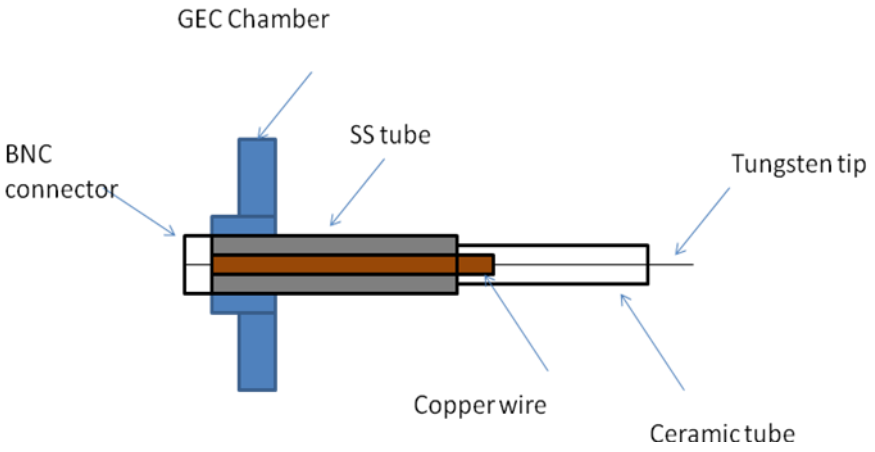

Figure 5.4. Cross section of the Langmuir probe setup

5.4. Langmuir Probe System

The technique used for driving the probe over a specified range of potentials is the pulse method. The pulse method involves biasing the probe with a steady potential and then superimposing a voltage pulse of known amplitude. At the instant of superimposing the pulse a measurement of the corresponding change in the probe current is carried out. For this experiment, an SRS DG 535 delay generator is connected in series to a DEI PVX 4140 Pulse generator. Two SRS PS 325 Voltage supplies are connected to the Pulse generator where one of the supplies is positively biased while the other is negatively biased. The output from the Pulse generator is connected to a filter circuit. The purpose of the filter is to suppress the RF frequency. The current collected by the probe after passing through the filter, passes through a Tektronix P5200 Differential Probe which is connected to a Lecroy 6100 Wave Runner oscilloscope. A Matlab code downloads the information from the oscilloscope to spread sheets on the lab computer. A schematic drawing of the probe setup is shown in figure 5.5.

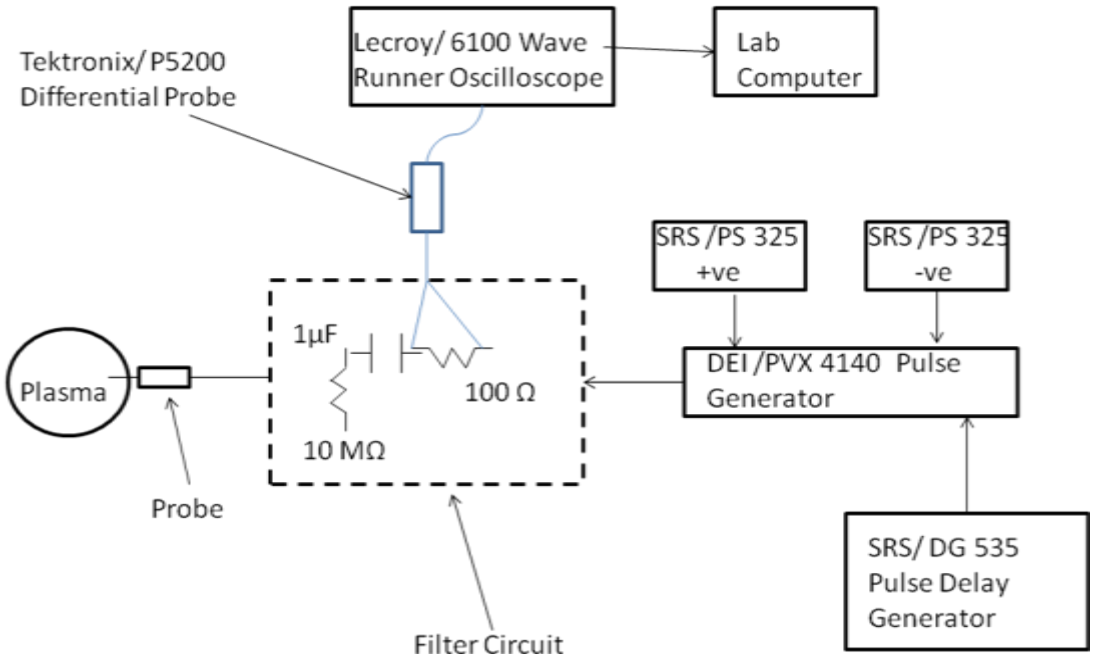

Figure 5.5. Langmuir circuit.

5.5. Results

The experiment consists of measuring the I-V curves for different argon/hydrogen mixtures as shown in figure 5.6 and through our methodology obtain the EEDFs. The results represented in figures 5.7 and 5.8 are for a 140W, 50 mtorr, and 120W 40 mtorr plasma, with 300 sccm total gas flow rate. In figure 5.8a. the three argon/hydrogen mixtures that were used are 98%Ar/2%H_2, 95%Ar/5%H_2, and 90%Ar/10%H_2 as for figure 5.8b. the compositions were 100% Ar, 97%Ar/3%H_2, 91%Ar/9%H_2, and 90%Ar/10%H_2. Gas composition was controlled by scaling the corrected flows of each gas through independent gas delivery systems consisting of one mass flow controller for each gas and an up-stream mixing manifold that combined the gases prior to entering the GEC reference cell.

As for the probe, it was placed in the center of the chamber at a distance of approximately 13 cm from the window, and the voltage sweep across the probe ranged from -10V to +20V, , providing adequate data range to capture the ion saturation regime, electron saturation regime, and transition regime.

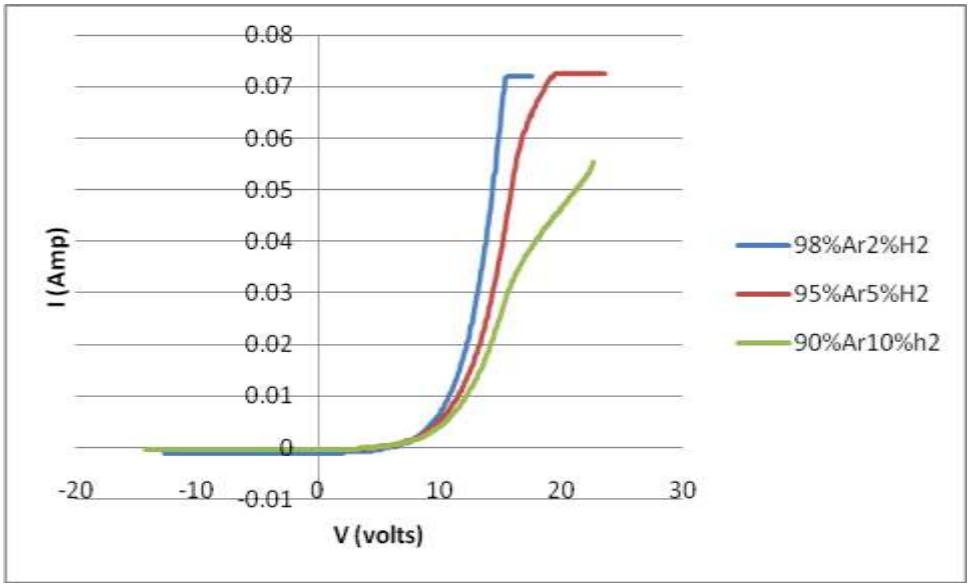

Figure 5.6. I-V curves for different argon/hydrogen mixtures at 140W and 50mtorr.

In this section we demonstrate the impact of probe geometry on EEDF extraction discussed in chapter 4 with experimental data, as well as measure EEDFs for different argon and hydrogen mixtures, utilizing the enhanced reconstruction capabilities of the hybrid method, and studying the behavior of the EEDF with respect to increasing hydrogen content.

The influence of probe geometry in EEDF reconstruction was accomplished by comparing EEDF's computed by both Druyvesteyn's relation and our Cylindrical method for the same data set. This comparison is shown in figure 5.7 for a 2% and 10% diluted

argon/hydrogen plasma at 50mTorr and 140W ICP power. For the EEDF's obtained under these conditions,there exists a small shift in the peak while the shift in the high energy tail is significant which is mainly apparent for the case of 90%Ar/10%H_2.

Figures 5.7 a-b. Comparison between Druyvesteyn's method and our Cylindrical method.

Figure 5.7 a. 50mtorr/140W(98%Ar/2%H_2) EEDFs.

Figure 5.7 b. 50mtorr/140W(90%Ar/10%H_2) EEDFs.

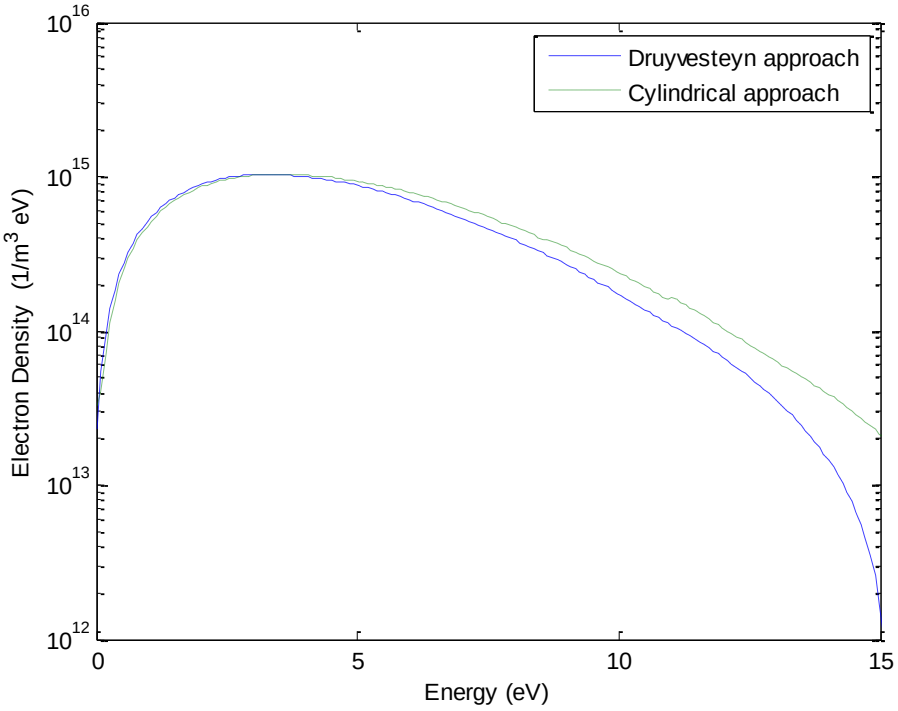
Druyvesteyn approach
Cylindrical approach
Electron Density (1/m3 eV)
Energy (eV)
10^16
10^15
10^14
10^13
10^12
0
5
10
15

(a)

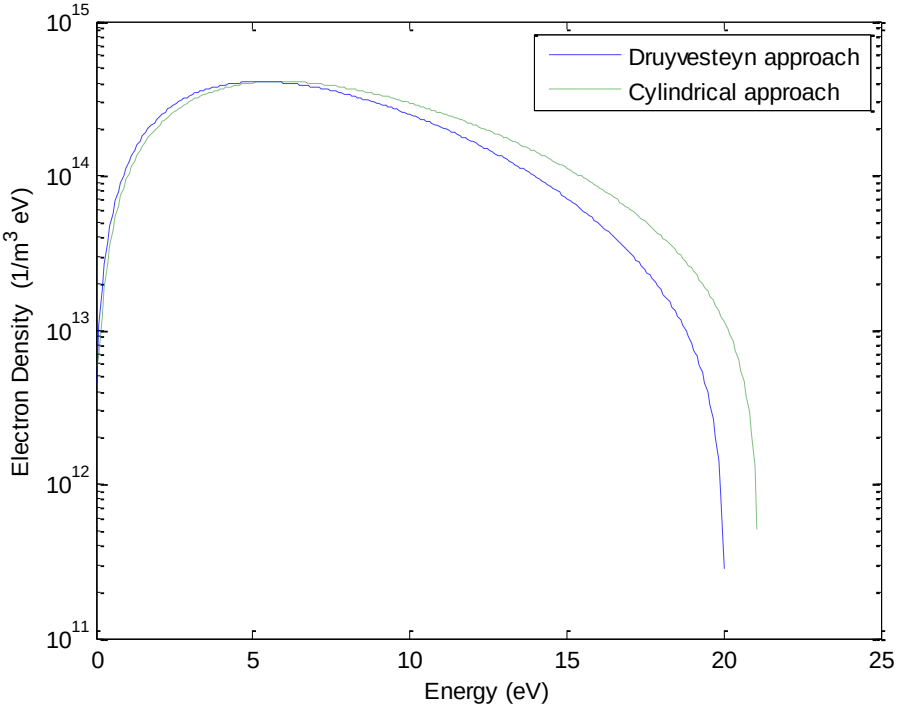
Druyvesteyn approach
Cylindrical approach
Electron Density (1/m3 eV)
Energy (eV)
10^15
10^14
10^13
10^12
10^11
0
5
10
15
20
25

(b)

The examination of the EEDF shape as a function of hydrogen incorporation yield two key observations. The first is as increasing the hydrogen content the overall number density decreases. This is plausible since hydrogen is electronegative and also provides an energy loss mechanism to the electrons via molecular dissociation (compared to the purely electropositive argon case). This provides a loss mechanism for electrons higher than the ionization threshold for argon, thereby reducing the rate of ionization.

The second observation is that as the hydrogen content increase the high energy tail tends to increase. This observation appears to support the reduction in electron density due to hydrogen electronegativity as opposed to dissociative energy losses in the electron population that would result in a reduction in electron tail temperature.

Figures 5.8 a-b. Comparison EEDFs for different argon/hydrogen mixtures.

Figure 5.8 a. 50mtorr/140W.

Figure 5.8 b. 40mtorr/120W.

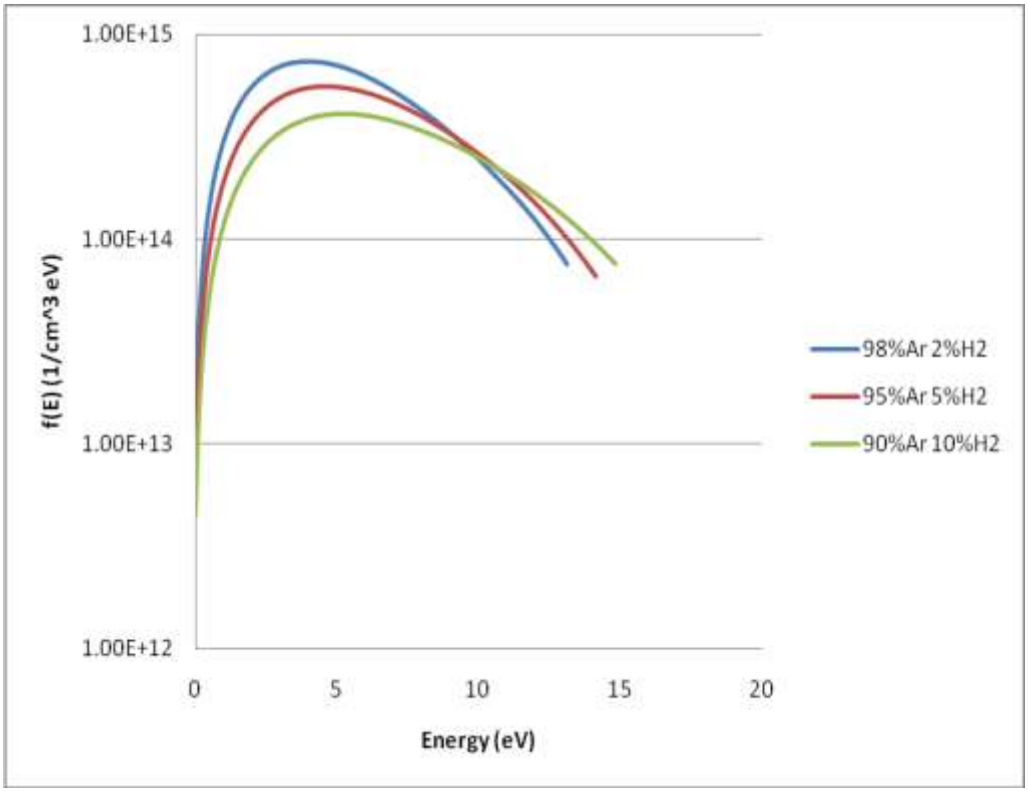
1.00E+15
1.00E+14
1.00E+13
1.00E+12
f(E) (1/cm^3 eV)
0
5
10
15
20
Energy (eV)
98%Ar 2%H2
95%Ar 5%H2
90%Ar 10%H2

(a)

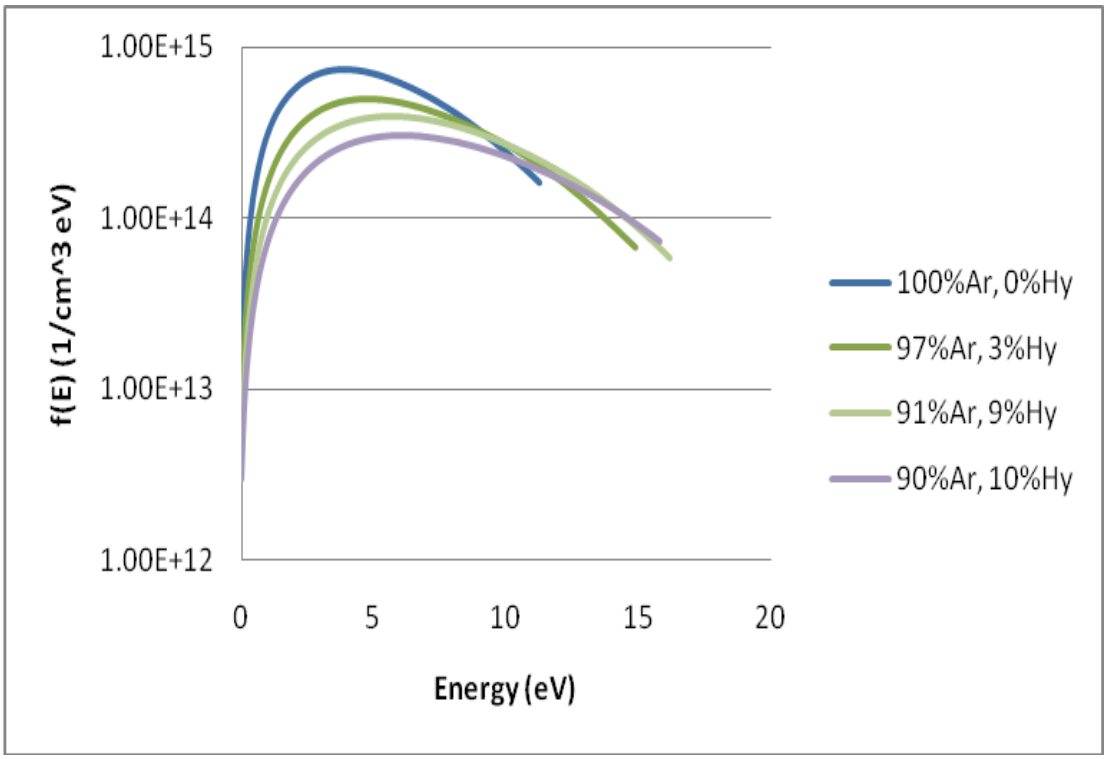
1.00E+15
1.00E+14
1.00E+13
1.00E+12
f(E) (1/cm^3 eV)
0
5
10
15
20
Energy (eV)
100%Ar, 0%Hy
97%Ar, 3%Hy
91%Ar, 9%Hy
90%Ar, 10%Hy

(b)

5.6. References

[1] Neyts E., Yan M., Bogaerts A., Gijbes R., "PIC-MC Simulation of an RF Capacitively Coupled Ar/H2 Discharge", *Nuc. Inst. and Methods in Phys. Res. B*, 202, 2003, pp. 300-304.

[2] Olthoff J. K., Greenberg K. E., "The Gaseous Electronics Conference RF Reference Cell-An Introduction", *J. Res. Natl. Inst. Stan. Technol.*, 100(4) No. 9A. 1995, pp. 327-339.

[3] Brake M. L., Pender J., Fournier J., "The Gaseous Electronics Conference (GEC) Reference Cell as a Benchmark for Understanding Microelectronics Processing Plasmas", *Phys. Plas.*, 6(5), 1999, pp. 2307-2313.

[4] Miller P. A, Hebner G. A., Greenberg K. E., Pochan P.D., Aragon B.P., "An Inductively Coupled Plasma Source for the Gaseous Electronics Conference Reference Cell", *J. Res. Natl. Inst. Stand. Technol.*, 100, 1995, pp. 427-439.

[5] Hopwood J., "Review of Inductively Coupled Plasmas for Plasma Processing", *Plasma Source Sci. and Technol.*, 1(2), 1992, pp.109-116.

CHAPTER 6

Conclusions and Recommendations for Future Research

In conclusion, this thesis was able to improve regularization methods for the extraction of EEDFs. There have been two methods widely applied; Druyvesteyn's method and Tikhonov's regularization method. Regarding Tikhonov's regularization, we were able to show that, due to its challenges of optimizing the regularization parameter and the high error at the low energy end of the reconstructed distribution (which mainly caused it rarely to be used) our advanced algorithm which is the Hybrid method overcomes such challenges making reconstructed EEDFs more accurate and can be carried out over a wide energy range than Tikhonov's method.

As for Druyvesteyn's method, it neglected the shape of the probe whether it was cylindrical or spherical. Such negligence results in errors in reconstructed distributions to be around 5% and even higher in cases of nonmaxwellian distributions. In this thesis we dealt with the geometry of the probe and the effect on the current collected from the plasma and thus the EEDF. Langmuir's paper, first stated a different equation for the case of cylindrical probe and another for the spherical probe. Combining that with the new hybrid method we were able to prove that geometry has a substantial effect on EEDFs and the mere assumption that cylindrical and spherical probes can be treated the same is absolutely not correct.

In the end the technique specified in this thesis is capable of measuring subtle changes in EEDF as a function of plasma condition over a wide energy range with higher accuracy than any other technique. This was all possible under the fact that integral methods were used to boost the accuracy of EEDF analysis.

The following are recommendations for future research:

- The construction of a spherical probe and comparing the I-V curve for both spherical and cylindrical probes to verify our theory.
- Taking the mathematical model a step further by trying to quantify the error in the EEDF and thus being able to add error bars to be able to point out where the error is minimal and where it maximizes and under what conditions.
- To verify our algorithm in extreme plasmas such as pulsed plasma and as well as flowing plasmas.